Cape Peninsula
University of Technology

Sub-10 MeV proton irradiation effects on a coating obtained from the pulsed laser ablation of W_2B_5/B_4C for space applications

by

Sokeng Ifriky TADADJEU

Thesis submitted in partial fulfilment of the requirements for the degree

Doctor of Technology: Electrical, Electronic and Computer Engineering

in the Faculty of Engineering

at the Cape Peninsula University of Technology

Supervisor: **Prof. Malik Maaza**
Co-supervisor: **Prof. Robert R van Zyl**

Bellville
January 2015

DECLARATION

I, Ifriky Tadadjeu Sokeng, declare that the contents of this thesis represent my own unaided work, and that the thesis has not previously been submitted for academic examination towards any qualification. Furthermore, it represents my own opinions and not necessarily those of the Cape Peninsula University of Technology.

The research outputs from this work include:

- Tadadjeu Sokeng, I., Ngom, B. D., Cummings, F., Kotsedi, L., Msimanga, M., Maaza, M. & Van Zyl, R. R. 2015. Proton-induced nanorod melting in a coating obtained from the pulsed laser ablation of W_2B_5/B_4C. *Nuclear Instruments and Methods in Physics Research B*, 344: 70-75, February.
- Tadadjeu Sokeng, I., Ngom, B.D., Coetzee-Hugo, L., Msimanga, M., Nuru, Z. Y., Maaza, M., Van Zyl, R. R. 2014. Pulsed laser ablation of W_2B_5/B_4C ceramic composite for space applications. *4th Design, Development and Research Conference*, 8-10 September. ISBN: 978-0-620-62981-0
- Tadadjeu Sokeng, I., Ngom, B.D., Coetzee-Hugo, L., Msimanga, M., Nuru, Z. Y., Kotsedi, L., Maaza, M., Van Zyl, R. R. 2015. Coatings synthesized by the pulsed laser ablation of W_2B_5/B_4C ceramic composite. *Thin Solid Films,* Available online [21 September 2015]: http://www.sciencedirect.com/science/article/pii/S0040609015009086

Signed **Date**

ABSTRACT

This research investigates the effects of sub-10 MeV protons on coatings obtained from the pulsed laser ablation of W_2B_5/B_4C. This is in an attempt to extend the bullet proof applications of W_2B_5/B_4C to space radiation shielding applications, offering low cost and low mass protection against radiation including X-rays, neutrons, gamma rays and protons in low Earth orbit. The focus in this research, however, is on low energy protons.

The associated problems addressed in this work are solar cell degradation and Single Event Upsets in high density semiconductor devices caused by low energy protons. The relevant constraints considered are the necessity for low cost, low mass and high efficiency solutions. The work starts with a literature review of the space environment, the interaction of radiation with matter, and on pulsed laser deposition as a technique of choice for the coating synthesis. This paves the way for the pulsed laser ablation of W_2B_5/B_4C. The resulting coating is a solid solution of the form $WC_{1-x}B_x$ which contains crystalline and amorphous forms. Two proton irradiation experiments are carried out on this coating, and the resulting effects are analysed. The effects of 900 keV proton irradiation were the melting and subsequent growing of nanorods on the surface of the coating, the lateral transfer of the proton energy across the coating surface, and the lateral displacement of matter along the coating surface. These effects show that the coating is a promising cost effective and low mass radiation shield against low energy protons. The effects of 1 MeV protons on this coating are the three-stage melting of rods formed on the coating surface, and further evidence of lateral transfer of energy across the coating surface. Optical measurements of this coating show that it is about 73% transparent in the Ultraviolet, Visible and near Infrared range. This allows it to be used as radiation shielding for solar cells, in addition to high density semiconductor devices, against low energy protons in low Earth orbit. Simulations show that based on coulombic interactions alone, the same level of protection coverglass offers to solar cells can be achieved with about half the thickness of $WC_{1-x}B_x$ or less.

Additional contributions of this research include the report of a naturally occurring reversed Stranski-Krastanov film growth mode for this coating, and the proposition of a rod structure made up of a material enclosure containing nanospheres.

This work contributes to fields across various disciplines, including Electrical Engineering, Structural Engineering, Satellite Systems Engineering, Radiation Physics, Experimental Physics, and Material Science.

Based on this research, it is recommended that pulsed laser deposition be considered more as an application technique rather than simply a laboratory technique. It is also recommended that the coating synthesised be considered for testing on active space

missions. Two missions under development that have already shown interest are ZACUBE-2 (3U CubeSat) from CPUT/F'SATI in South Africa, and AOBA-VELOX (2U CubeSat) from the Kyushu Institute of Technology in Japan.

ACKNOWLEDGEMENTS

I wish to thank:

- God almighty. Yours is the glory. Thank you!
- The French South African Institute of Technology / Cape Peninsula University of Technology and iThemba LABS-National Research Foundation. For providing the necessary sponsorship and experimental facilities for this research.
- My supervisors Prof. Malik Maaza and Prof. Robert R van Zyl. For your guidance, advise, coaching, motivation and support. You were and you are true scientific parents and mentors to me. Thank you for teaching me much more than how to contribute to knowledge.
- Dr. Balla Diop Ngom. It is safe to say that without you I would not have made it this far in this short amount of time. You held my hand when everyone else was too busy, and this even while you were out of the country. Thank you for carrying me step by step through the details of my laboratory work, experimentation, analysis and writing.
- Dr. Zebib Yenus Nuru. Thank you for showing me the way to true scientific independence.
- Prof. Carlos Pineda, Dr. Mlunghisi Nkosi, Dr. Lebogang Kotsedi, Dr. Christopher Mtshali, Dr. Philip Sechogela, Dr. Remy Bucher, Ms. Langutani Mathevula, and the iThemba LABS Van De Graaf accelerator technical staff. Your patience in teaching me everything I needed to know with regards to the use of equipment, software, and administrative procedures has shaped me into the scientist I am today. Thank you for making me feel at home at iThemba LABS Material research department.
- Ian van Zyl and Cindy Engel. Your support has been a major contributor to the completion of my thesis, and to my activities at F'SATI both in-house and as part of collaborations. Thank you!!
- Tony Lumbwe, Enrico Louw, Morne Roman, Vernon Davids, Angela Shumba, and Flavien Minko. During my darkest hours I could always rely on you. I owe you more than words can say and will be eternally grateful to you. Your friendship remains a blessing beyond measure to me.
- All the students from F'SATI and iThemba LABS MRD. You breathe life into the science and engineering we do. It was great to share my laughter, tears, victories, defeats, fun, frustrations, work and everything else with you every day for the duration of my thesis. Thank you for being my brothers and sisters. I trust we will remain a family.
- My friends, parents and siblings (especially my mother). Thank you for believing in me and never giving up on me.

DEDICATION

To my father, late Professor **Maurice Tadadjeu**,

Dad, I guess this one finally has my name on it! I'm proud to be a part of what you liked to call 'your universe'.

To my mother, **Sokeng Catherine**,

Mom, I am proud to point at you and say 'That's my mommy… Thank her for the man I have become!!'.

TABLE OF CONTENTS

LIST OF FIGURES

LIST OF TABLES

GLOSSARY

Term	Meaning
Pulsed Laser Deposition (PLD)	A physical vapour deposition technique which involves the ablation of a material target with a laser beam to produce a plasma plume which expands to grow a film onto a substrate.
Bragg peak	The maximum point on a Bragg curve, which is the plot of the energy loss of an ionising particle as it travels through matter.
CubeSat	A low cost, containerised nano-satellite with a mass between 1 and 4 kg for smaller form factors of 1, 2 and 3 units.
X-ray Diffraction (XRD)	A materials characterisation technique involving the scattering of X-rays by the atoms of a material under study, producing a diffraction pattern that gives information on the crystal structure and/or the identity of the material.
Scanning Electron Microscopy (SEM)	An imaging technique whereby the sample to be imaged is scanned with a focussed beam of electrons, causing it to emit secondary electrons which in turn form a pattern used to generate a 3D image of the sample.
Energy-Dispersive X-ray Spectroscopy (EDS)	An analytical characterisation technique used to determine the elemental and/or chemical characteristics of a sample.
X-ray Photoelectron Spectroscopy (XPS)	A surface sensitive quantitative technique used to determine the empirical formula, chemical and electronic states of the constituent elements of a sample.

Chapter 1 Introduction

Since the definition of CubeSat design specifications (California Polytechnic State University, *s.a*), many CubeSat missions have been successfully developed and launched. They provide a fast and cost effective solution to human capacity development in the space industry and to the usage of space for research and technology development. Commercial-off-the-shelf (COTS) components, which are not designed for use in space and therefore are not radiation hardened, are used extensively to reduce the cost of development (Clyde space, 2012). Exposure to the space environment (protons, electrons, gamma radiation, solar energetic particles) causes Single Event Effects (SEEs) which affect the performance of satellites, more so those employing COTS components (Barnard and Nwosa, 2011). In current CubeSat design, there are more efforts to accommodate the effects of high energy particle radiation than attempting to mitigate these effects or to prevent them. This is because strategies to provide effective radiation shielding usually increase the satellite mass, software and hardware, and financial budget. Barnard and Steyn (2007) published a cost-effective way of performing Total Ionising Dose (TID) tests for COTS components. Their work, in addition to the design of radiation shielding for nano-satellites in Low Earth Orbit (Mayanbari and Kasesaz, 2011), shows that it is possible to have both acceptable radiation shielding and low cost satellite component testing. There is, however, a problem when it comes to the relationship between the evolution of technology used in space and the testing standards being applied.

SEE testing has been synonymous with high energy testing because in the past (before Integrated Circuits with technology nodes less than 130 nm commonly used), SEEs were mainly caused by high energy heavy ions, and protons exceeding 50 MeV. This is because high energy protons, through Linear Energy Transfer (LET), ionise the bulk material they travel through along their paths and generate secondary heavy ions through collisions, spallation and nuclear reactions (Cannon *et al*., 2010). These heavy ions in turn have enough energy to cause damage in the sensitive areas of electronic components, resulting in Single Event Upsets (SEUs). These effects affect semiconductor devices, including devices based on Complementary Metal-Oxide-Semiconductor (CMOS) technology. One of the most sensitive implementations of this technology most affected by SEUs is memory, particularly Static Random Access Memory (SRAM) (Maurer *et al., 2008*).

Figure 1.1 shows the time evolution of CMOS-based SRAM technology nodes (Gaillard, 2011), while Figure 1.2 reports the variation of the Single Event Rate (SER) of SEUs and Multiple Bit

Upsets (MBU) with technology nodes, and the influence of direct ionisation by low energy protons (Hubert *et al.*, 2009). From Figure 1.1, commercial semiconductor devices considered and/or used in space post-2006, are sub-130 nm CMOS-based devices. Figure 1.2 shows that for sub-130 nm technology, the effect of direct ionisation by low energy protons becomes significant. The simulation results shown in Figure 1.2 are consistent with experimental data reported by Heidel *et al.* (2008) on a 65 nm device and by Lawrence *et al.* (2009) on a 90 nm device, where the SEU cross-sections for protons of energies less than 1 MeV are orders of magnitude larger than those of protons of energies greater than 100 MeV. From Figure 1.1 and Figure 1.2, one can notice that in addition to heavy ions and high energy protons, low energy protons are becoming a major concern.

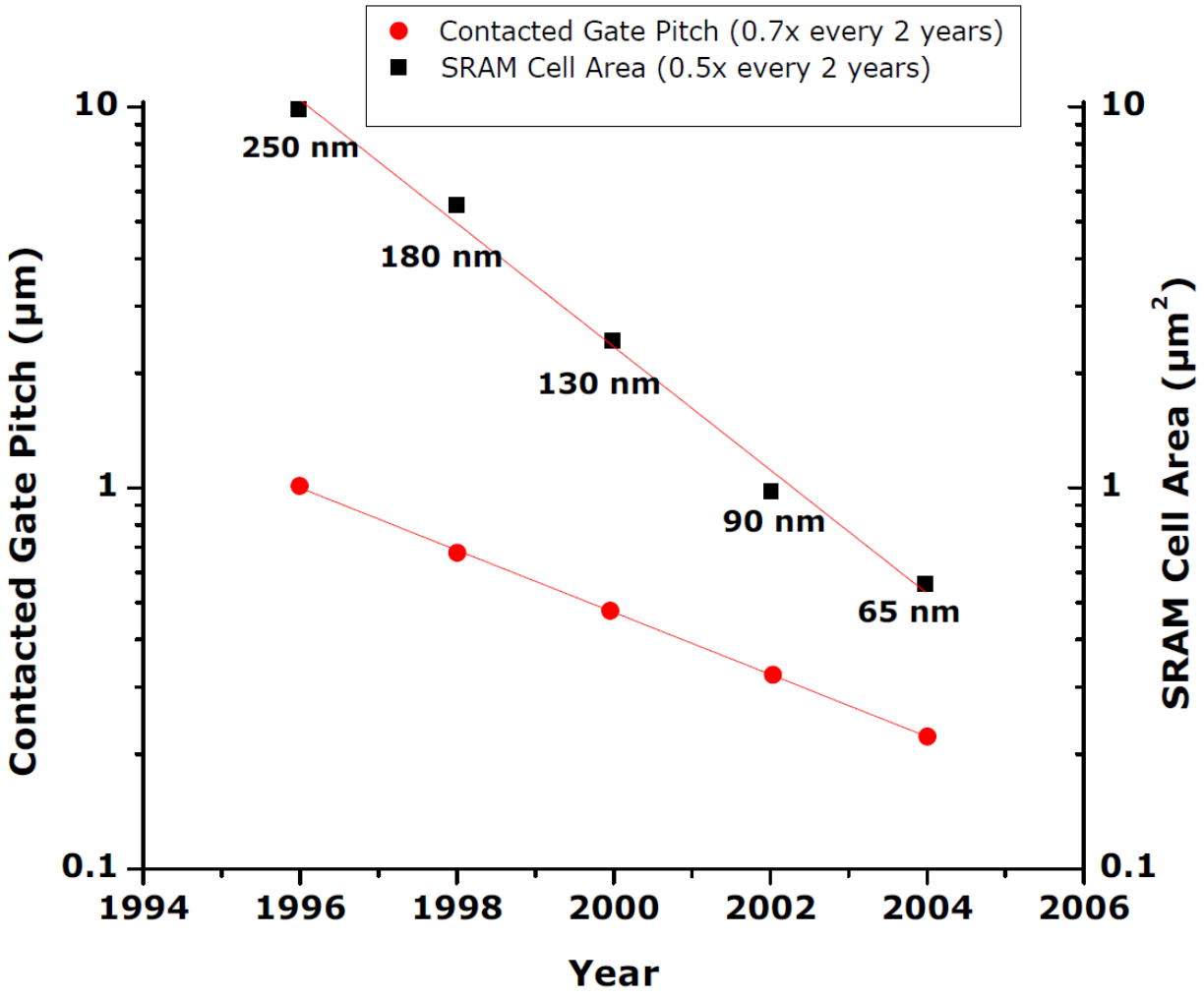

Figure 1.1: **SRAM cell area and contact gate pitch variation with technology nodes and their respective dates of development.**

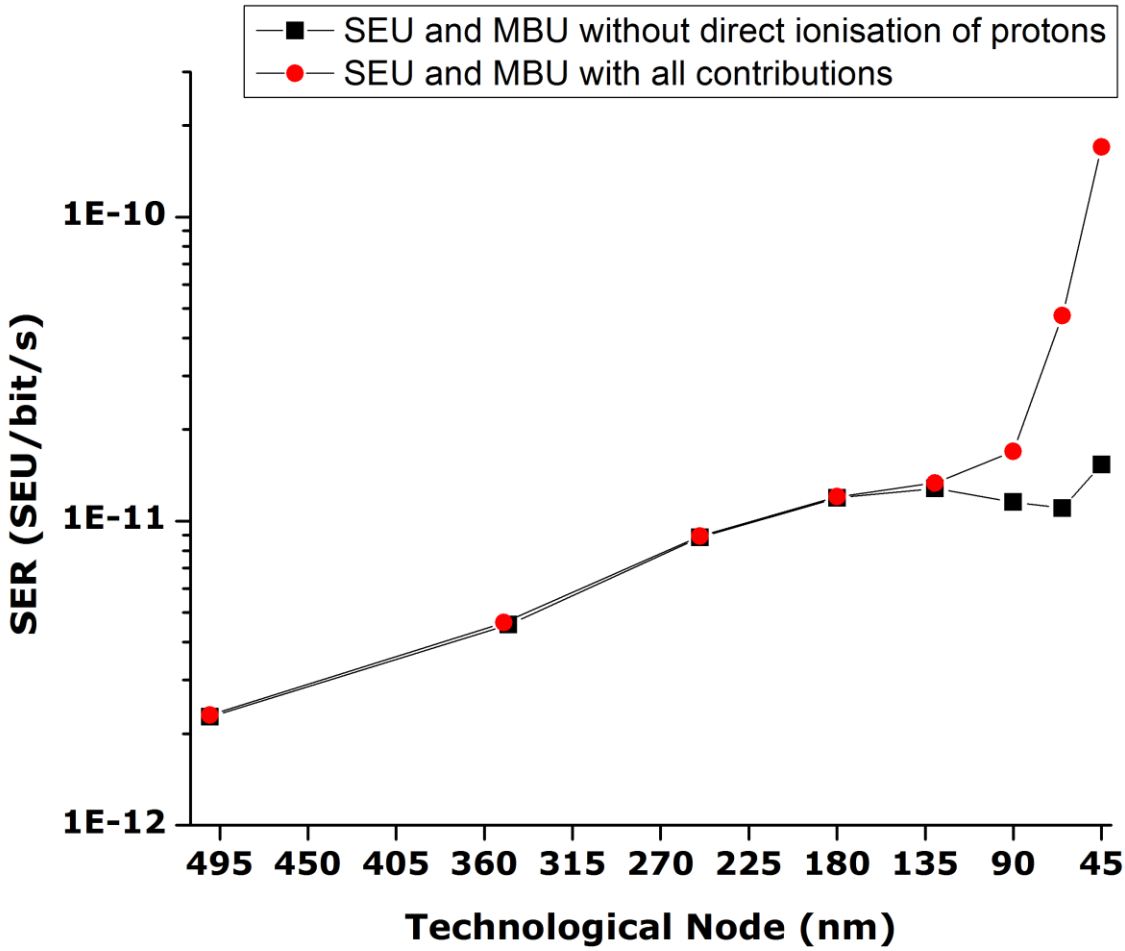

Figure 1.2: **Simulated variation of SER with technology nodes showing the contribution of direct ionisation by low energy protons.**

1.1 Background on transistors and SEUs

Julius Lilienfeld's patent (1933) led to the development of the first field effect transistor. Further developments in the following two decades brought about the successful implementation of a bipolar junction transistor with a feature size of 100 µm (Bardeen and Brattain, 1948; Shockley, 1951). In the early 1960s, Willmark and Marcus (1962) in their paper on trends in microelectronics predicted the minimum feature size to be about 10 µm (which turned out to be wrong) and that direct ionisation by cosmic rays would cause errors in circuits with small enough feature size (which was correct and very much ahead of its time). Two years later, Jack Kilby was awarded two patents, one of which was for the invention of the Integrated Circuit (IC) (Kilby, 1964; Kilby, 1964). The following year, Gordon Moore made a prediction on the density

of ICs, projecting the number of transistors per chip to double every second year for the following 10 years (Moore's law) (Moore, 1965). Two years after that, CMOS logic was invented (Wanlass, 1967). In the 1970s, the effects predicted by Willmark and Marcus were observed and studied. These effects were called *anomalies* in 1975, *bit errors* in 1978, *soft errors* and *single event upsets* in 1979 (Binder *et al*., 1975; Pickel and Blandford, 1978; May and Woods, 1979; Guenzer *et al*., 1979). The term *soft error* refers to errors that are not permanent and can be corrected (as opposed to hard errors which are permanent errors due to permanent damage).

In space, the main causes of SEUs are protons and heavier ions (Barak, 2006). High energy protons cause nuclear reactions as they traverse bulk material. The products of these nuclear reactions are heavier ions which travel in the material and cause SEUs when they reach a sensitive region of a digital semiconductor device (such as an SRAM). The following expressions 1 to 5 show the different types of proton-induced nuclear reactions likely to occur with Oxygen (Ulmer and Matsinos, 2010). These are of concern, especially for CMOS technology.

1. $p + O_8^{16} \Rightarrow n(neutron) + F_9^{16}(\beta^+ - decay, T_{1/2} = 22\,\mathrm{sec} + \gamma)$
2. $p + O_8^{16} \Rightarrow p + n + O_8^{15}(+\beta^+ - decay, T_{1/2} = 124\,\mathrm{sec} + \gamma)$
3. $p + O_8^{16} \Rightarrow p + p + N_7^{15}(+\beta^+ - decay, T_{1/2} = 10\,\mathrm{min} + \gamma)$
4. $p + O_8^{16} \Rightarrow \alpha + N_7^{13}(+\beta^+ - decay, T_{1/2} = 124\,\mathrm{sec} + \gamma)$
5. $p + O_8^{16} \Rightarrow d(deuterons) + O_8^{15}(+\beta^+ - decay, T_{1/2} = 124\,\mathrm{sec} + \gamma)$

Reaction 1 is most probable for proton energies < 50 MeV. This probability decreases rapidly at energies between 50 MeV and 60 MeV, and vanishes above 60 MeV. Reaction 2 produces a neutron and the incident proton is not absorbed. This requires at least 50 MeV to occur. Reaction 3 requires at least 60 MeV to occur, and its probability increases with energy. Reaction 4 produces an α - particle from clusters in the nucleus. This requires about 100 MeV and its probability increases up to about 190 MeV, after which it decreases rapidly. In reaction 5, higher energy protons destroy clusters in the nucleus and release deuterons (the nucleus of deuterium also known as heavy hydrogen). It is energetically possible above 60 MeV but is only significant above 200 MeV. From the energies at which these reactions occur, it will be evident from the

space environment description in Chapter 2 that in Low Earth Orbit (LEO), reactions of type 1 are of biggest concern.

Low energy protons lose energy as they penetrate deeper into the material, and they eventually stop as they reach their Bragg peak. Equation 1.1 defines the Linear Energy Transfer LET through distances x in a material. Equation 1.2, which is known as the Bethe formula, is the classical expression of the specific energy lost by a particle with energy E, velocity v and charge z_e, through atoms of number density N, atomic number Z, electron rest mass m_0 and electronic charge e (Glenn, 2000:31),

$$LET = -dE / dx \qquad \text{Equation 1.1}$$

$$-dE / dx = \frac{4\pi z_e^4 e^4}{m_0 v^2} NB \qquad \text{Equation 1.2}$$

where $$B = Z\left[\ln\frac{2m_0v^2}{I} - \ln\left(1-\frac{v^2}{c^2}\right) - \frac{v^2}{c^2}\right].$$

I is the average excitation and ionisation of each element and c is the speed of light. For non-relativistic charged particles, $v << c$, and only the first term of B is significant.

The LET is measured in charge per unit length, and if this charge at the Bragg peak is greater than or equal to the minimum charge necessary to cause an upset (critical charge), then this proton can cause an SEU. It should be noted, however, that for a low energy proton to cause an SEU, its Bragg peak charge should be at least equal to the critical charge, and this Bragg peak should occur in a sensitive region (Hubert *et al*., 2009). Heidel *et al*. have shown the dependence of the upset cross-section on the incident angle of low energy protons (2008), as the incidence angle affects the probability that the Bragg Peak will occur in a sensitive region.

Figure 1.3 illustrates the conditions necessary for low energy proton SEUs by direct ionisation. Figure 1.4 illustrates some of the events that occur during most ground tests at normal incidence. In Figure 1.4 (a) and (c) the Bragg peak occurs before and after the sensitive region respectively, whereas in Figure 1.4 (b), it occurs in the sensitive region. In space, however, the angles of incidence are not always normal and occur from different sides in a stochastic

manner. Figure 1.5 shows experimentally obtained effects of incidence angle on SEU cross-section[1] (Heidel *et al.*, 2008).

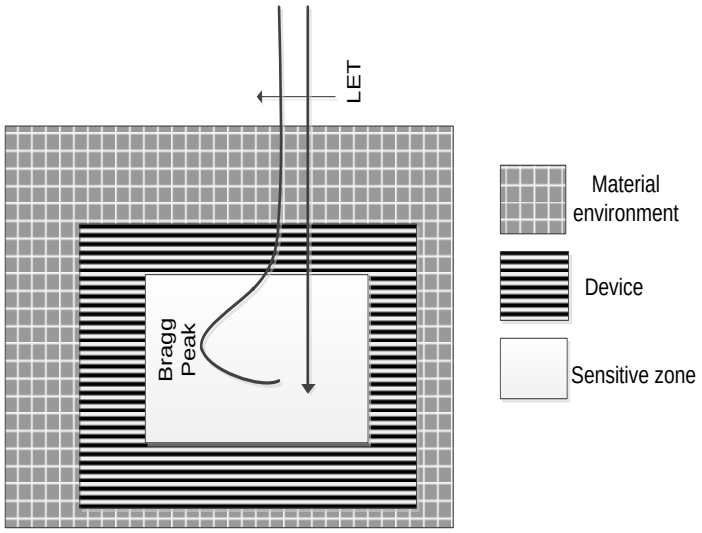

Figure 1.3: Illustration of the conditions to induce SEUs.

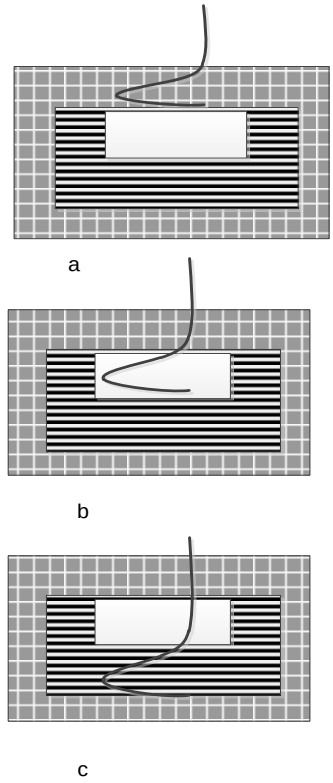

Figure 1.4: Bragg peak (a) before the active region (b) in the active region (c) after the active region.

[1] Ratio of number of upsets to particle fluence

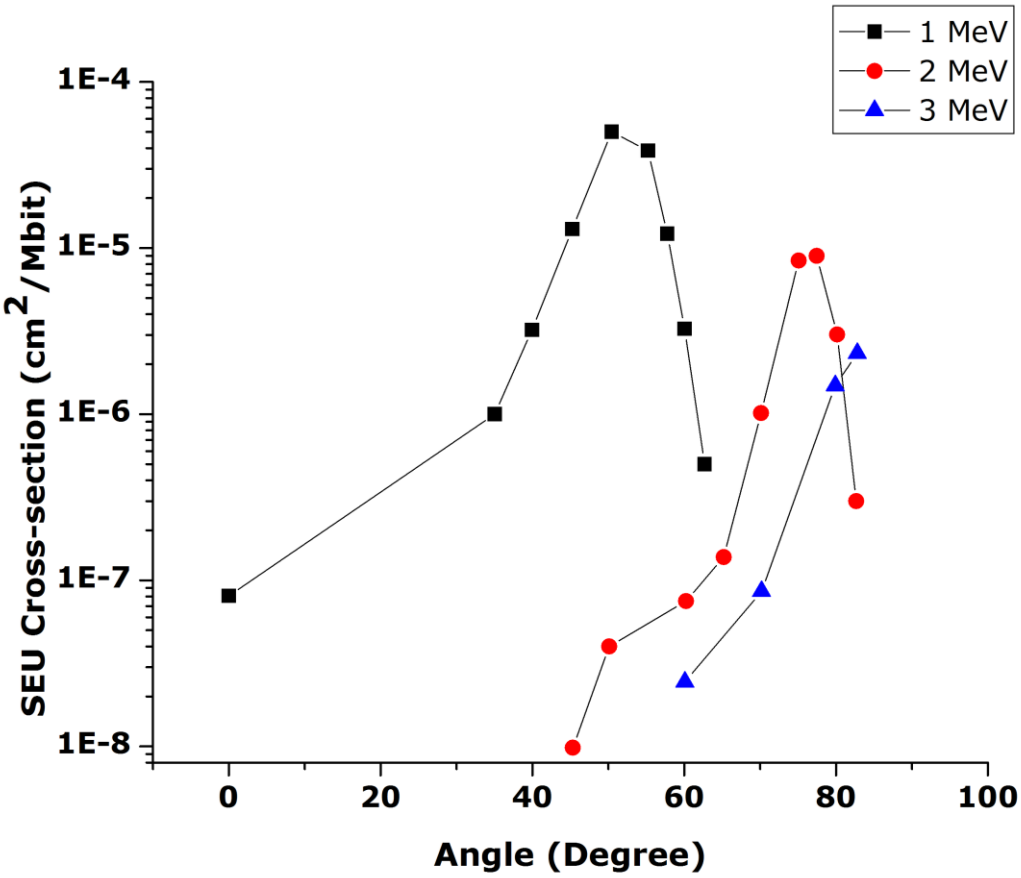

Figure 1.5: Low energy proton SEU cross-section variation with incident angle.

Currently, ways to mitigate SEUs include shielding (with Aluminium for instance), Radiation Hardening By Design (RHBD) where components are designed with extra circuitry to make them more SEE immune, Error Detection and Correction (EDAC) where codes like the Hamming code are used to correct single and double-bit errors, and Triple Modular Redundancy (TMR) where a voting technique is used to choose data between redundant systems (Mauer *et al*., 2008). Shielding of 2 mm Al has been shown to be a viable option for CubeSats (Mayanbari and Kasesaz, 2011), although depending on specific missions, there is generally little provision for extra mass, code and/or circuitry.

1.2 Background on solar cell degradation due to low energy protons

The first practical Silicon solar cell was announced by the Bell Laboratories in 1954 (Chapin *et al.*, 1954). In 1957, G.L. Pearson, D.M. Chapin and C.S. Fuller received the US2780765 patent for their "*Solar Energy Converting Apparatus*". The following year, T. Mandelkorn from U.S Signal Corps Laboratories, fabricated a more radiation-resistant n-on-p Silicon photovoltaic cell[2]. Hoffman electronics achieved 9% efficiency with these cells and that same year, the Vanguard 1 was the first solar powered satellite in space, having on board a < 1 W

[2] The history of solar: https://www1.eere.energy.gov/solar/pdfs/solar_timeline.pdf

array to power its radios[1]. By the end of 1958 (until today), solar cells had become the accepted energy source for space applications. They were, however, only commercialised the following year when Hoffman electronics introduced 10% efficient photovoltaic cells to the market (they were also the first to use grid contacts to reduce series resistance).

As will be described in Chapter 2, protons of energies less than 10 MeV are the most probable in LEO. Solar panels are in direct contact with the space environment and, therefore, are most likely to encounter low energy protons. The degradation of Silicon solar cells due to protons is still mainly caused by protons of energies less than 5 MeV[3]. Cost, efficiency and functionality per unit mass are main drivers in space technology. This has driven the shift from Silicon solar cells to GaAs/Ge and InGaP/GaAs/Ge cells (among others), which have proven to be lighter and/or more efficient. Unfortunately, Bekhti's comparative study (Bekhti, 2013) shows that protons of energies between 0.5 MeV and 3 MeV still induce the most loss in maximum power output.

The solar panel degradation can be linked to the number of vacancies produced by protons in the active volume (Messenger *et. al.*, 2005). In the case of multiple-junction cells, such as InGaP/GaAs/Ge, protons affect the electrical properties of each junction differently. Quantum efficiency measurements show that in this particular example, degradation in the overall cell is largely due to degradation in the GaAs junction (Messenger *et. al.*, 2005).

There are two main methods for predicting the End of Life (EOL) photovoltaic parameters (maximum power, short circuit current and open circuit voltage) for a solar array considered for use in space. The first was developed by the US Jet Propulsion Laboratory (JPL) in the 1980s (Tada *et. al.*, 1982; Anspaugh *et. al.*, 1984; Anspaugh, 1989; Anspaugh, 1996). It is widely used and incorporated in many space radiation suites including SPENVIS[2] and OMERE[4] among others. This method aims at determining the normal incidence 1 MeV electron fluence which produces the same level of damage to the cell as a specific radiation environment. It is generally known as the JPL Equivalent Fluence method.

The second was developed by the US Naval Research Laboratory (NRL) (Summers *et. al.*, 1994; Summers *et. al.*, 1995; Summers *et. al.*, 1997; Messenger *et. al.*, 1997; Messenger *et. al.*, 1999; Morton *et. al.*, 1999). The aim of this method is to determine the displacement damage dose for a given mission by using the Non-Ionising Energy Loss (NIEL) for protons and electrons traversing a bare solar cell. It is generally known as the NRL method.

[3] https://www.spenvis.oma.be/help/background/soldam/soldam.html#effpro
[4] http://www.trad.fr/OMERE-Software.html

The NRL method is much less complex and much less expensive than the JPL method as it requires much less experimentation (Messenger *et. al.*, 2001). Furthermore, this method can be used in conjunction with Monte Carlo based software, such as SRIM (Ziegler *et al.*, 2010) to estimate the relative damage coefficients for solar cells in various radiation environments (Messenger *et. al.*, 2005).

Figure 1.6 presents the prediction of degradation in the maximum power of a GaAs/Ge solar panel after one year in orbit as a function of coverglass thickness (Messenger *et. al.*, 2001). The simulated orbit is dominated by sub-10 MeV protons, which are the main contributors to solar cell degradation in space.

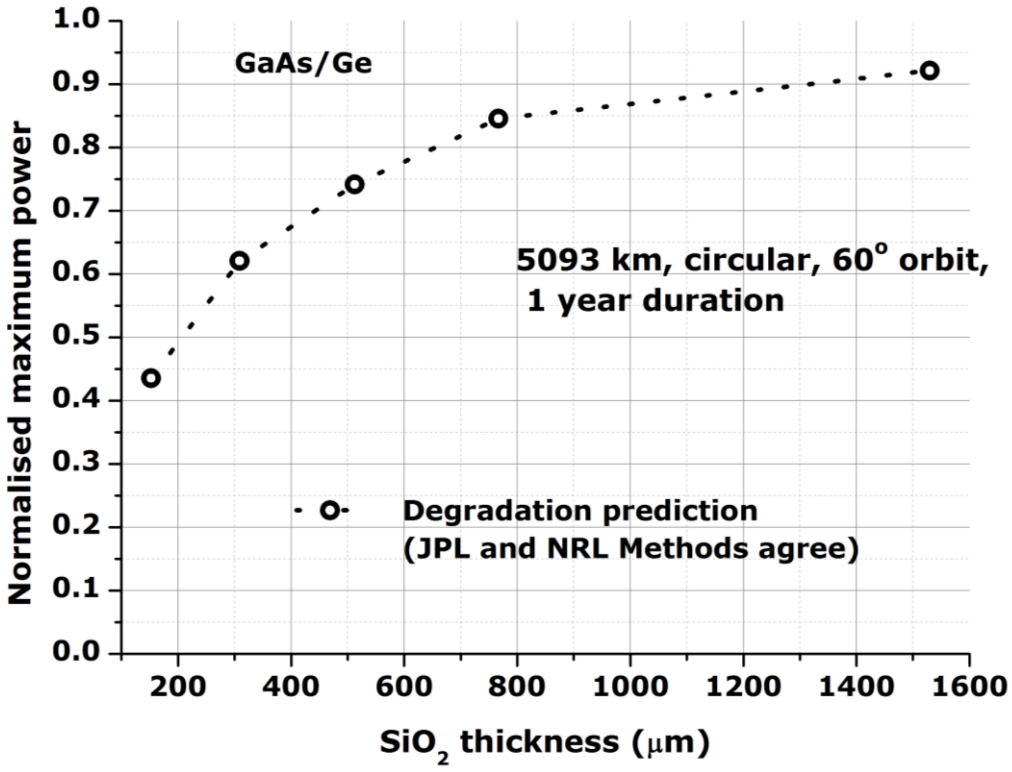

Figure 1.6: Degradation prediction of maximum power output for a GaAs/Ge solar cell in a proton dominated orbit.

1.3 Background on a B_4C/W_2B_5 ceramic composite target

Boron Carbide based ceramics are used for bulletproof vest applications for their high hardness (about 30 GPa), high melting point (2427 ^oC) and low density (2520 $g.mm^{-3}$) (Wang, 2008; Yin *et. al.*, 2013). They are also used as neutron radiation absorbents for their high neutron absorption cross-section (about 600 barn) (Yin *et. al.*, 2013). Monolithic B_4C, however, has a low strength (<300MPa) and low fracture toughness (about 2.2 $MPa.m^{1/2}$) (Wen *et.al.*, 2000).

The thermal and electric properties of B_4C can be enhanced by doping it with a second phase with different thermoelectric properties, such as W_2B_5, as was done by Cai and Nan (2000). Figure 1.7 and Figure 1.8 show the temperature dependence of the electrical conductivity and the thermal conductivity, respectively, of B_4C with and without W_2B_5, where the B_4C/W_2B_5 composite was prepared by sintering of WC-based cement balls milled in B_4C powder (Cai and Nan, 2000). These figures show how much the addition of W_2B_5 increases the electrical and thermal conductivities of the composite.

The addition of W_2B_5 was also reported to increase the flexure strength and the fracture toughness of the resulting Boron Carbide based composite ceramic (Wen *et al*., 2000; Yin *et al.*, 2013). Table 1.1 and Table 1.2 show the mechanical properties of the B-W-C composites, prepared by Wen *et.al.* and Yin *et.al*., respectively (also prepared by sintering of B_4C and WC). These tables show how much the addition of W_2B_5 ameliorates the mechanical properties of B_4C mentioned earlier.

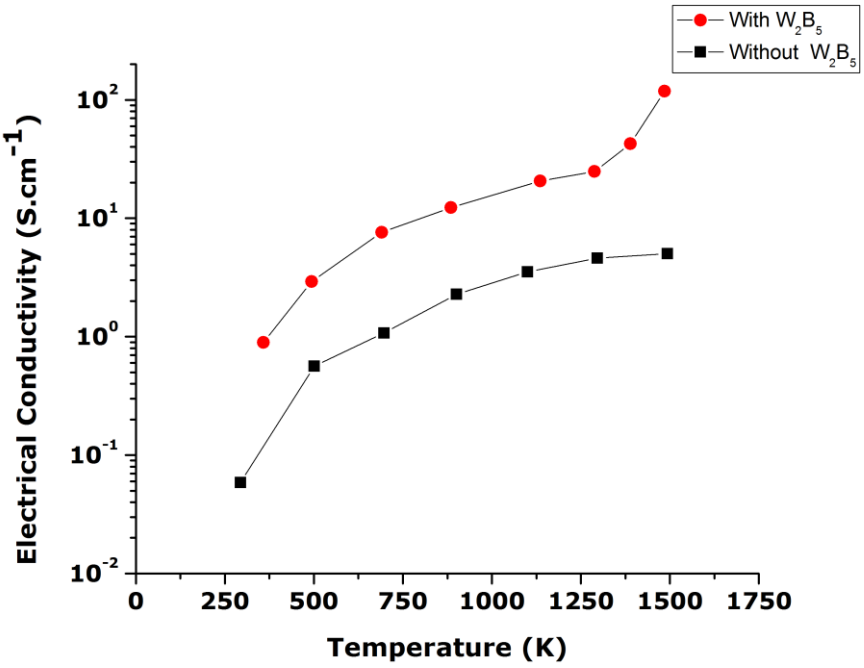

Figure 1.7: Temperature dependence of electrical conductivity of B_4C with and without W_2B_5

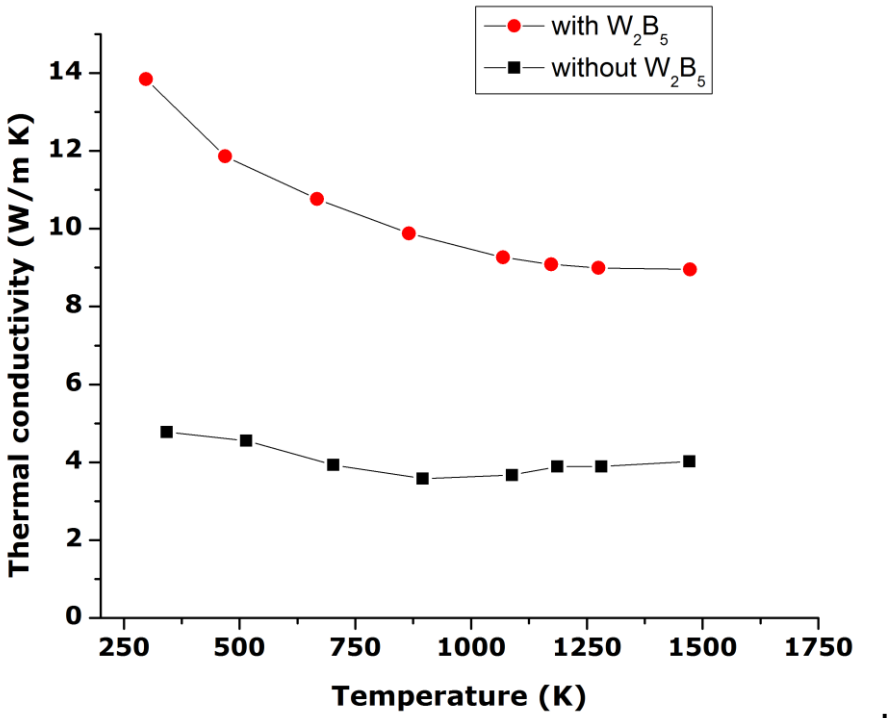

Figure 1.8: **Temperature dependence of thermal conductivity of B_4C with and without W_2B_5.**

Table 1.1: **Composition of materials, sintering parameters and properties of resulting ceramic composite.**

Material	Composition (Vol%)		Sintering Condition			Porosity (%)	Flexure Strength (MPa)	Fracture Toughness ($MPa.m^{1/2}$)
	WC	B_4C	Temp (^oC)	Press (MPa)	Time (min)			
B_4C-20WC	20	80	1800	35	30	9	298.9 ± 22.6	5.12 ± 0.61
			1900	35	30	4	345.6 ± 37.2	6.98 ± 0.26
B_4C-40WC	40	60	1800	35	30	5	400.1 ± 11.3	8.11 ± 0.74
			1900	35	30	2	453.6 ± 26.7	8.70 ± 0.41

Table 1.2: **Mechanical properties of B(W)C ceramic composites sintered at 2150 ^oC for 2 hours.**

	Flexural Strength (MPa)	Elastic Modulus (GPa)	Vickers Hardness (GPa)	Fracture Toughness ($MPa.m^{1/2}$)
B-6C	150 ± 19	215 ± 14	29.2 ± 0.4	-
BW-1.5C	260 ± 5	293 ± 10	28.1 ± 0.7	3.78 ± 0.14
BW-6C	354 ± 16	348 ± 10	25.2 ± 0.4	5.80 ± 0.12

For the purposes of this research, a pellet of B_4C/W_2B_5 was acquired. Its mechanical properties, the presence of W which is characterised by a large atomic number (and hence large X-ray absorption), and its large neutron absorption cross-section (due to its Boron content), are all of interest. If it can stop bullets, then it likely has lateral energy diffusion properties. W, being heavy, is likely to stop X-rays. If coatings of this material can be synthesised, then they are likely to provide a level of radiation hardening for space applications in LEO.

Figure 1.9 (Tadadjeu Sokeng *et al.*, 2015a) shows the X-ray Diffraction (XRD) spectrum of the pellet. The B_4C and W_2B_5 phases are consistent with those in the composites prepared in literature (Cai and Nan, 2000; Wen *et.al.*, 2000; Radev *et.al.*, 2002; Yin *et.al.*, 2013). The B_4C peaks were identified using the Powder Diffraction File (PDF-file) JCPDS 00-035-0798 and the W_2B_5 peaks were identified using the PDF-file JCPDS 00-038-1365. Micro-Particle Induced X-ray Emission (Micro-PIXE) analyses revealed some impurities including Fe, Ca, Co, Si, K and Ti in very little amounts.

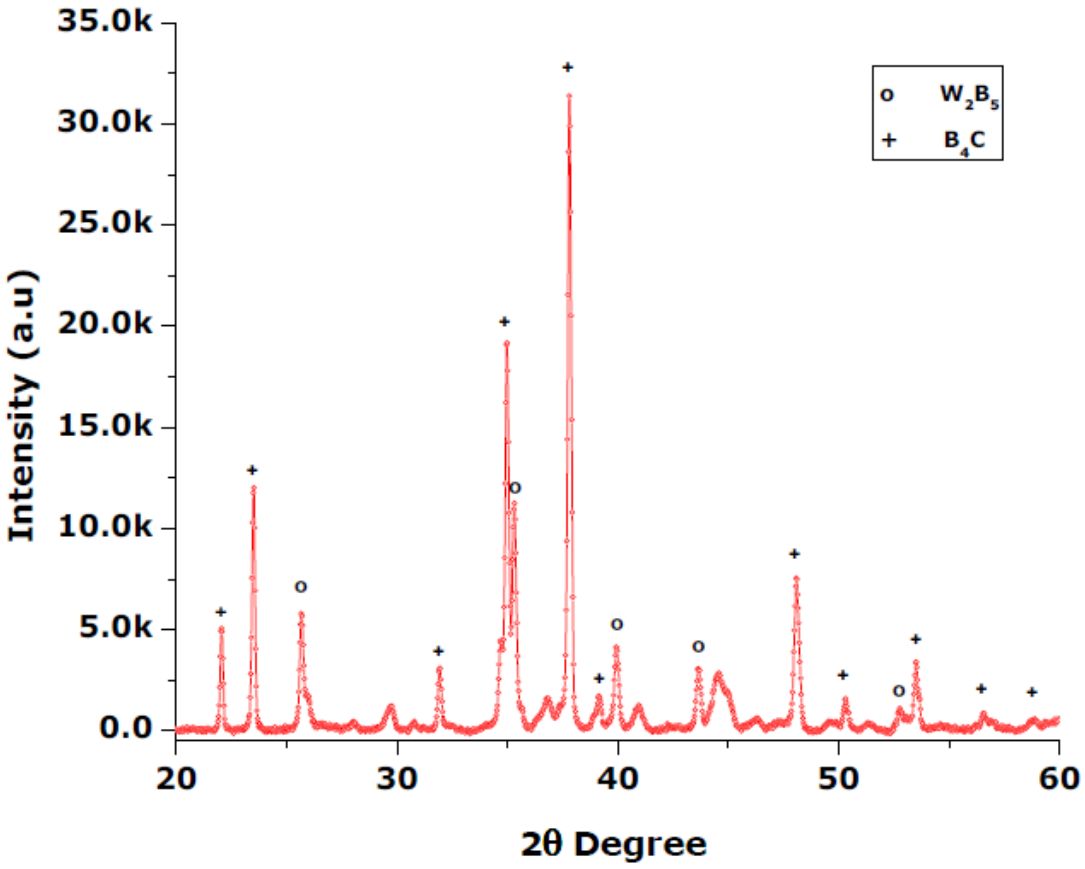

Figure 1.9: Measured XRD spectrum of the B_4C/W_2B_5 pellet.

This composite can absorb neutrons and X-rays simply because it contains Boron and W, respectively. Figure 1.10 shows how the cross-section for true absorption of neutrons and X-rays for elements with atomic numbers ranging from 1 to 92 (Bacon, 1965). Evident is the high neutron absorption cross-section of Boron, and the high X-ray absorption cross-section of W. Although elements such as Li^6 and Gd have higher neutron absorption cross-sections than Boron, Boron still offers a very good neutron absorption cross-section for its cost and weight. Despite its weight, W is relatively affordable and offers a very good X-ray absorption cross-section.

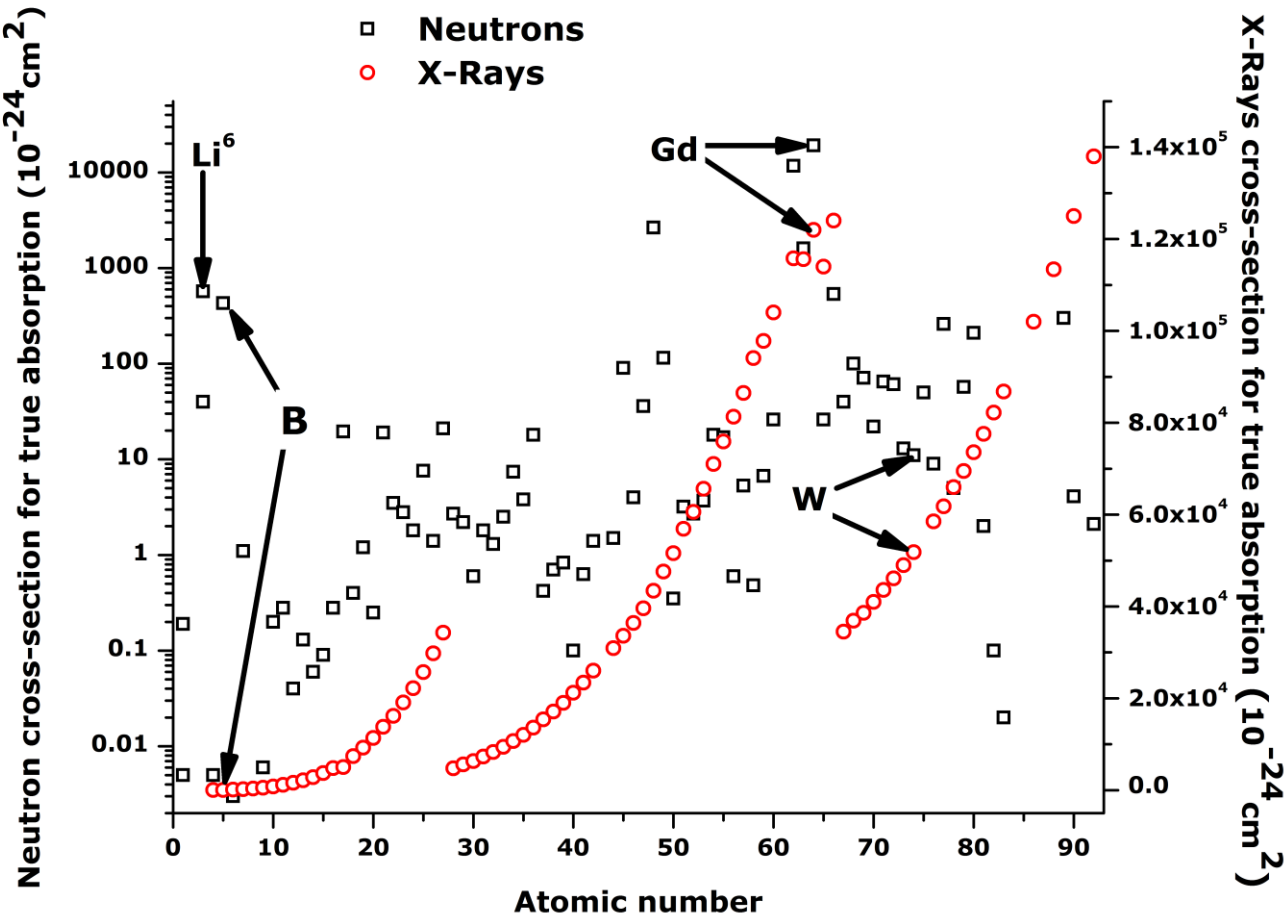

Figure 1.10: **Cross-section for true absorption of neutrons and X-rays as a function of atomic number.**

1.4 Research problem and relevance

Low energy protons have always been a major contributor to solar cell degradation in space, despite the advances in solar cell technology. They are now becoming a main source of SEUs in high density semiconductor electronics. There is, therefore, a need to investigate the effects of low energy protons on materials for space applications. A switch from bullet-proof applications to possible space radiation shielding applications of B_4C/W_2B_5 is of particular interest in this work (in addition to neutron and X-ray absorption due to B and W, respectively). This investigation contribute to achieving better shielding and mitigation, especially in small satellites where cost, efficiency and mass are critical design constraints.

This project is part of the French South African Institute of Technology (F'SATI) space program. It is the first project in this program that focuses on space radiation effects as part of nano-satellite related design and research. It expands the knowledge base within the program, which is already relatively extensive in the field of CubeSat space mission and spacecraft design.

Within the collaboration between F'SATI and the NRF iThemba Laboratory for Accelerator Based Sciences (iThemba LABS), this pioneering project between the groups developes the knowledge and expertise network in the field of nano-satellite radiation studies and testing, both at a fundamental level and at an engineering level. In fact, within this framework, this project significantly contributes to closing the gap between fundamental sciences and engineering in the field of radiation effects on space applicable materials and devices.

Specific outcomes of this research should contribute to the philosophy of small satellite design in terms of the mitigation of space radiation, and contribute to the knowledge base on space radiation effects on space-applicable materials and devices. The outcomes also contribute to the knowledge base on the synthesis and applications of B_4C/W_2B_5 as coatings by PLD.

1.5 Research questions

- How can coatings be synthesised from a B_4C/W_2B_5 pellet?
- How can such coatings offer any level of protection against various types of radiation, specifically low energy protons?
- What are the physical mechanisms providing protection against radiation of this coating?
- How can these coatings be effectively used for space applications?
- What improvement in longevity do these coatings provide for critical components of a spacecraft, such as solar panels?

1.6 Research objective

The main objective of this research is to investigate the space applicability of B_4C/W_2B_5 as a shield against low energy protons. Of specific interest is whether the bullet proof characterisitcs of B_4C/W_2B_5 can be exploited for applications in space. This can be broken down into three sub-goals:

- Synthesise and characterise coatings obtained from B_4C/W_2B_5;
- Subject the synthesised coatings to low energy proton irradiation;
- Determine whether the coating can be applied as a shield for protection against low energy protons.

1.7 Research methodology

- An extensive literature review is done on the space radiation environment, with a focus on low energy radiation and the interactions of the space environment with materials relevant to satellite design.
- Coatings are synthesised from B_4C/W_2B_5 and characterised.
- These coatings are irradiated with low energy protons to investigate the resulting radiation effects.
- The space applicability of the coatings is determined based on the analysis of the low energy proton irradiation experiments.
- The in-orbit shielding capability of the coating is simulated for solar cell applications.
- The results of the research are published in appropriate journal articles, and explained in a full doctorate thesis.

1.8 Delineation

- Pulsed Laser Deposition (PLD) is used for the coating deposition because with this method a wide range of materials including oxides, nitrides, polymers and even metals can be prepared at temperatures as low as room temperature (Ngom, 2010).
- Only the B_4C/W_2B_5 pellet acquired for this research is investigated for coating.
- All the hardware, software, testing and experimentation related to this project are restricted to the capabilities and facilities of CPUT and iThemba LABS.
- For the purposes of the targeted applications, any energy between 0.8 MeV and 1.5 MeV is, on average, equally relevant. The proton energy for each experiment will be

restricted to the most stable energy available within this range on the day of the irradiation.

1.9 Synopsis

The problem addressed in this research, the methodology used to address this problem, as well as the relevance and significance of the research is given in this chapter. In Chapter 2, the space radiation environment is described. Chapter 3 focuses on PLD as a physical vapour deposition technique. In Chapter 4, the experiments carried out in this research are described. This chapter also reports on the results and analysis. Chapter 5 outlines the conclusions and recommendations for future work.

Chapter 2 Space radiation environment

2.1 Introduction

Space is a hostile environment for both humans and electronics because of the high level of radiation of different types and the presence of both man-made debris and natural micro-meteoroids (Pippin, 2003). This chapter describes the different types of radiation species that constitute the space radiation environment. The sources of these radiation species and some of their properties are discussed, as well as how they interact with matter.

2.2 General overview

This section gives an overview of the space environment, specifically in the low Earth orbits (LEOs).

2.2.1 Low Earth orbit

Although Maini and Agrawal (2011) define LEOs as those orbits at altitudes between 150 km and 500 km above the surface of the earth, orbits of altitudes up to 1000 km are generally considered as LEO (Pippin, 2003; Haduverdi and Baylakoglu, 2011). The Advanced Land Observing Satellite (ALOS) has collected data on the LEO space radiation environment for solar-activity minima between September 2006 and February 2011 (Koshiishi and Matsumoto, 2012). Energies of around 10 MeV for protons and around 1 MeV for electrons were chosen to characterize the space radiation environment because they are the most prevelant among the particles capable of penetrating spacecraft walls.

Table 2.1 shows the simulated probability distribution per energy range of protons at 650 km altitude (Mayanbari and Kasesaz, 2011). This is a good estimate of the population of different energetic protons in LEO. It shows that sub-10 MeV protons are much more probable to find in LEO than protons of higher energies. Figure 2.1 shows the proton flux as a function of the energy spectra in LEO (Mayanbari and Kasesaz, 2011). It compares simulation results to the data plotted with the CRÈME[5] software, which uses models based on a database containing data from the 1970s to 2007 (Mayanbari and Kasesaz, 2011). It shows that there is a much higher flux of low energy protons in LEO.

[5] https://creme.isde.vanderbilt.edu/CREME-MC

Table 2.1: Simulated probability of protons based on their energy spectra at 650 km altitude.

Energy spectrum (MeV)	Probability
1-10	0.882994
10-20	0.012832
20-30	0.008637
30-40	0.009249
40-50	0.008353
50-150	0.051168
150-250	0.01698
250-350	0.006103
350-400	0.003684

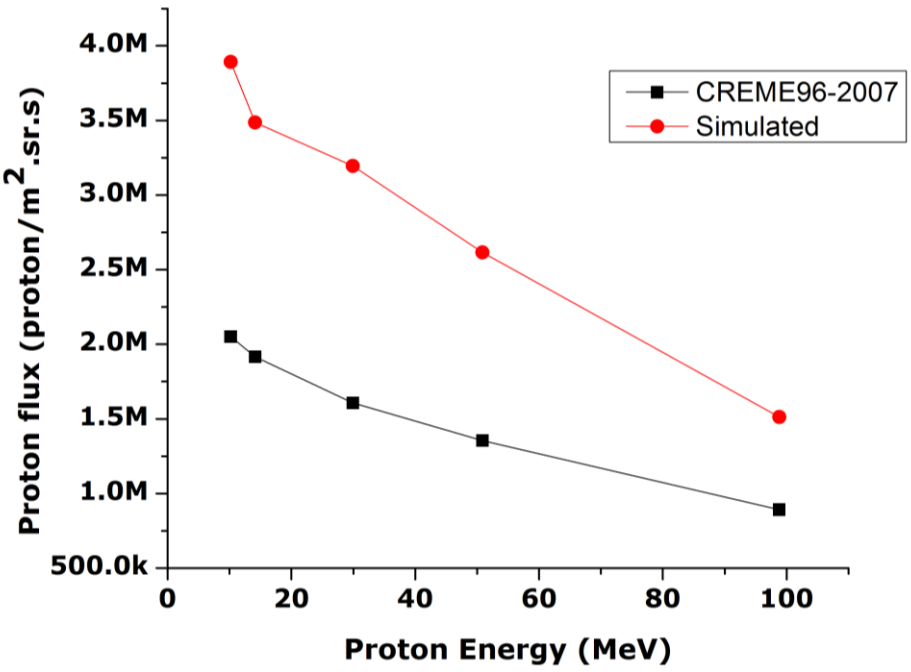

Figure 2.1: Variation of proton flux with energy in LEO

Reitz characterised the space radiation environment both in low Earth orbit and in deep space (Reitz, 2008). He describes the main sources of space radiation which are Galactic Cosmic Radiation (GCR), Solar Cosmic Radiation (SCR) and trapped radiation, as well as

their interactions with materials and magnetic fields. He also describes their doses and flux for LEO and interplanetary missions.

2.2.2 Galactic Cosmic Radiation

While there is no conclusive experimental proof of their origins outside the solar system, GCR is known to be made up of particles of all charges from protons to Uranium nuclei, with about 83.3% protons, 13.72% alpha particles, 2% electrons and 0.98% heavier nuclei. The energy of particles can vary from a few MeV/nucleon to about 10^{15} MeV/nucleon (Reitz, 2008; Badhwar, 1997). Their fluence rate is inversely proportional to the intensity of solar activity, and varies by a factor of about 3 or 4 (Reitz *et al*., 2005). The GCR flux is omni-directional and its fluence rate increases from low to high latitude orbits, with only the very high energy relativistic particles (about 1 GeV per atomic mass unit) being able to penetrate the Earth's magnetic field to low altitudes (Reitz *et al*., 2005; Cucinotta *et al*., 2003).

2.2.3 Solar Cosmic Radiation

SCR consists of solar winds and Solar Particle Events (SPEs). Solar winds are continuously emitted particle radiation from the sun, mainly consisting of protons and electrons. These particles have an intensity that varies between about 10^{10} and 10^{12} particles/cm/s/sr. Their velocities vary between about 300 km/s and 800 km/s. Their energies are very low, roughly between 100 eV and 3.5 keV for protons (Reitz, 2008). SPEs are large local outbursts of coronal radiation from the surface of the sun. These consist mainly of gamma rays, hard and soft X-rays, and radio waves in a wide frequency band. They can have energies up to several GeV (Reitz, 2008).

2.2.4 Trapped radiation

The interaction of GCR and SCR with the Earth's magnetic field results in belts of trapped particles, called the *van Allen belts* (Reitz, 2008). They consist of electrons (up to 7 MeV), protons (up to 600 MeV) and heavier ions (less than 50 MeV/nucleon) and extend over a region from about 200 km to about 75 000 km in altitude around the geomagnetic equator. The inner belt is mainly formed by decaying neutrons from cosmic particle interactions producing protons and electrons. The outer belt is mostly populated by electrons and consists mainly of trapped solar particles (Reitz, 2008).

At altitudes between 200 km and 600 km above the surface of the Earth, the energy of charged particles is such that the main absorbed dose inside spacecraft is due to protons, especially at the South Atlantic Magnetic Anomaly (SAMA), which is an area over the coast of Brazil where the radiation belts come closest to the Earth's surface at and altitude of about

200 km (Reitz *et al*., 2005). The SAMA occurs because the geomagnetic axis of the Earth is 11^0 inclined from the Earth's axis of rotation towards Northern America, and its dipole centre is displaced by 500 km towards the Western Pacific. This results in a significantly reduced magnetic field above the coast of Brazil (Reitz, 2008). The contribution of individual GCR elements in terms of fluence, dose and equivalent dose can be found in literature (Cucinotta *et al*., 2003).

2.3 Radiation species and their interaction with matter

This section details how the different radiation types in space interact with matter. These radiation types include protons, heavy charged particles, electrons, neutrons and electromagnetic radiation.

2.3.1 Protons and heavy charged particles

Protons are positively charged Hydrogen ions and heavy charged particles are particles which have a mass very large compared to the mass of an electron (Green and Hamman, 1971). They lose energy as they traverse matter primarily by Coulomb force interactions with atomic electrons, leaving the atoms along their path ionised or in an excited state. They also lose energy during possible elastic collisions with atoms, which can result in atomic displacement.

Protons with energies in the tens of MeV can knock out sub-atomic particles from a target nucleus during inelastic collisions with nuclei. This phenomenon is more likely to occur at higher energies (Strauch, 1962). In this interaction, incident protons produce a multiplication of particles by knocking out several particles by direct interaction with individual nucleons in target nuclei. This is called the *cascade effect* and the resulting particles are called *cascade particles*, having a forward direction relative to that of the incident protons (Green and Hamman, 1971).

After the passage of incident protons and the emission of cascade particles, the target nucleus loses its excitation energy by isotropically emitting neutrons, protons and lighter nuclei. The latter emissions and the cascade particles have a much higher potential for damage as they are greater in number and slower than the incident protons. The average number of neutrons and protons emitted due to these two processes, per incident proton, per inelastic collision, is a function of the incident proton energy and the atomic mass of the target nucleus (Wallace and Sandhaus, 1962).

The nuclear inelastic scattering cross-section σ is given by Equation 2.1 (Green and Hamman, 1971),

$$\sigma = \pi(1.3\times10^{-13}A^{1/3})^2 cm^2, \quad \text{Equation 2.1}$$

where A is the atomic number of the target nucleus. The mean inelastic scattering free path λ_{in} of a particle is given in Equation 2.2 (Green and Hamman, 1971),

$$\lambda_{in} = \left(\frac{\sigma N_0}{A}\right)^{-1} g/cm^2, \quad \text{Equation 2.2}$$

where N_0 is Avogadro's number. The average fraction F_{in} of incident protons that will undergo this type of interaction is given in Equation 2.3 (Green and Hamman, 1971),

$$F_{in} = 1 - e^{-x/\lambda_{in}} \quad \text{Equation 2.3}$$

2.3.2 Electrons

Electrons' primary mechanism of energy loss is the ionisation of the atoms in the material they traverse. In addition, high energy electrons lose energy through the Bremsstrahlung generation of X-rays. The ratio of the energy lost per unit path length from Bremsstrahlung generation to that lost from ionisation is given in Equation 2.4 (Green and Hamman, 1971),

$$\frac{\left(\frac{dE}{dx}\right)_{Bremsstrahlung}}{\left(\frac{dE}{dx}\right)_{Ionisatioin}} = \frac{EZ}{800}, \quad \text{Equation 2.4}$$

where E is the energy of the electron in MeV, and Z is the atomic number of the absorbing material (the material interacting with the electron). The Bremsstrahlung radiation created by a high energy electron is much more penetrating than the electron itself and is an additional source of radiation damage.

2.3.3 Neutrons

Neutrons can be produced from the fission of U^{253} and Pu^{239}. Neutrons produced this way are called fission neutrons. They have energies from 0.75 to 17 MeV and fit the distribution $N(E)$ shown in Equation 2.5 (Glasstone and Sesonske, 1963),

$$N(E) = 0.484\sinh(2E)^{1/2}e^{-E}, \quad \text{Equation 2.5}$$

where $N(E)$ is the number of neutrons of energy E per unit energy interval for each emitted neutron.

Neutrons can also be produced by the interaction of alpha particles with Beryllium, Boron and Lithium in reactions such as shown in Equation 2.6 (Green and Hamman, 1971),

$$Be_4^9 + \alpha \rightarrow C_6^{12} + n \ . \qquad \text{Equation 2.6}$$

Neutrons can also be produced by the interaction of Bremsstrahlung gamma rays when the latter have energies greater than the binding energy of the last neutron in the target nucleus. Neutrons produced this way are nearly mono-energetic and are called photo-neutrons. This type of reaction can occur due to Bremsstrahlung radiation generated when high energy electrons are slowed down in a high density target (Green and Hamman, 1971).

Neutrons can be grouped into thermal neutrons (kinetic energy approximately 0.025 eV), epithermal neutrons (kinetic energy approximately between 0.025 eV and 10 keV) and fast neutrons (kinetic energy greater than 10 keV). Of these three groups, only fast neutrons are likely to cause atomic displacement and indirect ionisation. Mechanisms of ionisation by fast neutrons are listed below (Green and Hamman, 1971):

- Elastic scattering in which recoil neutrons have enough energy to produce ionisation;
- Inelastic scattering in which gamma photons are emitted which can produce indirect ionisation;
- Nuclear reactions induced by neutrons in which ionising particles are emitted.

Boron and Lithium have high absorption cross-sections for thermal neutrons and can emit alpha particles as a result of thermal neutron absorption.

2.3.4 High energy electromagnetic radiation

Electromagnetic radiation can be viewed as discrete energetic photons travelling at the speed of light, which also have a wave-like nature expressed by the photon frequency given by $E = h\upsilon$ where E is the photon energy, h is Plank's constant and υ is the frequency associated with the photon (Green and Hamman, 1971). In the space environment, the electromagnetic radiations of interest are gamma rays, X-rays and ultraviolet light.

Gamma rays have the highest energy (greater than 0.1 MeV) and originate within atomic nuclei. X-rays have less energy than gamma rays. They originate either from interactions involving orbital electrons, blackbody radiation of heated mass or by Bremsstrahlung radiation resulting from inelastic scattering of charged particles by a nucleus. Ultraviolet light has less energy than X-rays, mainly originate from the sun, and is only weakly ionising.

When discussing the attenuation of electromagnetic radiation in matter, a useful term is the linear attenuation coefficient μ given in Equation 2.7 (Glenn, 2010),

$$\mu = \frac{(\rho N_0 \sigma_{atom})}{A} \quad , \qquad \text{Equation 2.7}$$

where ρ is the material density, N_0 is Avogadro's number, σ_{atom} is the photon cross-section per atom (expressed in terms of the photon cross-section per electron σ_e in an atom with atomic number Z as $\sigma_{atom} = Z\sigma_e$), and A is the atomic mass of the absorbing material. The intensity of a beam traversing a material of thickness x is given in Equation 2.8 (Green and Hamman, 1971; Glenn, 2010),

$$I = I_0 e^{-\mu x} , \qquad \text{Equation 2.8}$$

where I_0 is the initial beam intensity.

Introducing the mass attenuation coefficient μ/ρ, Equation 2.8 can be expressed as Equation 2.9 (Green and Hamman, 1971; Glenn, 2010),

$$I = I_0 e^{-\left(\frac{\mu}{\rho}\right)\rho x} \quad . \qquad \text{Equation 2.9}$$

Electromagnetic radiation primarily interacts with matter through the photoelectric effect, the Compton Effect and pair production (Evans, 1955).

For low energies (< 0.2 MeV), the predominant mechanism is the photoelectric effect. In this mechanism, a tightly bound orbital electron absorbs the entire energy of a photon and is ejected from its atom with an energy $E = E_0 - E_B$ where E_0 is the initial energy of the photon and E_B is the binding energy of the electron. This process imparts energy on the atom which it releases by emitting X-rays or Auger electrons. Equation 2.10 is an approximation of how the photoelectric absorption cross-section ς varies with Z and E_0 (Evans, 1955),

$$\varsigma = const. \frac{Z^4}{E_0^3} \quad . \qquad \text{Equation 2.10}$$

For energies between about 0.2 MeV and 2 MeV, the predominant mechanism is the Compton effect. In this mechanism, the photon loses part of its energy to an orbital electron. The energised electron and the lower energy photon are both scattered, with the photon travelling at an angle φ with respect to its previous direction. The energy of the scattered photon is given by Equation 2.11 (Green and Hamman, 1971),

$$E_1 = h\upsilon_1 = \frac{E_0}{1 + \frac{E_0}{(m_0 c^2)}(1 - \cos\varphi)} , \qquad \text{Equation 2.11}$$

where m_0 is the rest mass of an electron, c is the speed of light, and E_0 is the energy of the incident photon. The kinetic energy of the electron is given by $E_e = E_0 - E_1$. The maximum energy that can be transferred to the Compton electron is given by Equation 2.12 (Billington and Crawford, 1961),

$$E_{e(\max)} = \frac{2E_0^2}{m_0c^2 + 2E_0} \quad . \qquad \text{Equation 2.12}$$

For energies of a few MeV, the predominant mechanism is pair production. In this mechanism the photon is completely absorbed from an electron-positron pair. This can only take place in the field of a charged particle (usually a nucleus). Equation 2.13 describes the energetics of this reaction (Green and Hamman, 1971),

$$E_0 = (E_{e^-} + m_0c^2) + (E_{e^+} + m_0c^2) = E_{e^-} + E_{e^+} + 1.02MeV \,, \qquad \text{Equation 2.13}$$

where E_{e^-} and E_{e^+} are the kinetic energies of the electrons and positrons, and $m_0c^2 = 0.511MeV$ for an electron.

2.4 Basic mechanisms of space radiation damage

Space radiation can cause damage in materials through two basic mechanisms: ionisation and atomic displacement. These can be caused directly or indirectly by the different radiation types discussed in the previous section.

2.4.1 Ionisation

Ionisation can be defined as the removal of one or more orbital electron from a neutral atom or molecule. It can occur when charged particles lose energy as they traverse matter. This energy is lost by any of four main interactions (Green and Hamman, 1971):

- **Ionisation by inelastic collision with a nucleus**
  The incident particle is deflected by the nucleus and part of its energy either goes into emitting a Bremsstrahlung photon or into exciting the nucleus.
- **Ionisation by elastic collision with a nucleus**
  The incident particle is deflected and part of its kinetic energy is imparted to the struck molecule according to the law of conservation of momentum.
- **Ionisation by elastic collision with an atom**
  The incident particle is deflected elastically by the atom as a whole, imparting an amount of energy usually too low to remove an atomic electron.

- **Ionisation by inelastic collisions with atomic electrons**
  The incident particle imparts enough energy to one or more atomic electrons to either excite them or completely remove them.

The primary mechanism for ionisation is by inelastic collision with atomic electrons where particles (directly) and electromagnetic radiation (indirectly) damage matter. The minimum energy required to remove an electron from an atomic orbital to a position where it is free from the nucleus is called the Ionisation Potential. The average energy E_p required to remove an electron, however, is two to four times greater than the ionisation potential because of energy lost in non-ionising processes, such as excitation and the kinetic energy of the ejected electron. The ejected electron and the resulting positively charged atom constitute an ion pair. In semiconductors, when a charged particle loses its energy by moving an electron from the valence band to the conduction band, the vacancy left behind has many of the properties of a positively charged particle. In this case, the energy balance is as given by Equation 2.14 (Shockley, 1961),

$$E_p = E_g + rE_r + 2E_F \ , \qquad \text{Equation 2.14}$$

where E_g is the semiconductor energy band gap, r is the number of phonons generated per ionisation , E_r is the phonon energy and E_F is the residual electron or hole energy after an ion pair is formed.

2.4.2 Atomic displacement

Atomic displacement occurs when an atom is displaced from its usual position within a crystal lattice. The damage caused by atomic displacement mostly affects materials with highly ordered lattice structures and whose macroscopic properties are affected by the latter. A vacant lattice position and an interstitial atom within a lattice are the simplest forms of this type of damage (Frenkel defect). The following is a description of the process of atomic displacement damage as proposed by Green and Hamman (1971).

When an incident particle (an energetic particle or a high energy secondary particle) collides with a lattice atom, it imparts to it recoil energy E_2. This target atom is displaced from its lattice position and creates a vacancy. It loses its energy through ionisation and/or thermal excitation and sometimes it has enough energy to displace other atoms. After a certain time the recoil atoms reach thermal equilibrium in interstitial positions, except for the atoms that fill vacancies. The simple defects and clusters thus caused, tend to anneal and move through

the crystal via thermal energy. The recombination of some vacancy-interstitial pairs and the formation of stable defect complexes eventually annihilate mobile defects.

Heavy charged particles, electrons and neutrons each cause atomic displacement in different ways.

2.4.2.1 Atomic displacement by protons and/or heavy charged particles

Rutherford scattering is the primary mechanism through which charged particles cause atomic displacement damage. In this mechanism, the incident charged particle is deflected in the electrostatic field of another charged particle. The incident particle loses energy to the target particle and both move away from the interaction point in directions that are determined by the law of conservation of momentum. Since this is an elastic collision, the total kinetic energy is conserved. Consider the interaction between an incident energetic particle (a proton for instance) and a target particle (a lattice atom for instance), with the following variables:

v_0 = velocity of incident particle before interaction

E_0 = energy of incident particle before interaction

m_1 = mass of incident particle

m_2 = mass of target particle

Z_1 = charge number of incident particle

Z_2 = charge number of target particle

e = unit electron charge

E_1 and v_1 are the kinetic energy and velocity, respectively of the recoiling incident particle

E_2 and v_2 are the kinetic energy and velocity, respectively of the recoiling target particle

θ = recoil angle in the centre of mass coordinate system

β = ratio of particle velocity to velocity of light

α = $Z_2/137$ ($1/137$ is the fine structure constant)

The non-relativistic differential scattering cross-section $d\sigma$ for transferring energy between E_2 and $E_2 + dE_2$ to a particle is given by Equation 2.15 (Green and Hamman, 1971),

$$d\sigma = \frac{2\pi(Z_1 Z_2 e^2)^2}{m_2 v_0^2} \frac{dE_2}{E_2^2} \quad . \qquad \text{Equation 2.15}$$

For relativistic interactions, this becomes (Green and Hamman, 1971)

$$d\sigma = \frac{2\pi(Z_1 Z_2 e^2)^2}{(m_2 c^2)\beta^2}\left[1-\beta^2\frac{E_2}{E_{2m}}+\pi\alpha\beta\left\{\left(\frac{E_2}{E_{2m}}\right)^{1/2}\frac{E_2}{E_2^2}\right\}\right]\frac{dE_2}{E_2^2} \quad , \qquad \text{Equation 2.16}$$

where $E_{2m} = \frac{4m_1 m_2}{(m_1+m_2)^2}E_0$ is the maximum energy that can be transferred to a recoiling particle. Most recoiling atoms, however, will have energies much less than E_{2m} because the spectrum of recoil energies E_2 produced by mono-energetic incident particles, varies as $(1/E_2)^2$ (van Lint and Wikner, 1963).

According to Billington and Crawford (1961), for energies between 0.1 MeV and 50 MeV, this expression of E_{2m} holds for non-relativistic particles and is valid for neutrons, protons and other heavy particles.

The number of recoil atoms with energies greater than some energy E is given by Equation 2.17 (Bilinski *et al*., 1962),

$$\sigma(E_{2m} > E) = \int_E^{E_{2m}} d\sigma = \frac{P_2}{\beta_2}\left[\frac{1}{E}-\frac{1}{E_{2m}}-\frac{\beta^2+\pi\alpha\beta}{E_{2m}}\ln\frac{E_{2m}}{E}+\frac{\pi\alpha\beta}{(E_{2m})^{1/2}}\left(\frac{1}{(E)^{1/2}}-\frac{1}{(E_{2m})^{1/2}}\right)\right], \qquad \text{Equation 2.17}$$

where $P_2 = \frac{2\pi(Z_1 Z_2 e^2)^2}{m_2 c^2}$, and if $E_{2m} \gg E$, then $\sigma(E_2 > E) \cong \frac{P_2}{E\beta^2}$.

Since $E_0 = (1/2)m_1 v_0^2 = (1/2)m_1 c^2 \beta^2$, σ varies with $1/E_0$ (Green and Hamman, 1971).

2.4.2.2 Atomic displacement by electrons

Since electrons have a very small mass, they need to travel at relativistic velocities to cause atomic displacement. In the vicinity of the displacement threshold, the cross-sections for electrons rise steeply with increasing energy and then level off and become nearly constant.

For $E_0 \ll m_0 c^2$, the maximum energy that can be transferred to a target particle of mass $m_2 \gg m_1$ by an electron of mass m_1 is given by Equation 2.18 (Green and Hamman, 1971),

$$E_{2m} = \frac{2(E_0 + 2m_1 c^2)}{m_2 c^2}E_0 \quad . \qquad \text{Equation 2.18}$$

An approximation of the mean energy transferred to the displaced particle is given by (Aukerman, 1962).

$$\overline{E_2} \cong \frac{E_d E_{2m}}{E_{2m} - E_d} \ln \frac{E_{2m}}{E_d} \qquad \text{Equation 2.19}$$

where E_d is the minimum amount of energy that can be imparted to an atom and still displace it (displacement threshold).

The displacement cross-section for relativistic electrons is given by (Seitz and Koehler, 1952),

$$\sigma_d = \frac{\pi}{4}(b')^2 \left[\left(\frac{E_{2m}}{E_d} - 1 \right) - \beta^2 \ln \frac{E_{2m}}{E_d} + \pi\alpha\beta \left\{ 2 \left[\left(\frac{E_{2m}}{E_d} \right)^{1/2} - 1 \right] \ln \frac{E_{2m}}{E_d} \right\} \right], \qquad \text{Equation 2.20}$$

where $\frac{\pi}{4}(b')^2 = \pi Z_2^2 \left(\frac{e^2}{m_1 c^2} \right)^2 \frac{1}{\beta^4(1-\beta^2)} = \frac{(2.495)10^{-25}(cm^2)}{\beta^4(1-\beta^2)} Z_2^2$, and as the cross-section becomes constant (as $E_{2m} \to E_d$) it approaches the value $\sigma_d \cong \frac{\pi}{4}(b')^2 \frac{E_{2m}}{E_d}$.

In practice, the net result of electron radiation is a pattern of isolated single displacements since the energy transferred is only slightly higher than the threshold energy and the recoiling atoms usually have insufficient energy to cause secondary displacements (Chadderton, 1965).

2.4.2.3 Atomic displacement by neutrons

Neutrons with energies less than about 1 MeV (for low Z materials) interact with atoms primarily by elastic scattering in which the incident neutron has a kinetic energy which is approximately equal to the total kinetic energy of the recoiling atom and neutron. Neutrons of low energy have elastic scattering cross-sections that range from 2 to 10 barns (1 barn = 10^{24} cm^{-2}) for most elements, with the notable exception of hydrogen for which it is 20 barns in its chemically bound state (Glasstone and Sesonske, 1963).

Consider an interaction between a neutron and a lattice atom, with the following variables:

m_1 = mass of the neutron in atomic mass units (a.m.u) = 1

m_2 = mass of the atom in a.m.u = atomic mass

E_0 = initial energy of the neutron

E_1 = recoil energy of the neutron

$E_{1\min}$ = minimum energy of recoil neutron

E_2 = kinetic energy imparted to target atom

Assuming isotropic scattering, the maximum fractional energy the neutron can transfer to the target atom given by Equation 2.21 (Green and Hamman, 1971),

$$\frac{E_{2\max}}{E_0} = 1 - \frac{E_{1\min}}{E_0} = 1 - \left(\frac{m_2 - m_1}{m_2 + m_1}\right)^2 \cong 1 - \left(\frac{m_2 - 1}{m_2 + 1}\right)^2 = 1 - r^2 \quad . \qquad \text{Equation 2.21}$$

If isotropy is not assumed, this equation should be multiplied by an anisotropy correction factor of between 1/2 and 2/3 for fission spectrum neutrons. At higher energies the anisotropy becomes greater (Green and Hamman, 1971).

Equation 2.22 gives the average decrease in the neutron's energy (Glasstone and Sesonske, 1963),

$$\xi = 1 - \frac{(m_2 - 1)^2}{2m_2} \ln \frac{m_2 + 1}{m_2 - 1} \quad . \qquad \text{Equation 2.22}$$

The approximation $\xi = \dfrac{2}{m_2 + (2/3)}$ can be made for values of m_2 greater than 10 (Green and Hamman, 1971). When a neutron is being slowed down from an energy E_0 to an energy E_f, it undergoes an average number of collisions = $\dfrac{\ln(E_0 / E_f)}{\xi}$, and the average energy of the neutron after a collision is given by Equation 2.23 (Green and Hamman, 1971),

$$\overline{E_1} = \frac{E_0}{2}\left[1 + \left(\frac{m_2 - 1}{m_2 + 1}\right)^2\right] \quad . \qquad \text{Equation 2.23}$$

The energy spectrum of recoiling nuclei is nearly uniform between $E_{2\min}$ and $E_{2\max}$, and the minimum energy that can be imparted to a recoiling nucleus is zero. Therefore, the average energy of a recoiling nucleus is half the maximum value as shown in Equation 2.24 (Green and Hamman, 1971),

$$\overline{E_2} = (1/2)E_0(1-r^2) \ .$$ Equation 2.24

For neutrons of energies above 1 MeV, the cross-sections for elastic scattering and absorption plus inelastic scattering both approach the nucleus' geometrical cross-section. Therefore, for a nucleus of radius R, the total cross-section tends to $2\pi R^2$ (Green and Hamman, 1971).

Equation 2.25 gives the relationship between the displacement cross-section and the scattering cross-section (Green and Hamman, 1971),

$$\sigma_d = \sigma_s \left(1 - \frac{m_2 E_d}{4E_0}\right), \quad \text{Equation 2.25}$$

where E_d is the displacement threshold energy. For $E_0 \gg E_d$, $\sigma_d \cong \sigma_s$.

2.5 Simulation packages for radiation interaction with matter

Scientists and engineers have done a significant amount of work to develop software and simulation codes to implement the interactions and mechanisms discussed in sections 2.3 and 2.4. In fact, more elaborate models are implemented in software to cater for various boundary conditions, corpuscular and electromagnetic interactions, high and low energy interactions. Platforms such as GEANT4 (GEANT-4 Collaboration, 2003; Allison *et al.*, 2006), SRIM (Ziegler *et al.*, 2010), and FLUKA (Ferrari *et al.*, 2005; Böhlen *et al*., 2014) offer very accurate and reliable solutions to the understanding of the interaction of radiation with matter.

Specific to space radiation and how it relates to spacecraft design and mission assurance, platforms such as SPENVIS[6], OMERE[7] and MC-Oracle (Wrobel and Saigne, 2011) offer very reliable simulation results (soft error rates, solar panel degradation, single event upset cross-sections, etc.). GEANT4 tools such as GEMAT[8] and MULASSIS[9] interface with SPENVIS and allow users to define shielding materials and to simulate specific material geometries (including semiconductor devices). Another GEANT-4 tool, GRAS, deals with common radiation analyses, such as TID, NIEL and equivalent dose (Santin *et al*., 2005).

2.6 Conclusion

This chapter covered the different aspects of the space environment and described the different types of radiation that can be encountered in space, their sources and how they

[6] https://www.spenvis.oma.be/
[7] http://www.trad.fr/OMERE-Software.html
[8] http://reat.space.qinetiq.com/gemat/
[9] http://reat.space.qinetiq.com/mulassis/

interact with matter. Because this work is primarily for space applications, this chapter is very important in the understanding of the relevance of the results obtained in this work. It describes the environment in which the coating prepared in this work is to operate. It also describes the radiation it is to interact with for the mitigation of their effects. The next chapter describes the method of preparation of this coating.

Chapter 3 Pulsed Laser Deposition

3.1 Introduction

In this work, coatings are grown on integrated circuits using pulsed laser deposition (PLD). It is therefore important to describe this coating deposition technique. This chapter describes the main aspects of PLD, including laser-target interaction, plasma plume expansion dynamics, film nucleation and growth at the substrate. It also briefly describes a typical PLD experimental set-up.

3.2 Background

The historical development of PLD begins with Albert Einstein's postulate on the stimulated emission process when he published the paper (English translation) "*On the Quantum Theory of Radiation"* (Einstein, 1917). The next significant step was the invention of the first laser (a Ruby laser) in 1960 (Maiman, 1960). Although laser evaporation was first used as a thin film deposition technique in 1965 using Maiman's Ruby laser (Smith and Turner, 1965), it was only in the 1980s that it was rapidly developed (Dijkkamp *et al*., 1987; Venkatesan *et al.*, 1988; Inam *et al.*, 1988). Since then, this physical vapour deposition technique has been used to grow epitaxial thin films of oxide materials, among others.

PLD is based on the evaporation of material by a pulsed and highly energetic laser which is focused by a lens onto a solid target. If the laser energy density is high enough to evaporate the material, the latter evaporates into gas plasma having a characteristic plume shape. This plume expands in a direction normal to the target onto a substrate placed in front of the target. The part of the plume that reaches the substrate forms a thin film on the latter. Following this description, one can break down the PLD process into 4 regimes:

- The laser-target interaction during which the surface of the target is evaporated. This is the evaporation regime.
- The laser-plasma interaction which results in isothermal expanding plasma. This is the isothermal regime.
- The expansion of the plasma, which is an isotropic, three-dimensional adiabatic expansion and it occurs with a rapid transfer of thermal energy of the plasma species into kinetic energy.
- The growth of the thin film on the substrate.

Instead of a single comprehensive theoretical model explaining the whole of PLD, there are several models, each analysing a specific aspect of PLD in detail, such as vaporisation (Gibert *et al.*, 1993), plasma formation (Phipps *et al*., 1988; Boardman *et al.*, 1996), and expansion in vacuum (Singh and Narayan, 1990; Anisimov *et al*., 1996) or in an ambient gas (Predtechensky and Mayorov, 1990; Arnold *et al*., 1993). This is because the complex nature of the correlation between the physical phenomena involved in PLD allows for only an approximated description of the latter. In the presence of an ambient gas, for instance, plasma expansion dynamics becomes complex to study due to additional physical phenomena, such as shock-wave formation, plume deceleration and splitting, and thermalisation (Wood *et al*., 1997; Itina *et al*., 1998; Harilal *et al*., 2003).

Figure 3.1 shows a typical PLD experimental set-up. The deposition takes place in an ultra high vacuum chamber. A laser beam of desired energy and fluence is focussed on a target of interest in order to ablate the target into a plasma plume that will in turn expand onto a substrate to form a film on its surface.

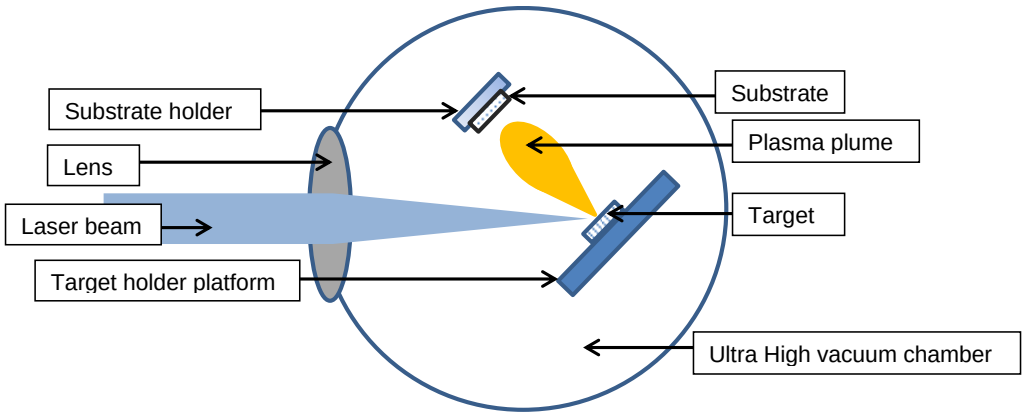

Figure 3.1: A typical PLD experimental set-up

The target to be ablated is mounted onto a target holder platform such that it is struck at an angle of 45^0. This platform is made to rotate and translate appropriately along the plane of the ablated surface to ensure uniform ablation of the target surface while maintaining the 45^0 ablation angle. Substrates are mounted on substrate holders such that they are parallel to, and typically 2-10 cm away from the surface of the target. The substrate holders are mounted with a heating element to allow for experimental conditions that require the substrate to be heated up. In general, substrates up to about 2 cm x 2 cm in dimension are used. This is because larger substrates are too larget for the technique as the resulting films would not be uniform and the substrates may not be coated at all towards their boundaries. However, some set-ups have substrate holders that can rotate and translate to coat larger surfaces.

In this work, the PLD was done using a Q-switched 3rd harmonic Nd YAG (Spectra Physics) laser with a wavelength of 355 nm and a frequency of 10 Hz (pulse width = 2-3 ns). The target used was a B_4C/W_2B_5 pellet in the shape of a regular hexagon. Its diameter was 25 mm, its height was 6 mm, and it weighed 6.23 g. The substrates used were cut from soda lime glass (about 1 cm x 1 cm). The substrate holder was not equipped with rotation and translation capabilities, so only small samples could be synthesised.

3.3 PLD mechanisms

PLD can be described simply as a thin film deposition technique in which a pulsed laser is focused on a solid target with enough energy to ablate the latter into a plasma plume which expands and forms a film onto a substrate. Generally, the stoichiometry of the target is conserved and the resulting film has the same stoichiometry. The mechanisms involved in this process include the laser-target interaction, the laser-plasma interaction, the plasma plume expansion, plume-substrate interaction and the film growth (Ngom, 2010).

3.3.1 Laser-target interaction

When the laser beam fluence is enough to raise the local temperature of the target material to a temperature higher than its vaporisation temperature, laser ablation occurs. The factors that affect this interaction include the target absorption coefficient and reflectivity, the pulse duration τ, the laser wavelength λ and fluence F. Each material has a corresponding threshold laser fluence F_{th} such that for laser fluences greater than F_{th} the laser-target interaction regime is called ablation and for fluences less than F_{th} the laser-target interaction is called desorbsion (Ngom, 2010).

The exact analytical description of this interaction is extremely complex. This is because of the fact that the laser-target interface is moving, and that the melting and evaporation of the target material are target-specific due to a dependence on the optical and thermal properties of the material. As a result, this interaction is described using a macroscopic approach. The ablation volume on the target can be defined by the product of the laser beam cross-section and the depth of the ablation volume into the target. This depth L_{th} is determined as (Allen, 1987; Corkum *et al*., 1988; Bauerle, 2000)

$$L_{th} = \sqrt{2D\tau_L} \quad , \qquad \text{Equation 3.1}$$

where D is the thermal diffusivity of the target and τ_L is the pulse duration.

It can be assumed that the temperature gradient in the direction transverse to the target is insignificant compared to the temperature gradient in the direction normal to the target. The

temperature distribution, which is a function of both space and time, can therefore be approximated such that it is represented by the one-dimensional heat equation (Ready, 1971; Allen, 1987; Peterlongo *et al*., 1994). This approximation, however, may not be appropriate if the target material is known to exhibit lateral diffusion of energy incidenced on it.

The energy in the laser photons is absorbed by electrons in the atomic lattice of the target and transferred through electron-phonon coupling. The interaction of electrons and the atomic lattice in space and time can be described with the two-temperature diffusion model (Anisimov *et al.*, 1974; Qui and Tien, 1993) with the use of two different temperatures: the electron temperature T_e and the lattice temperature T_l (Kaganov *et al*., 1957; Peterlongo *et al*., 1994; Chichkov *et al*, 1996; Nolte *et al*., 1997; Anisimov and Luk'yanchuk, 2002). For nanosecond pulsed lasers, however, the electron-phonon coupling takes place on the picosecond time scale, and it can therefore be assumed that $T_e = T_l = T$. The one-dimensional heat equation approximation describing the ablation process for nanosecond laser pulses can be expressed as given by Equation 3.2 (Ngom, 2010)

$$C_i \frac{\partial T}{\partial t} = \frac{\partial}{\partial z}\left(k_0 \frac{\partial T}{\partial z} \right) + \alpha A I(t) e^{-\alpha z} \text{ ,} \qquad \text{Equation 3.2}$$

where C_i is the heat capacitance of the lattice, $I(t)$ is the laser intensity, k_0 is the thermal conductivity and α the absorption coefficient.

3.3.2 Laser-plasma interaction

The laser-plasma interaction depends on the pulse duration. The forming plasma interacts with the 'tail' of a nanosecond laser pulse, but does not interact at all with a femtosecond laser pulse (Ngom, 2010). When the laser interacts with the forming plasma, the efficiency of the energy deposition in the target material is reduced as some energy is lost in the plasma. This lost energy increases the ionisation in the plasma, rendering the plume expansion even more complex. The plasma temperature rises rapidly, accelerating the electrons further. These electrons in turn emit photons that cause the characteristic brightness of the PLD plasma plume. The plasma mainly absorbs energy through inverse Bremsstrahlung and photo-ionisation (Zel'dovic and Raizer, 1966; Ready, 1971; Dreyfus, 1993).

3.3.3 Plume expansion

The characteristic elliptical shape of the plasma (plume) is due to the fact that the plasma expands in the direction of maximum pressure gradient, which is the axial direction. The plume, however, is more hemispherical in the presence of an ambient gas because the plume front compresses the background gas as it expands.

Because PLD can be done in vacuum or in the presence of an ambient gas, the plume expansion is described both in vacuum and in the presence of an ambient gas.

In vacuum, the plume expands with a free linear behaviour and a weak fluorescence near the target, which is where collisions occur immediately after the termination of the laser pulse (Ngom, 2010). Singh and Narayan (1990) and Anasimov *et al*. (1996) are key references for describing the plume expansion in vacuum. Both models propose an adiabatic plume expansion in which the initial, purely thermal plume energy is progressively converted to kinetic energy as the expansion progresses. The plume front dynamics becomes linear after a short transient time and reaches a maximum asymptotic expansion velocity when all the thermal energy is converted to kinetic energy.

The models describing the plume expansion in an ambient gas include those proposed by Predtechensky and Mayorov (1993), Itina *et al*. (1998), and Arnold *et al*. (1999).

At the initial stages of the plume expansion, the plume velocity was experimentally shown to be very close to that of the plume expansion in vacuum (about 10^6 cm s^{-1}) (Dyer *et al*., 1990; Anisimov *et al.*, 1996; Amoruso *et al.*, 2006). This confirms the hypothesis which predicts this similarity in velocity by proposing that the mass of the plume at the initial stages of the expansion is very large compared to the mass of the ambient gas at the plume front, making the latter insignificant (similar to the case of expansion in vacuum). As the plume expands, the mass of the plume front increases as it includes the mass of the background gas being swept away.

Predtechensky and Mayorov (1993) developed a model describing the dynamics of a hemispherical expansion of the plume front into the ambient gas. Here, as the plume expands, the mass of the ambient gas at the plume periphery expands gradually. This reduces the plume front expansion velocity until a stopping stage is reached.

Arnold *et al*. (1999) developed a more complete model which also considers the effects of the plume-ambient gas interaction on the internal structure of the plume itself. In this model, the plume has two thin layers in contact. One layer is at the contact front with the ambient gas (external) and another is along the plume edge (internal). As the plume expands, the total mass of the ambient gas particles and the ablated material at the contact front (external layer) increases. When this mass is equal or greater than that of the ablated particles on the internal layer, the expansion velocity reduces. The collisions at the plume front between the plasma particles and the ambient gas molecules result in an increase in temperature. This, in addition to the counter-pressure caused by the slowing down of the plume front, results in the reflection of plasma particles as they collide with gas molecules at the external layer. An

internal shock wave thus propagates towards the centre of the plume. Most of the plume energy becomes thermal as the shock wave reaches the centre of the plume. This model does not consider further reflections of the shock wave and considers the plume to be homogenous when the wave reaches its centre. This model also does not account for what happens when the plume stops expanding. Indeed, it has been reported that plume species could reach a substrate at a distance greater than the stopping distance of the plume, and that this was attributed to diffusion (Amoruso *et al*., 2004).

Plume expansion in an ambient gas was also described in terms of experimental pressure ranges of the ambient gas, the energy of the plasma particles and the time evolution of the expansion (Kumuduni *et al*., 1993; Okhoshi *et al*., 1994; Dang *et al*., 1999).

The drag-force model (Geohegan, 1994) is appropriate to describe the early stages of plume expansion in an ambient gas at low pressure. In this model, the ablated particles experience a viscous force proportional to their velocity as they travel through the ambient gas, such that the plume front position is as given by Equation 3.3 (Geohegan, 1994; Ngom, 2010),

$$R = R_0\left(1 - e^{-\beta t}\right) \qquad \text{Equation 3.3}$$

where β is a slowing coefficient, R is the position of the plume front edge and R_0 is the distance at which plume expansion stops. R_0 and β are parameters which are intimately linked with the expansion phenomenon and as such, must necessarily be determined through curve fitting of experimental data. Some referenced sources estimate the stopping distance to be more than one order of magnitude larger than the calculated inelastic mean free path (Geohegan, 1994; Gonzalo *et al*., 1997). It is presumed that this is due to the complex dependence of R_0 on experimental parameters, such as the nature of the ambient gas, its pressure, plasma mass and energy, and target atomic mass ratio. At higher ambient gas pressures, the drag-force model predicts distances which are shorter than those observed experimentally, which makes this model inappropriate for higher ambient gas pressures (Ngom, 2010).

The blast wave model, which was developed to describe the propagation of a shock wave through a background gas after an explosion, is appropriate to describe the plume expansion at higher ambient gas pressures (Zel'dovic and Raizer, 1966; Dyer *et al*., 1990). In this model, the plasma expands and pushes the ambient gas molecules at a supersonic velocity, creating a shock wave ahead of the plume front. This shock wave is followed by an expansion wave which gradually reduces the shock strength. The position of the plume front edge is given by Equation 3.4 (Ngom, 2010),

$$R = \xi_0 \left(\frac{E}{\rho_0} \right)^{1/5} t^{2/5} \ , \qquad \text{Equation 3.4}$$

where ξ_0 ~ 1 is a factor related to thermodynamic and geometric quantities, E is the plasma energy and ρ_0 is the density of the undisturbed ambient gas. The shock wave can only be observed in a region defined by $\left(\frac{3M_0}{4\pi\rho_0} \right)^{1/3} \ll R \ll \left(\frac{E}{P_0} \right)^{1/3}$, where M_0 is the mass of the expanding plasma and P_0 is the pressure ahead of the shock wave front (Kumuduni *et al*., 1993; Geohegan, 1994). The temperature, pressure and diffusion processes within the shock region can be treated using the work of Landau and Lifshitz (1987).

The plasma generated in PLD experiments exhibits behaviours consistent with a mixture of the drag-force model and the blast wave model. The early stages of the expansion agree well with the drag-force model. After the viscous slowing of the plasma front edge forms the shock wave front, the expansion agrees well with the blast wave model (Ngom, 2010). Arnold *et al*. (1999), however, proposed an analytical approach describing the complete dynamics of the plasma plume in an ambient gas in space and time for any pressure.

3.3.4 Plume-substrate interaction

The interaction between the plasma plume and the substrate occurs instantaneously at every laser pulse. The deposition of the plasma species on the substrate can therefore be viewed as separate and random. The parameters which determine this deposition are the laser energy density at the target, the distance between the target and the substrate and ambient gas mass and pressure (Ngom, 2010). The deposition rate in PLD is of the order of 10^{20} atoms $cm^{-2}s^{-1}$ (Rijnders, 2001; Huijben, 2009). This high deposition rate leads to a high super-saturation rate defined by Equation 3.5 (Ngom, 2010),

$$\Delta\mu = k_B T \ln\left(\frac{R_{rate}}{R_0} \right) \qquad \text{Equation 3.5}$$

where k_B is the Boltzmann's constant, R_{rate} is the deposition rate, and R_0 is the equilibrium value at temperature T. This high super-saturation rate is extremely important because if the gas (vaporised target plasma) is not super-saturated, its state will not transit from gaseous to solid on the substrate (Ngom, 2010). This transition is due to local fluctuations (due to kinetic processes) from equilibrium. A resulting high nucleation rate starts the film growth process. When the nuclei reach a critical density, islands start forming and the plume-substrate interaction ends when the islands coalesce.

3.3.5 Film growth

It is worth mentioning that the various growth modes used to explain film growth in PLD are not specific to PLD but apply to physical vapour depositions in general. In fact, they were developed before PLD was invented.

These growth modes differ in the thermodynamic balance between the free energy of the film (γ_F), the substrate (γ_S) and the interface between them (γ_I) (Ngom, 2010).

Also of interest are homoepitaxy and heteroepitaxy . In homoepitaxy, the substrate compounds are the same as those of the film deposited on it. The substrate crystallography extends into the film as it grows. In heteroepitaxy, the substrate and film are made up of different materials leading to a lattice mismatch during film growth. This mismatch causes tensile and/or compressive strain in the growing film (Ngom, 2010).

When $\gamma_F + \gamma_I < \gamma_S$, significant wetting is expected, leading to a layer to layer film growth. This growth mode was proposed by Frank and Van der Merwe (1949). This is generally the case in homoepitaxy.

When $\gamma_F + \gamma_I > \gamma_S$, wetting is unfavourable, leading to island growth rather than layers. This is the Volmer-Weber film growth mode (Volmer and Weber, 1926). This is generally the case in heteroepitaxy with little to moderate interface energies between the substrate and the film.

When there is sufficient mismatch between the film and the substrate, and enough strain on the film being grown, an intermediate film growth mode is observed. In the early stages, a layer by layer growth occurs (Frank-Van der Merwe growth). The elastic energy due to the strain in the film increases with its thickness. This strain energy is relaxed by the formation of islands. The film continues growing following a Volmer-Weber growth. This is the Stranski-Krastanov growth mode (Stranski and Krastanov, 1938). This is generally the case in heteroepitaxy with large interface energies between the substrate and the film.

3.4 Conclusion

This chapter covered the main aspects of PLD. This deposition technique is used for the thin film deposition in this work because a wide range of materials, including oxides, nitrides, polymers and even metals, can be prepared at temperatures as low as room temperature (Ngom, 2010). This is particularly useful as we ablate a composite ceramic target for the first time, and it is not desirable to heat the electronic component(s) we coat with the resulting film. The following chapter describes the synthesis of the coating using PLD and its subsequent characterisation and irradiation.

Chapter 4 Low energy proton irradiation of coatings deposited by the laser ablation of W_2B_5/B_4C

4.1 Introduction

This chapter covers the synthesis, characterisation and effects of irradiation of the films proposed as mitigating coating in this work. It details the structural effects of low energy protons on the synthesised films. The effects detailed are those covered within the time and infrastructure framework made available to the author. For the targeted applications, proton energies between 0.8 MeV and 1.5 MeV are relevant. The stable energies on the experiment days were 0.9 MeV and 1 MeV respectively. These energies, on average, have similar effects in terms of SEUs and solar cell degradation. SRIM simulations indicate that a 1 MeV proton will travel about 2 µm deeper than a 0.9 MeV proton in Si, SiO_2, GaAs, InGaP and Ge. In a 90 nm CMOS SRAM device, this means a 1 MeV proton would stop in a momory cell adjacent to the cell in which a 0.9 MeV proton would stop. In a solar cell, this means both 0.9 MeV and 1 MeV protons would stop in the same junction. Both energies can therefore be considered as equivalent for the purposes of this work.

4.2 Coatings synthesis and characterisation[10]

The coatings were synthesised by the Pulsed Laser Ablation of B_4C/W_2B_5. They were characterised by X-ray Diffraction (XRD), Atomic Force Microscopy (AFM), X-ray Photoelectron Spectroscopy (XPS) and Heavy Ion Elastic Recoil Detection Analysis (ERDA). The characterisation and data analysis lead to a stoichiometry and composition of the coatings.

4.2.1 Preparation conditions for synthesis and characterisation

The target was a B_4C/W_2B_5 pellet in the shape of a regular hexagon. Its diameter was 25 mm, its height was 6 mm, and weight 6.23 g. Its crystal structure, composition properties are described in Chapter 1.

The substrates were cut from soda lime glass (approximately 1 cm by 1 cm in dimension) and cleaned using a BRANSONIC ultrasonic cleaner (70 W, 42 kHz ± 6%). They were immersed in methanol, acetone, trichloroethylene, distilled water and methanol again for 5 minutes each in an ultrasound water bath. Glass was used as substrate for film characterisation purposes.

[10] This section is based on an article that was published by the author, referenced within the document as (Tadadjeu Sokeng *et al.*, 2015b)

The pulsed laser deposition was done using a set-up similar to that described in section 3.4 of Chapter 3, using a Q-switched 3rd harmonic Nd-YAG (Spectra Physics) laser with a wavelength of 355 nm and a frequency of 10 Hz. The beam diameter and energy were set to 2.45 mm and 150 mJ, respectively, corresponding to a laser fluence of 3.183 J/cm^2. The vacuum chamber was kept at a pressure of 5x10^{-5} mbar and at a temperature of 25^{o}C. The target was 3.72 cm away from the substrate. Six samples were deposited for 0.5, 1.5, 3, 4.5, 6 and 7.5 minutes, respectively. Each substrate was attached to a substrate holder in the deposition vacuum chamber using silver paste.

The crystallography of the samples (and target) was investigated by XRD using BRUKER AXS equipment having a D8 Advance diffractometer, a Cu-Kα radiation tube (λKα1=1.5406Å) and a PSD Vantec-1 detector.

The morphology of the samples was investigated by AFM using a Nano-Man V Atomic Force Microscope equipped with a VT-103-3K-2 acoustic enclosure. The tapping operation mode was used.

The depth profiles of the target and samples were obtained by Heavy Ion ERDA using a non-commercial set up and equipment internally developed at iThemba LABS Gauteng, South Africa (Msimanga *et al*., 2013:54-60). These were used to investigate the elemental composition of the target and the thickness of the samples.

The binding energies within the samples were determined by XPS using a PHI 5000 Versaprobe - Scanning ESCA Microprobe. The surveys and high resolution spectra were done with 100 µm, 25 W, 15 kV, Al monochromatic X-ray beam. Sputtering was done 2 kV, 2 µA, 1×1 mm raser using an Ar ion gun with a sputter rate of about 170 Å/min. The peaks were analysed using XPSPEAK41 software with a Shirley background, and a software defined and optimised %Lorenzian-Gaussian fit (combined Lorenzian and Gaussian fits in different optimised percentages).

4.2.2 Characterisation analysis and discussion

Figure 4.1 (Tadadjeu Sokeng *et al.*, 2015b) shows the XRD spectra of each sample produced from the same target. Peaks occurred at 2θ angles of 31.053^0, 35.217^0 and 47.878^0. There was no perfect match, and the closest match was WC. Its peaks were consistently about 0.4^0 to the right of those of the samples. Experiment-related errors were eliminated by completely recalibrating the apparatus and repeating the measurements. In order to determine the lattice parameters of the samples, the hexagonal lattice of WC and its Miller indices were assumed for the sample even though the diffraction angles differed consistently by 0.4^0. These Miller indices are (001) at 31.475^0, (100) at 35.627^0 and (101) at

48.267^0. From the JCPDS 00-025-1047 file, the WC lattice parameters are $a = 2.906\text{Å}$ and $c = 2.838\text{Å}$. Using the miller indices from this same PDF file, the lattice parameters of all the samples were averaged to $a = 2.942\text{Å}$ and $c = 2.879\text{Å}$. The obtained lattice parameters for the deposited samples were greater than the WC parameters by 0.035Å for a and 0.041Å for c. Figure 4.2 (Tadadjeu Sokeng *et al.*, 2015b) shows how the lattice parameters change with deposition time. These lattice parameters were computed based on the analysis of the measured XRD peaks. It is apparent that despite the absence of a trend with respect to deposition time, both parameters a and c increase and decrease consistently (although not by the same value), except for the sample deposited for 6 minutes. This suggests that changes in lattice dimensions are not across a specific plane on the lattice, but rather across the entire lattice. The difference between the lattice parameters of the samples and those of WC suggests an alteration of the WC crystal lattice; possibly the substitution of some of the C atoms with B atoms.

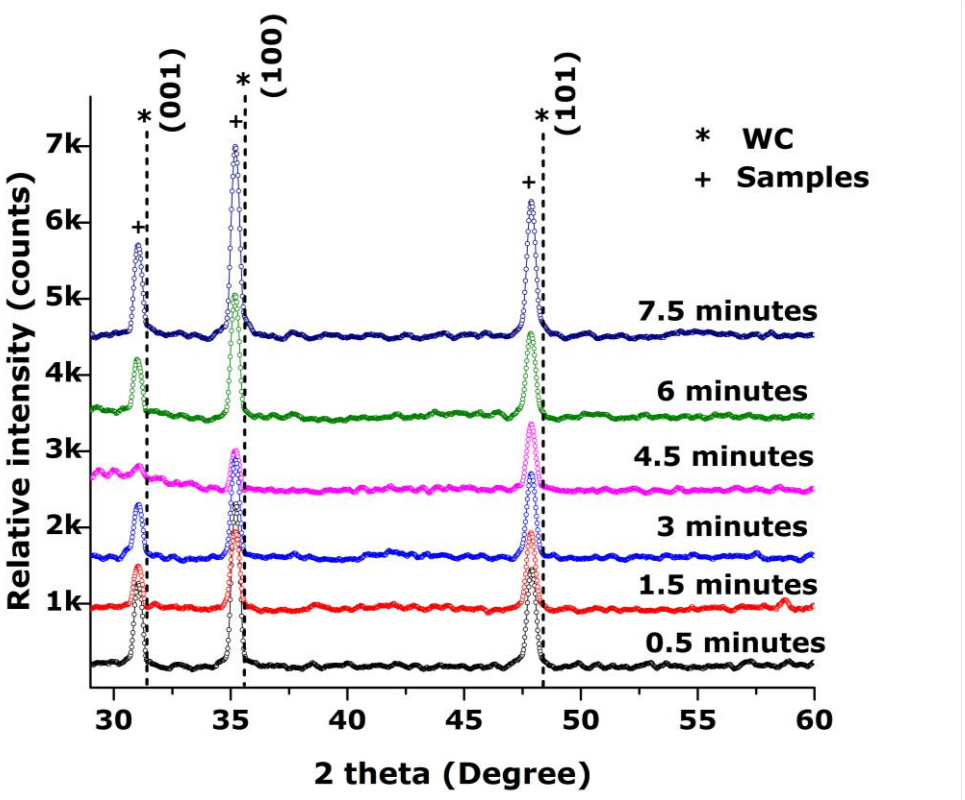

Figure 4.1: XRD spectrum of samples with increasing deposition time. The WC peaks are shown 0.4 degrees to the right of the sample peaks

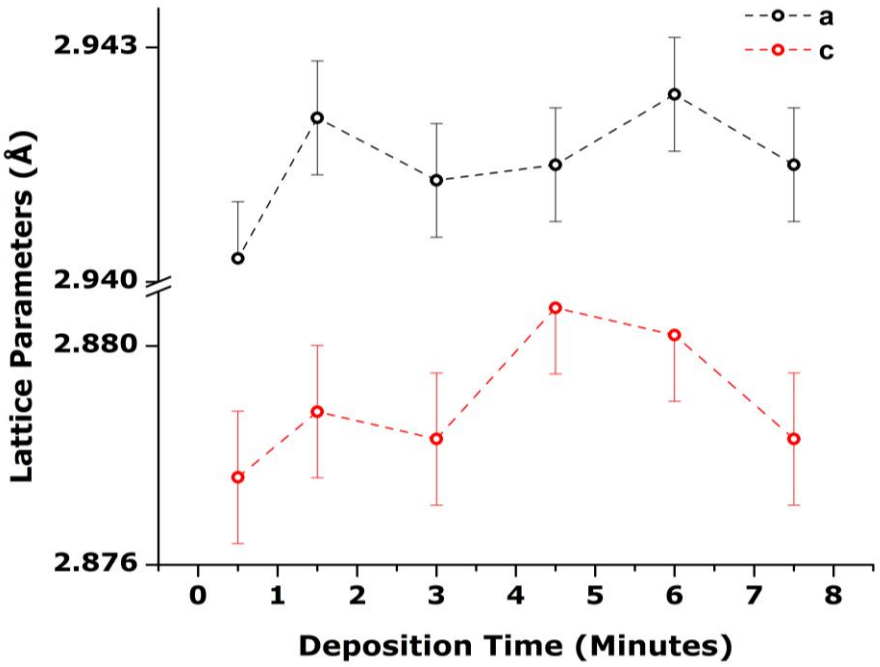

Figure 4.2: Variation of lattice parameters with deposition time. The parameters are computed based on the analysis of the measured XRD peaks

Figure 4.3 (a-f) (Tadadjeu Sokeng *et al.*, 2015b) shows the AFM images of samples deposited for 0.5 minutes through to 7.5 minutes. One can notice an increasing number of droplet-like features from 0.5 minutes to 4.5 minutes (a-d), after which fewer droplet-like features can be observed but many more rod-like features appear, and they increase in number from 4.5 minutes to 7.5 minutes (d-f). As shown in Figure 4.4 (Tadadjeu Sokeng *et al.*, 2015b), the mean peak-to-valley roughness (from the vertical axis in Figure 4.3) seems to be insignificant until a deposition time of 4.5 minutes is reached, after which it increases very rapidly. This is evidence that nucleation, island formation and coalescence (as described in Chapter 3) occur before 4.5 minutes. After this threshold, the roughness of the film becomes significant and increases as the film grows vertically.

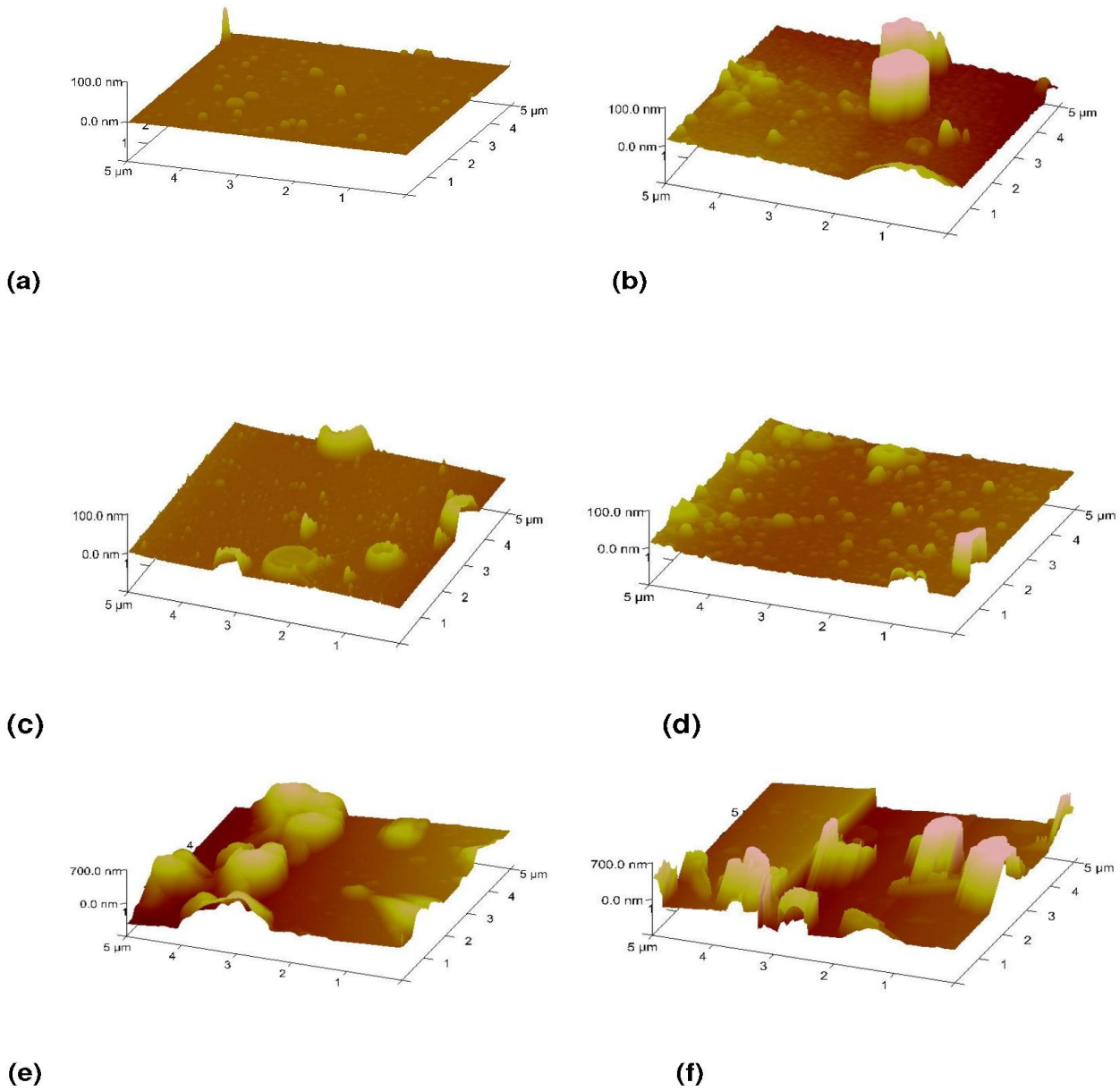

Figure 4.3: **AFM images for samples at different deposition times. (a) 0.5 minutes; (b) 1.5 minutes; (c) 3 minutes; (d) 4.5 minutes; (e) 6 minutes; (f) 7.5 minutes**

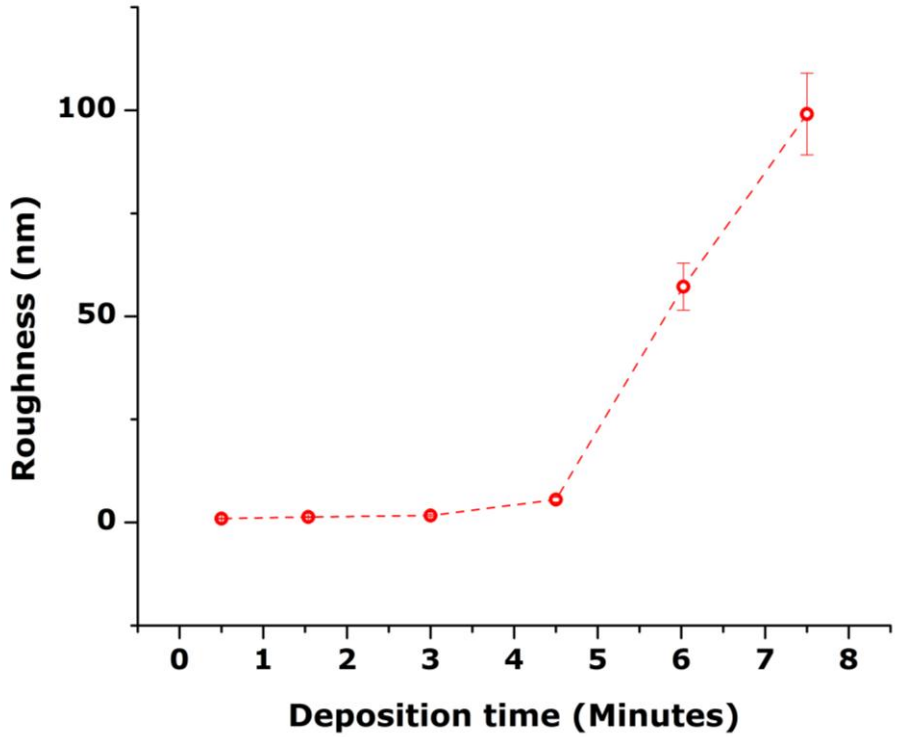

Figure 4.4: Variation of roughness with deposition time

X-ray Photoelectron Spectroscopy (XPS) revealed the presence of B, W and C as well as O, as illustrated in Figure 4.5 and detailed in Table 4.1. The B1s peak with binding energy (E_b) 190.5 eV indicates the presence of B^{2+} ions (Krastev *et al*., 1996:186-192). This is evidence of B atoms available for bonding with both C and W, as well as free B atoms. The peak at E_b = 192.7 eV is attributed to B_2O_3. The C1s peaks include one at E_b = 284.6 eV which is attributed to free C, one at E_b = 285.7 eV which is attributed to C bonded with W and one at E_b = 286.9 eV which is attributed to C bonded with O (Crist, 2007:1-52). The O1s peaks include one at E_b = 533.8 eV attributed to B_2O_3, and peaks at binding energies of 534.6 eV and 535.6 eV that may be attributed to O bonded with C and O bonded with W respectively. The W4f peaks include a W4f7 peak at E_b = 33.7 eV attributed to WC (Beadle *et al*., 2008: 3847-3854; Bhattarai *et al*., 1998:19-42) and a W4f5 peak at E_b = 35.9 eV attributed to W bonded with O (Bera *et al*., 2012:103-105; Ngom *et al*., 2011:6226-6232; Palmquist *et al*., 2003:29-37).

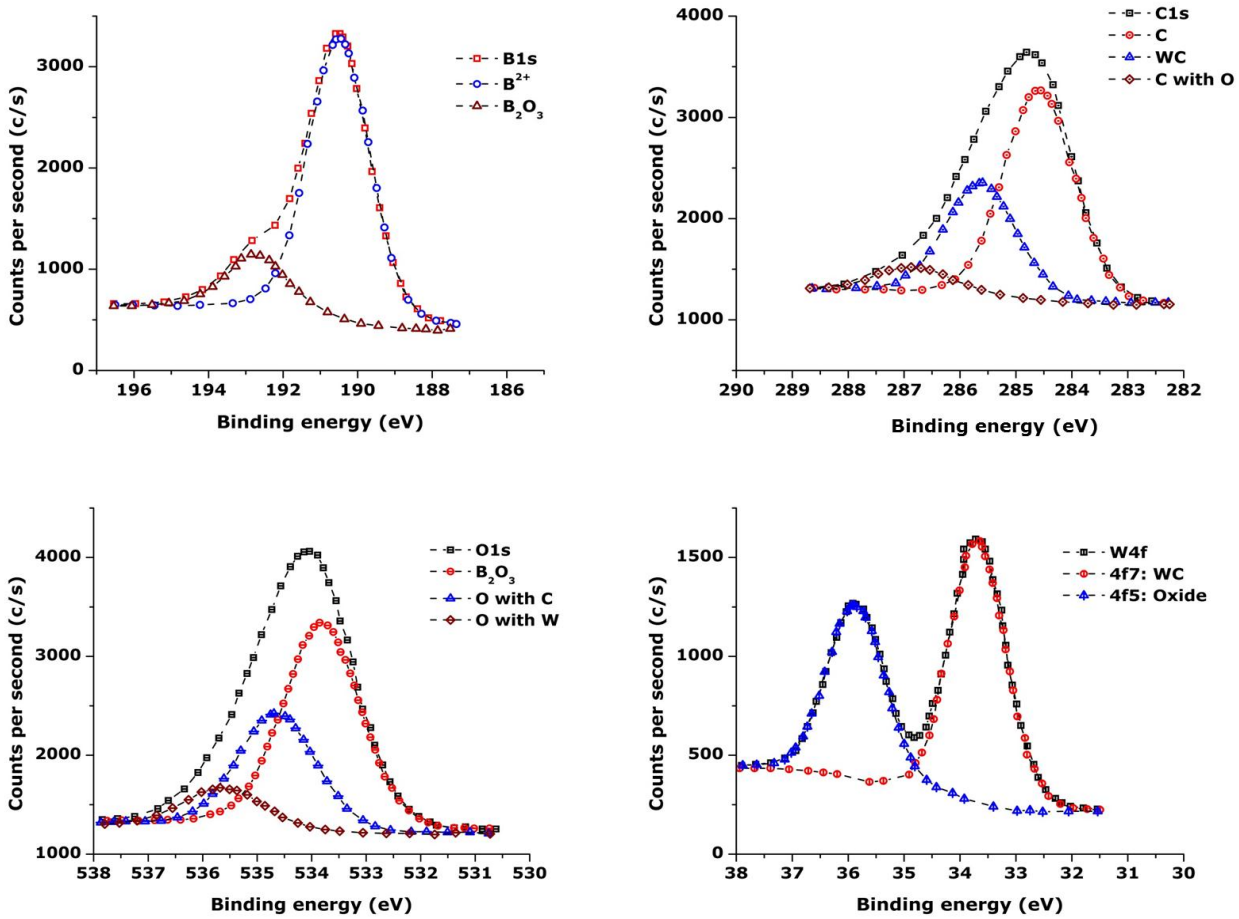

Figure 4.5: **XPS measurements showing the deconvolution of various peaks (a) B1s peak; (b) C1s peak; (c) O1s peak; (d) W4f peaks**

Table 4.1: **Analysis of the coating composition based on XPS measurements**

Sub peaks	Atomic percentage (%)	Binding energy (eV)	Percentage per binding energy (%)	Possible chemical state	Reference
B1s	39	190.5 192.7	31.7226 7.2774	B^{2+} B_2O_3	(Krastev *et al*., 1996:186-192)
C1s	26	284.6 285.7 286.9	15.4622 8.6528 1.885	C WC C with O	(Crist, 2007:1-52)
W4f	3	33.7 (4f7) 35.9 (4f5)	1.7964 1.2036	WC Oxide	(Beadle *et al*., 2008; Bhattarai *et al*., 1998:19-42) (Bera *et al*., 2012:103-105; Ngom *et al*., 2011:6226-6232; Palmquist *et al*., 2003:29-37).
O1s	24	533.8 534.6 535.6	15.8904 6.3792 1.7304	B_2O_3 O with C O with W	

The XPS results suggest that the films contain W-C bonds consistent with WC, and O bonded with C, B and W. While this O is most probably from the oxygen impurity in the target, oxidation needs to be investigated. The results also suggest that it is possible that some B atoms may have replaced some C atoms in the WC lattice to form a solid solution of the form $WC_{1-x}B_x$. Evidence of this solid solution lie in the XRD spectrum, and can be supported by the fact that beta-WC_{1-x} can exist at temperatures greater than 2600^0C (Demetriou *et al*., 2002:1421-1432). These temperatures are possible in PLA and B may have been inserted into the beta-WC_{1-x} phase within the plasma plume to form a hexagonal $WC_{1-x}B_x$ solid solution. The B would therefore have caused a stretch that explains the shift in the XRD peaks. The alpha-WC lattice suggests that each W is bonded to 5 C atoms (Krawitz *et al*., 1989:515-517). Within the lattice, this means a C/W atomic ratio of 5. The C/W ratio in this work, for the C and W atoms attributing to WC is about 4.817, which is further evidence of a doped WC lattice. In terms of stoichiometry, this suggests a $WC_{1-x}B_x$ where 1-x = [(at% C attributed to WC)/5] / (at% W attributed to WC). Using the entries in Table 4.1, this results in x = 0.037, and the proposed solid solution having stoichiometry $WC_{0.963}B_{0.037}$. This stoichiometry is consistent with a WC lattice doped with B.

Heavy Ion ERDA was used to investigate the elemental composition and the thickness of the samples. It reveals the presence of C, B, W and about 10% O contamination. The XPS results, and the absence of O or oxide peaks in the XRD spectra, suggest that both the target and the films are composed of a mixture of crystal forms containing at least C, B and W, and amorphous forms containing at least O. The roughness of the samples may have had a detrimental effect on the resolution and, hence, accuracy in film thickness measurements illustrated in Figure 4.6 (Tadadjeu Sokeng *et al.*, 2015b). Nonetheless, the results demonstrate a trend in film thickness dependence on deposition time. The thickness increases rapidly until a deposition time of 4.5 minutes, after which the increase slows down significantly. Since nucleation, island formation and coalescence can be viewed as a lateral film growth, it is normal that thickness in atoms/cm^2 increases rapidly during this growth which happens in the first 4.5 minutes of deposition. After 4.5 minutes the film growth is vertical and, therefore, the number of atoms per unit area does not increase much. A rough estimate of the thickness in nanometers was obtained using SRIM (see section 2.5 of Chapter 2) to calculate the density in atoms/cm^3. These calculations show that the coatings vary from about 13 nm after 0.5 minutes to about 120 nm after 7.5 minutes. It should be noted, however, that SRIM warns its users that its calculated densities are not always accurate.

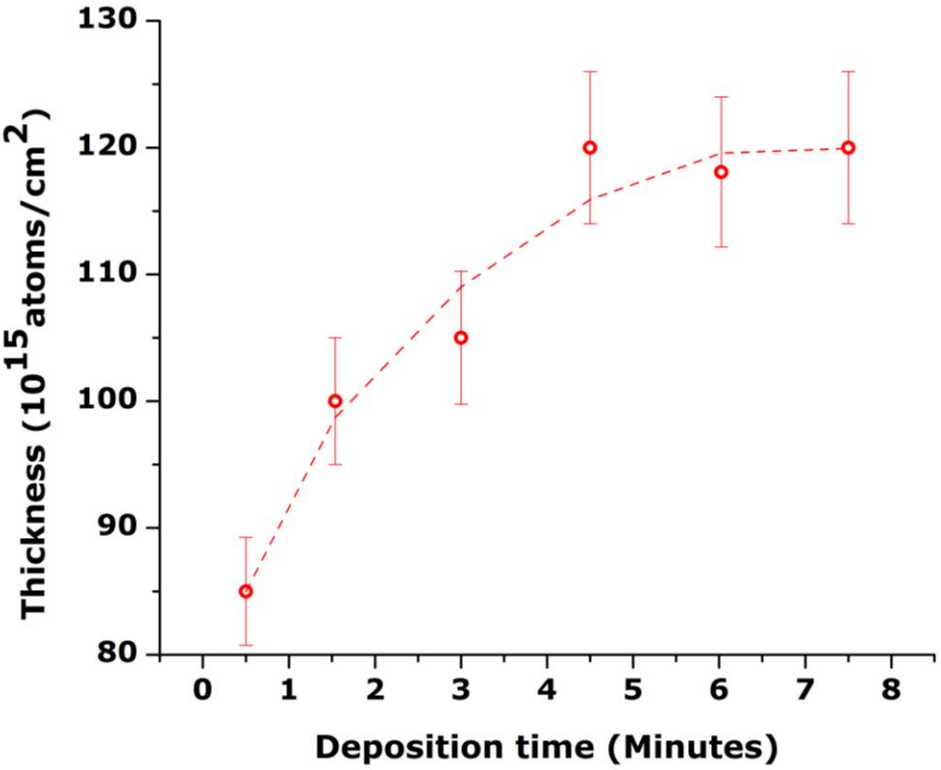

Figure 4.6: Variation of thickness with deposition time

4.3 900 keV proton-induced lateral dispersion of matter and nanorod melting in a $WC_{1-x}B_x$ coating[11]

As part of the investigation of the effects of low energy protons on the synthesised coatings, they were irradiated with 900 keV protons at fluences ranging from about $1x10^{15}$ protons/cm^2 to about $4x10^{15}$ protons/cm^2. Scanning Electron Microscopy (SEM) and Energy Dispersive Spectroscopy (EDS) were used to study the resulting structural effects.

4.3.1 Coating synthesis and irradiation conditions

The substrates used were the same as in section 4.2.1 and they were prepared the same way.

The pulsed laser deposition was done using the same equipment as in section 4.2.1. The laser fluence was 18.05 J/cm^2. The target was 3.7 cm away from the substrate in a vacuum chamber at $4x10^{-5}$ mbar. The deposition was carried out at room temperature and the deposition time was 15 minutes per sample, for 5 different identical samples.

The samples were irradiated with a focused proton beam emanating from a standard Van De Graaf accelerator. The proton energy was set to 900 keV, the beam diameter was 6 mm and the beam current was maintained at 14 nA. The proton flux was $3x10^{11}$ protons/cm^2/s

[11] This section is based on an article that was published by the author, referenced within the document as (Tadadjeu Sokeng *et al.*, 2015a)

and 4 samples were irradiated at fluences ranging from $1x10^{15}$ protons/cm^2 to $4x10^{15}$ protons/cm^2 at room temperature in a vacuum chamber at $5x10^{-6}$ mbar. The 5th sample was not irradiated and was used as control sample.

Scanning Electron Microscopy (SEM) was done with a Zeiss Auriga field emission gun SEM (FEG-SEM) operated at 5 kV for secondary electron imaging, using an inlens detector; and 20 kV for Energy Dispersive Spectroscopy (EDS) analysis. The EDS spectra were collected using an Oxford Instruments X-Max solid-state silicon drift detector

4.3.2 Result analysis and discussion

Figure 4.7(a-e) (Tadadjeu Sokeng *et al*., 2015a) shows the SEM images of the coating as deposited and irradiated at $1x10^{15}$ protons/cm^2, $2x10^{15}$ protons/cm^2, $3x10^{15}$ protons/cm^2 and $4x10^{15}$ protons/cm^2. The as-deposited coating shows clustered nanostructures of no particular shape, as shown in Figure 4.7 (a). These structures are referred to as rods in this work because they look like many irregularly shaped rods ”glued” together. These clusters appear to have formed in the later stages of the film growth, as they are on top of the surface of the film floor, from which they are quite distinct.

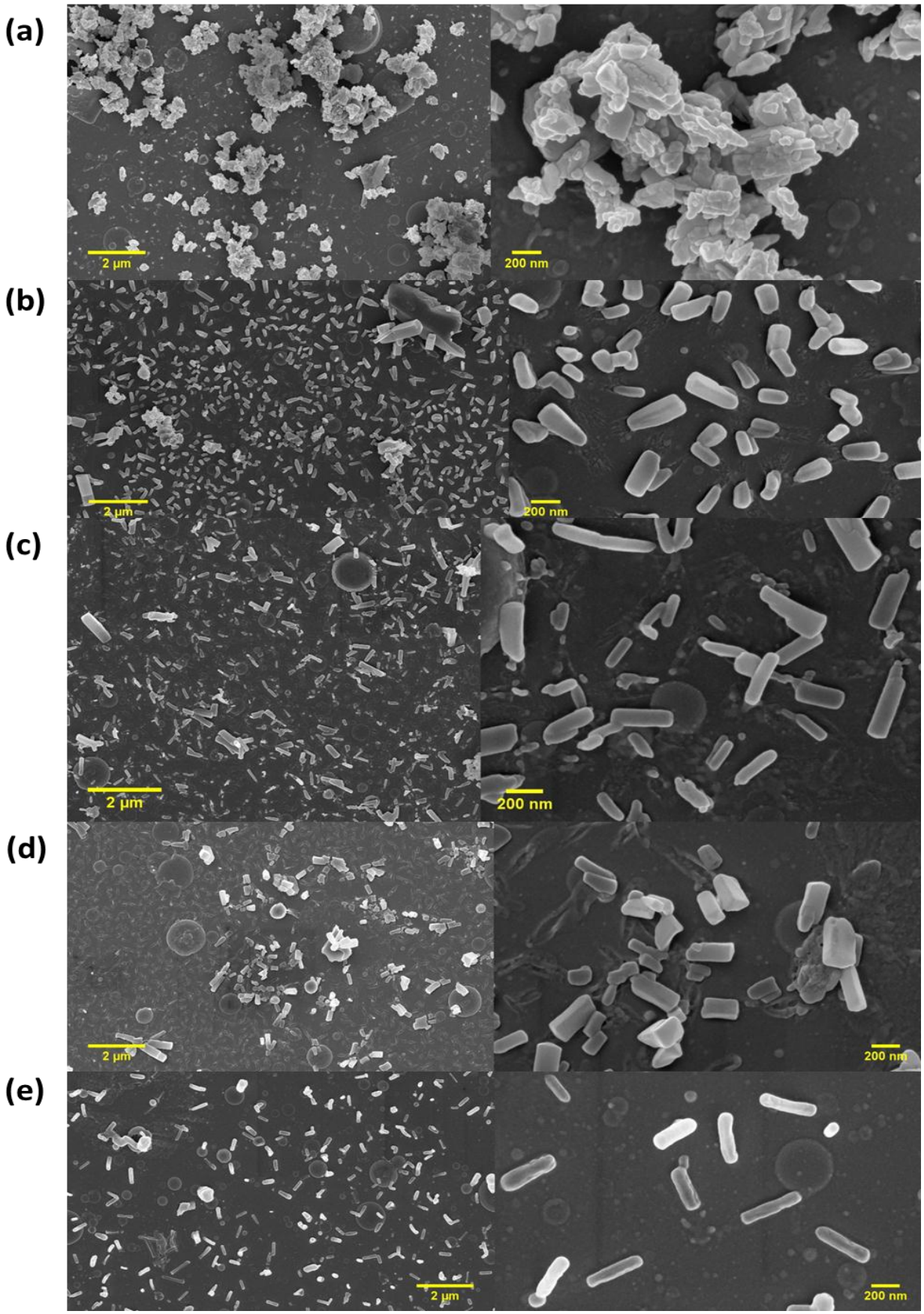

Figure 4.7: **SEM images of non-irradiated and irradiated coatings. (a) As deposited, (b) at $1x10^{15}$ protons/cm^2, (c) at $2x10^{15}$ protons/cm^2, (d) at $3x10^{15}$ protons/cm^2, (e) at $4x10^{15}$ protons/cm^2.**

Tadadjeu Sokeng *et al*. (2015a) points out that the growth mechanism of the coating has characteristics of a Volmer-Weber growth as described in section 3.3.5 of Chapter 3 (favoured by the high laser fluence during deposition). It also has characteristics of a Stranski-Krastanov growth as described in the same section of Chapter 3 (favoured by the thermal expansion coefficient mismatch between the substrate and the coating). A close observation of Figure 4.7 (b-d), in particular on the 200 nm scale, shows an increasing number of features merged with the film floor. These features are absent in Figure 4.7 (a) and Figure 4.7 (e). One can also observe that the rod shapes are not regular, except for those in Figure 4.7 (e), which are uniformly shaped rods about 405 nm long and 90 nm wide. These rods are longer than those in Figure 4.7 (d) (about 320 nm long for the more regular looking rods). This means that the clusters melt as the proton fluence increases from 1×10^{15} protons/cm^2 to $3x10^{15}$ protons/cm^2 (Tadadjeu Sokeng *et al*., 2015a). At $4x10^{15}$ protons/cm^2, no further melting occurs, but instead, the rods which are not molten seem to grow.

Figure 4.8 (Tadadjeu Sokeng *et al*., 2015a) shows the average cluster area as a function of irradiation fluence. This figure shows a decrease in cluster area from the non-irradiated sample to the sample irradiated at $3x10^{15}$ protons/cm^2. This decrease is consistent with melting. The figure also shows a slight increase from 0.29 µm^2 at $3x10^{15}$ protons/cm^2 to 0.38 µm^2 at $4x10^{15}$ protons/cm^2. The average cluster size at fluences of $3x10^{15}$ protons/cm^2 and $4x10^{15}$ protons/cm^2 corresponds to the average area of individual rods, since at those fluences there are little or no agglomerations. The mentioned increase in area therefore suggests rod growth.

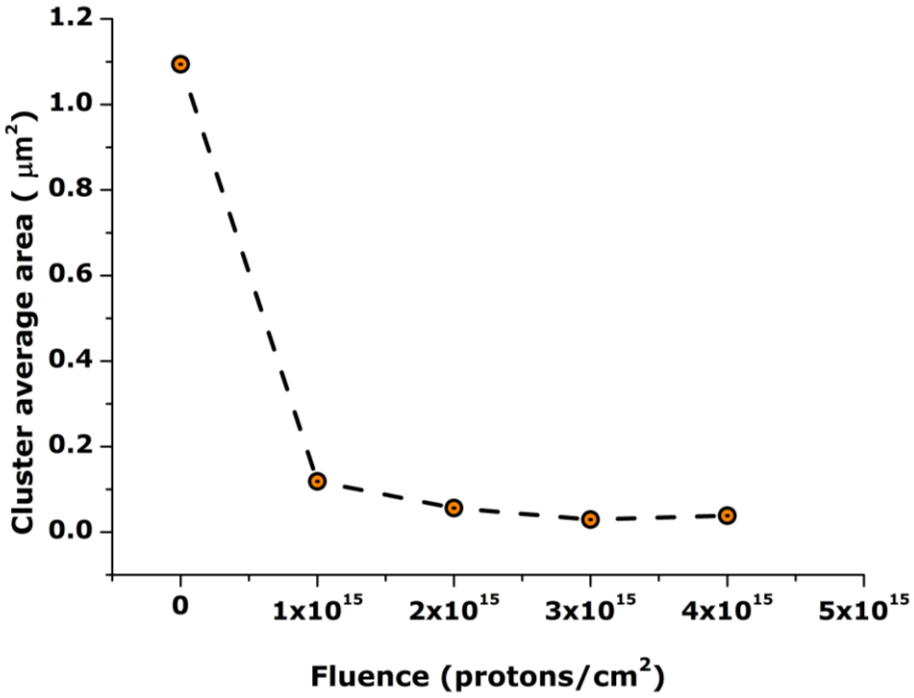

Figure 4.8: Average cluster area as a function of irradiation fluence.

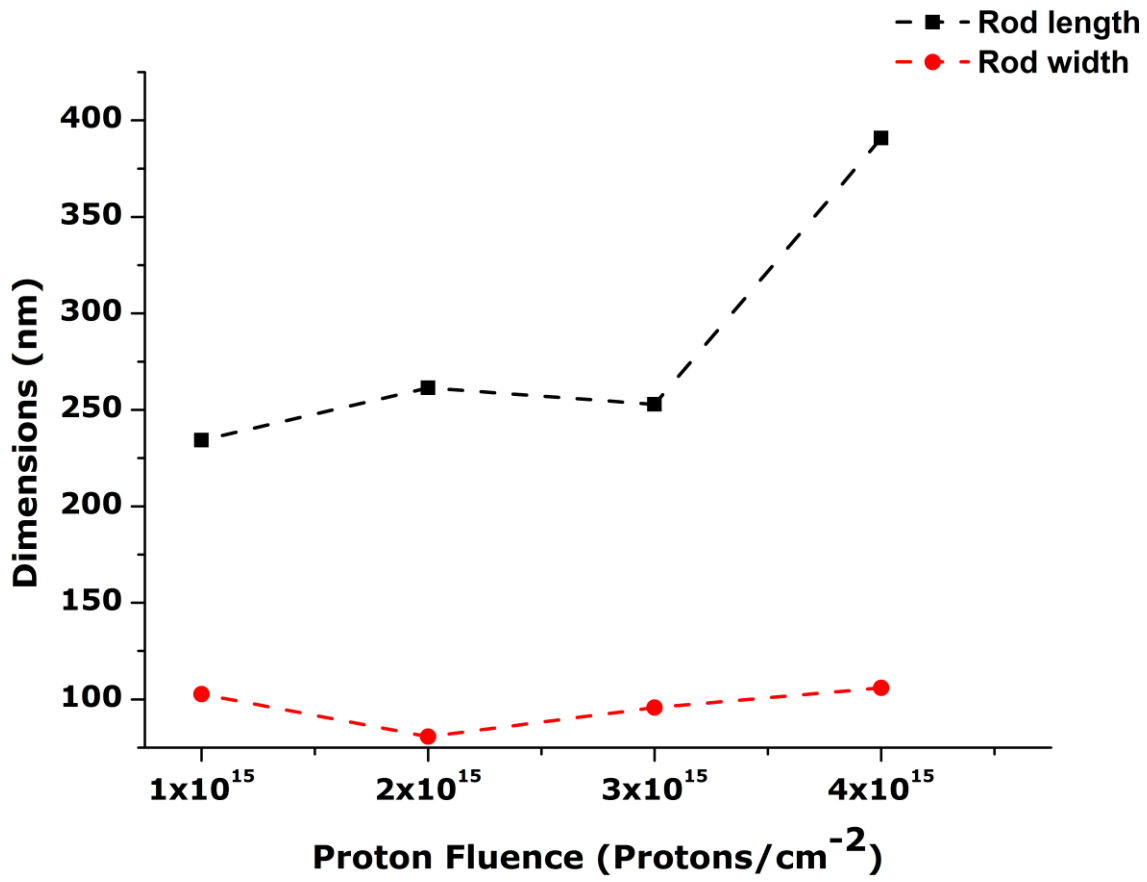

Figure 4.9: Average rod dimensions as a function of irradiation fluence.

In terms of the number of clusters per unit area, averaging over several spots shows a distribution of about 0.07 clusters/μm^2, 1.48 clusters/μm^2, 6.72 clusters/μm^2, 0.23 clusters/μm^2, and 0.60 clusters/μm^2, respectively, for the sample as deposited and for each irradiation fluence. This is normal as the fewer large clusters melt down to many smaller clusters as their constituent nanorods melt (Tadadjeu Sokeng *et al*., 2015a). These clusters in turn reduce in number per unit area as the rods melt further. Figure 4.9 (Tadadjeu Sokeng *et al*., 2015a) shows the average rod dimensions as a function of irradiation fluence. Of interest is the observation that at 4x10^{15} protons/cm^2, there is a considerable increase in average rod length. The corresponding average rod width, however, does not increase as much, but does not decrease either. This is consistent with the slight increase in cluster average area from 0.29 μm^2 at 3x10^{15} protons/cm^2 to 0.38 μm^2 at 4x10^{15} protons/cm^2. These observations support the proposition that after 3x10^{15} protons/cm^2, the melting stops and the growth of regularly shaped rods starts, and this growth can be observed at 4x10^{15} protons/cm^2. EDS measurements were made on a glass substrate and on the samples. This was to eliminate uncertainties related to the composition of the coatings.

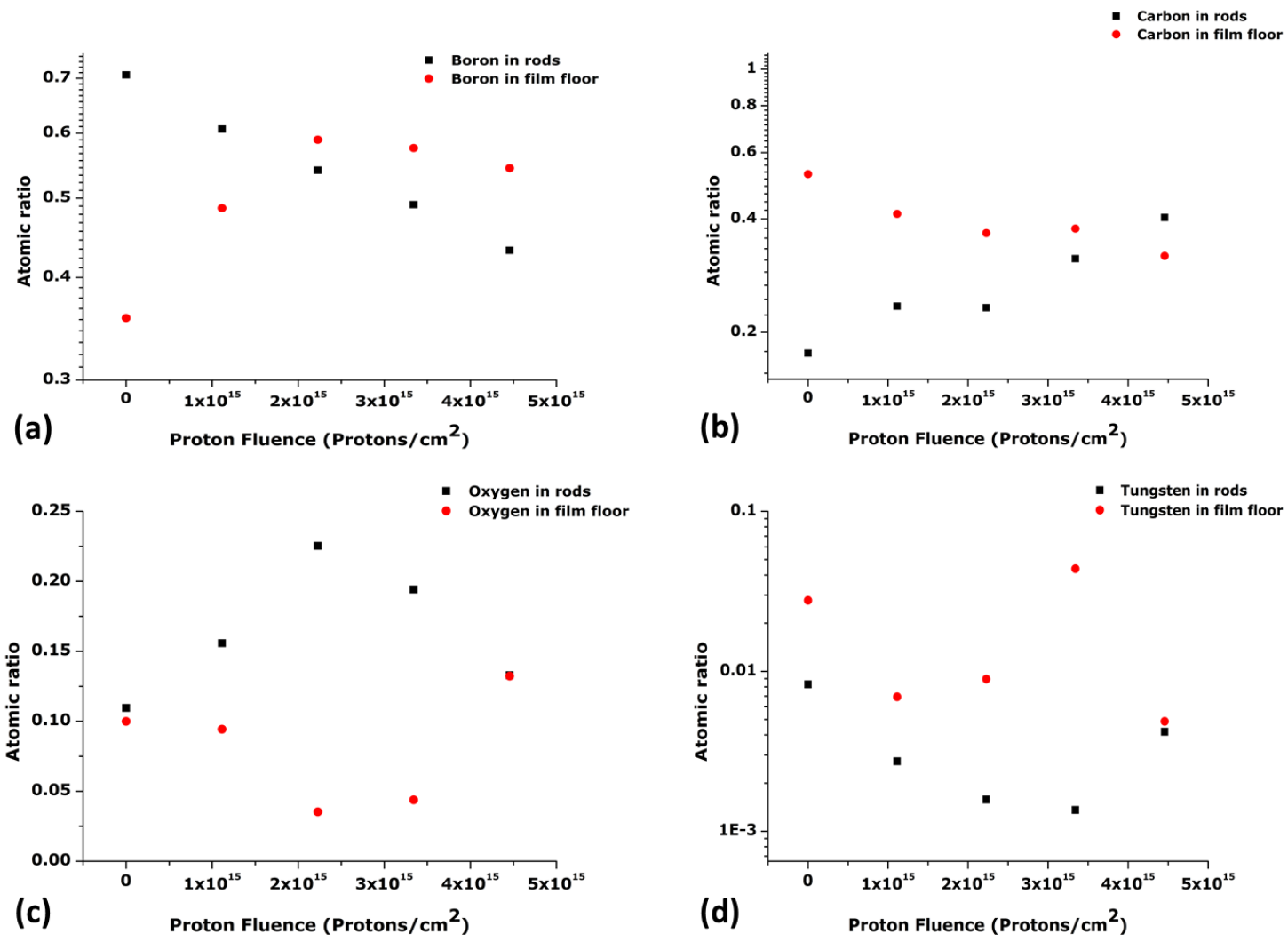

Figure 4.10: Atomic percentage distribution per element as a function of proton fluence. (a) B atomic percentage distribution, (b) C atomic percentage distribution, (c) Oxygen atomic percentage distribution, (d) W atomic percentage distribution.

The atomic percentages of B, C, W and O were computed based on experimental measurements (Tadadjeu Sokeng *et al*., 2015a) and the results are illustrated in Figure 4.10 (a-d) (Tadadjeu Sokeng *et al*., 2015a). It shows the atomic percentages of each element in the coating as a function of proton fluence, both in the rods and in the film floor. These graphs show an inverse relationship between the atomic percentage of each element in the rods and in the floor. In Figure 4.10 (a), B is seen to steadily reduce from the rods while at the same time increasing in the floor as the proton fluence increases. In Figure 4.10 (b), C increases steadily in the rods as it decreases from the floor at the same time with increase in proton fluence. In Figure 4.10 (c), Oxygen Increases in the rods and then drops after $2x10^{15}$ protons/cm^2 while following the inverse trend in the floor. In Figure 4.10 (d), W decreases steadily from the rods and then increases at $4x10^{15}$ protons/cm^2, while following the inverse trend in the floor.

In his analysis, Tadadjeu Sokeng *et al*. (2015a) explained how the above observations lead to the conclusion that energy lost by the protons to the coating melts the nanorods on the latter up to a certain point. This then contributes to the growth of uniformly shaped rods (Tadadjeu Sokeng *et al*., 2015a). Indeed, the interactions described and discussed so far, confirm that the coating transfers the energy from incident protons laterally across its surface rather than normally through itself. This lateral transfer of energy translates into lateral displacement of matter as illustrated in Figure 4.11 (Tadadjeu Sokeng *et al*., 2015a). This figure shows a light microscope image of the sample irradiated at $4x10^{15}$ protons/cm^2 and its surface 3D representation. Clearly visible are the displaced matter wave front and the depression at the irradiated spot from where matter is displaced across the coating.

It is very important to mention that the melting of its surface nanorod clusters, the resulting cluster dispersion and the subsequent growth of uniformly shaped nanorods are key effects making this coating suitable for space applications (Tadadjeu Sokeng *et al*., 2015a).

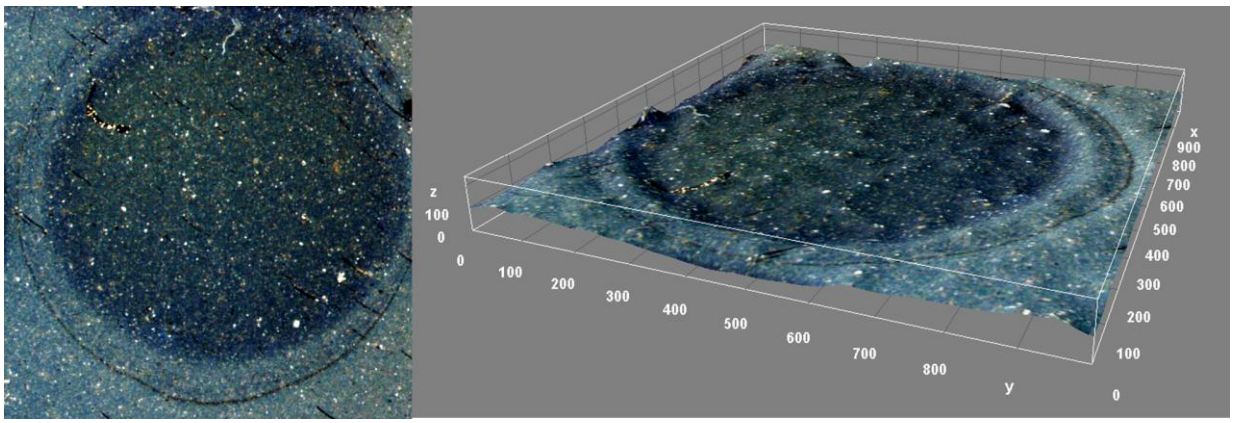

Figure 4.11: Light Microscopy image and surface 3D representation of an irradiated sample showing the wave front of laterally displaced matter.

Indeed, this coating provides an interesting solution to the mitigation of solar panel degradation due to low energy protons in low earth orbit. It also offers a mitigation solution to SEUs due to low energy protons. While the demonstration of these applications would require extensive simulations and testing (which is beyond the scope of this work), it is safe to say that the applicability of this coating is not limited to space.

4.4 1 MeV proton-induced three-stage nanorod melting in a $WC_{1-x}B_x$ coating

In this experiment, the synthesised coatings were irradiated with 1 MeV protons at fluences ranging from about $1x10^{15}$ protons/cm^2 to about $5x10^{15}$ protons/cm^2. Scanning Electron Microscopy (SEM) and Energy Dispersive Spectroscopy (EDS) were used to study the resulting structural effects.

4.4.1 Coating synthesis and irradiation conditions

The synthesis and irradiation conditions were very similar to the experiment described in section 4.3. For the current experiment, the laser fluence was 3.265 J/cm^2, the deposition time 5 minutes for four identical samples, the vacuum chamber pressure 2x10^{-5} mbar, the beam current 10 nA and the proton flux 2x10^{11} protons/cm^2/s. Three samples were irradiated at fluences of 1x10^{15} protons/cm^2, 3x10^{15} protons/cm^2, and 5x10^{15} protons/cm^2, respectively. The fourth sample was not irradiated and was used as control sample.

4.4.2 Result analysis and discussion

Figure 4.12 (a-d) shows the SEM images of the control sample and the samples irradiated at 1x10^{15} protons/cm^2, 3x10^{15} protons/cm^2 and 5x10^{15} protons/cm^2. One can notice the absence of the droplets that characterise PLD in all the samples. This means that during deposition, the laser beam energy was low enough that there was no sub-surface melting when the laser interacted with the target (see section 3.3.1).

Also noticeable is the cracks on the surface of the coatings. These cracks appear on all the samples, meaning they are not caused by irradiation. The atomic percentages of, respectively, B, C, W and O, on top and beneath the cracked surface are approximately the same. This observation strongly suggests a layer-by-layer growth as proposed by Frank and Van der Merwe (1949). There is, however, an inconsistency in that Frank-Van der Merwe growth generally occurs in homoepitaxy, which is not the case of this coating since the subsrate and the coating are made up of different materials. Furthermore, sections 4.2.2 and 4.3.1 have already shown strong evidence of Volmer-Weber growth (Volmer and Weber, 1926) in this coating (consistent with heteroepitaxy, and described in section 3.3.5 of Chapter 3), with coalescence occurring after 4.5 minutes of deposition. The latter observations and remarks are a very strong indication of a different growth mechanism which is consistent with every experiment carried out with this coating so far. This mechanism is the "*reversed Stranski-Krastanov growth mode*" in which, unlike in the Stranski-Krastanov growth mode (Stranski and Krastanov, 1938), the early stages of the growth starts with nucleation, island formation and coalescence (consistent with heteroepitaxy). After coalescence, the film surface becomes an apparent homoepitactic substrate, favouring a Frank-Van der Merwe growth (as described in section 3.3.5 of Chapter 3). Chen *et al*. (2004) reported this mode to grow GaN films on Si(111), but he had to induce it through temperature ramping to 1050 ^{o}C. In this work, this growth mode occurs "naturally" at room temperature under the specified deposition conditions.

Figure 4.12 (a) shows a sample of the rods that are formed on the coating during deposition. These rods are, on average, about 10 μm long and about 1μm wide, except for a few, like the rod in Figure 4.12 (b). On average, there are only about 2 rods in every 100 μm^2.

The formation mechanism of these rods is a mystery, mainly because of their three-stage melting under proton irradiation. Indeed, at $1x10^{15}$ protons/cm^2, as seen in Figure 4.12 (b), the surfaces of the rods appear to “weaken”, revealing a rough pattern from underneath it.

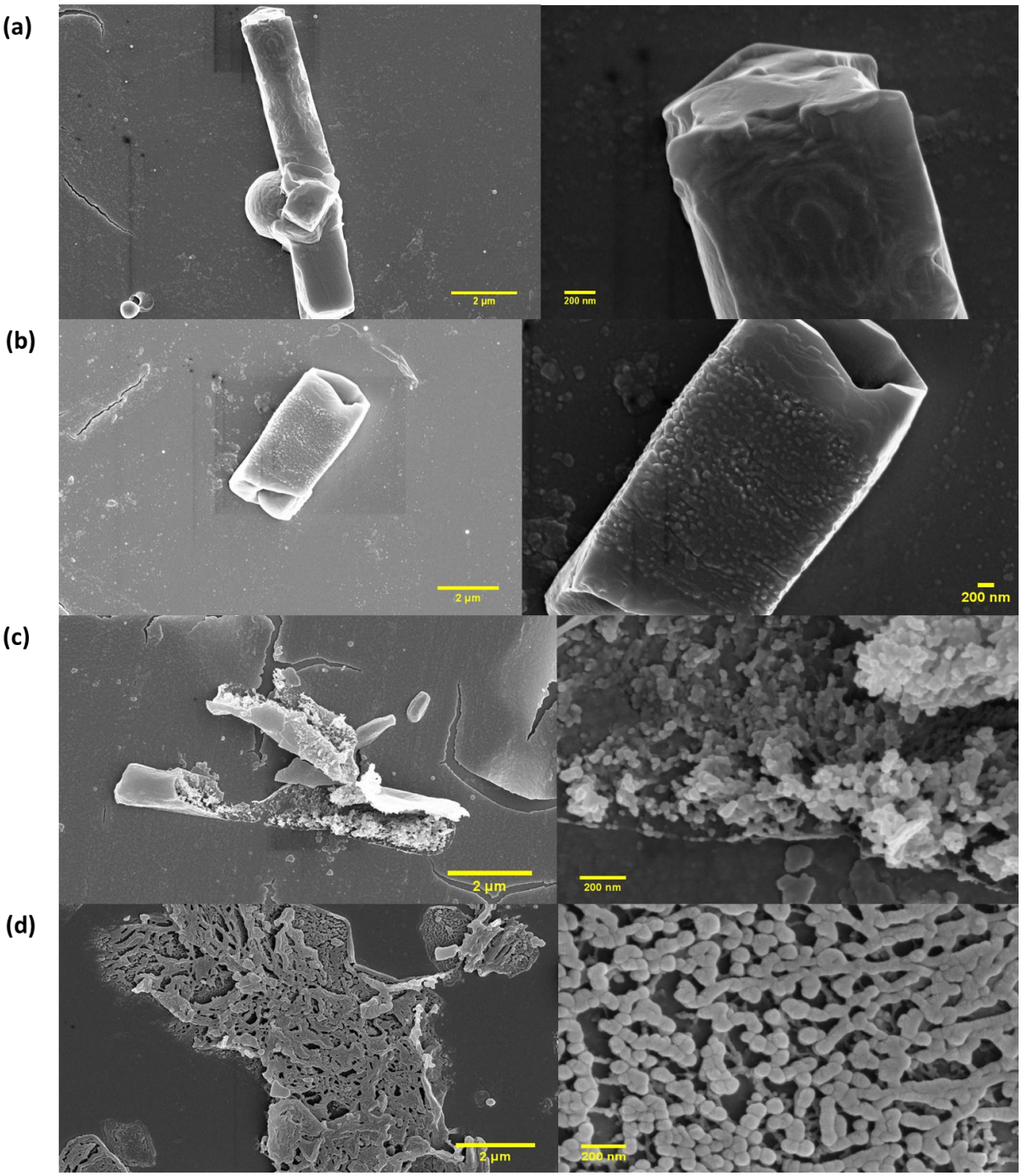

Figure 4.12: SEM images of non-irradiated and irradiated coatings. (a) As deposited, (b) at $1x10^{15}$ protons/cm^2 , (c) at $3x10^{15}$ protons/cm^2 , (d) at $5x10^{15}$ protons/cm^2.

This is the first stage of the melting. Figure 4.12 (c) shows stage two, which is a rather puzzling phenomenon at 3x10^{15} protons/cm^2. The rod ”skins” break open, exposing a very large amount of clustered nanospheres (about 60 nm in diameter). This observation suggests that the rods were in fact sealed enclosures containing nanospheres, analogous to sugar sachets[12]. It is a rather daunting task to suggest how such rods may have formed. The third stage is the melting of the exposed nanospheres into the floor of the coating, as shown in Figure 4.12 (d). These nanospheres also appear to merge as they melt.

As with 900 keV proton radiation, these observations also show strong evidence of lateral diffusion of the energy lost to the coating by the incident protons (Tadadjeu Sokeng *et al*., 2015a). It is, however, difficult to predict what would happen at higher proton fluences. Intuitively one may suggest that the nanospheres would completely melt into the coating, but it is not impossible that unexpected phenomena occur, similar to the rod growth described in section 4.3.2.

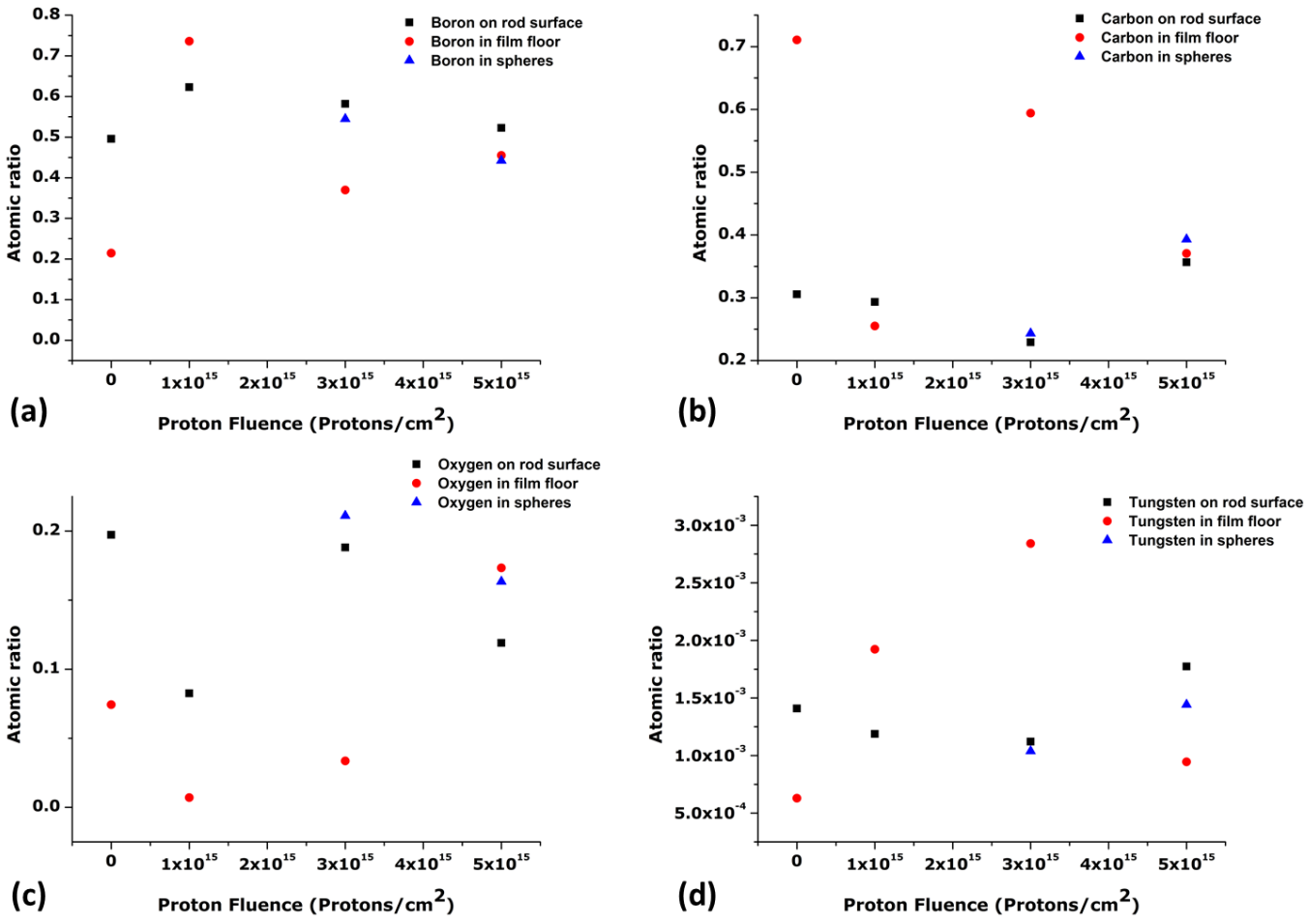

Figure 4.13: Atomic percentage distribution per element as a function of proton fluence. (a) B atomic percentage distribution, (b) C atomic percentage distribution, (c) O atomic percentage distribution, (d) W atomic percentage distribution.

[12] Sugar sachets are sometimes made of a tube-shaped paper enclosures filled with sugar and cealed at both extremeties.

Figure 4.13 (a-d) shows the atomic percentages of B, C, O and W in the coatings as a function of proton fluence. It is difficult to explain the trends in atomic percentages before the rods break open. This is because the phenomenon in itself is not yet explained. Of particular interest, however, is what happens after the rods break open (at $3x10^{15}$ protons/cm^2). In Figure 4.10 (a), B is seen to steadily reduce in the rod surface and in the nanospheres, while at the same time increasing in the floor as the proton fluence increases. Oxygen follows the same trend as seen in Figure 4.10 (c). This trend is to be expected from melting nanostructures, and was already observed in section 4.3 (Tadadjeu Sokeng *et al*., 2015a). In Figure 4.10 (b), C increases steadily in the rod surface and in the nanospheres as it decreases in the floor at the same time with an increase in proton fluence. W follows the same trend as seen in Figure 4.10 (d). These trends suggest that it is possible that nanostructures start forming at higher fluences, just like they did when the atomic percentage of W increased in the nanorods in section 4.3.2. They also show more evidence that the energy lost by the protons to the coating is dissipated in its surface rather than being transferred across itself.

4.5 Optical transmittance of $WC_{1-x}B_x$ coatings

Figure 4.14 shows the percentage transmittance of the control sample relative to the glass substrate used, at room temperature. While the substrate was about 90% transmitting across the near ultraviolet through the visible to the near infrared spectrum, the coating was about 73% transmitting in the same range. This is promising for solar panel applications in space, as it shows that this coating can be used to mitigate the contribution of low energy protons to solar panel degradation, if its transmittance is deemed acceptable. This application, however, would require extensive testing and optimisation.

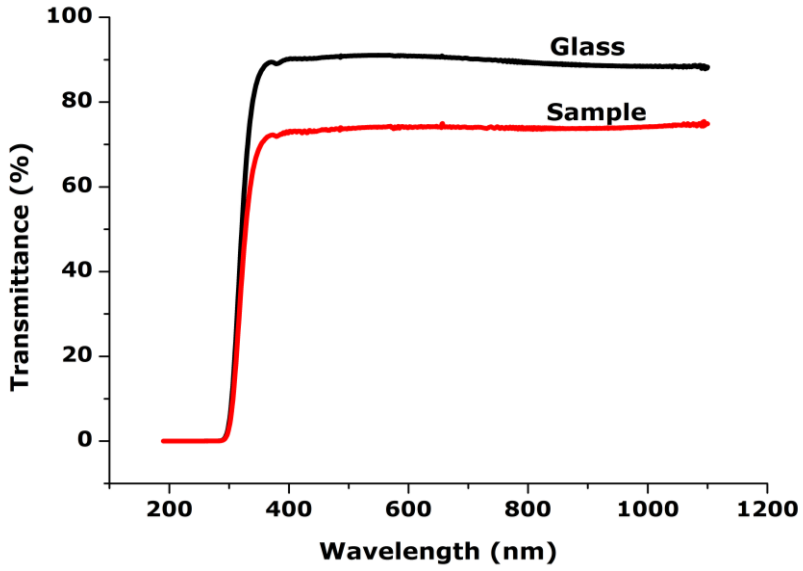

Figure 4.14: Percentage transmittance of the control sample relative to the glass substrate in the UV-Visible range.

4.6 Simulation of the in-orbit shielding capability of $WC_{1-x}B_x$ coatings

In order to quantify the in-orbit shielding capability of $WC_{1-x}B_x$, it is important to start with a sample proton environment for a specified orbit and duration in space. While this work proposes a possible shielding solution to the effects of low energy protons on both solar cells and high density semiconductor devices, this quantification focuses only on solar cells.

It should be noted that this quantification is an approximation. This is because the proposed coating needs further characterisation and application-specific optimisation. Furthermore, the simulation packages used are SRIM and SPENVIS. SRIM does not account for the most interesting aspect of the synthesised coating, which is its preferred lateral transfer of energy from incident protons. The modelling and simulation of this aspect will require extensive further experimentation.

Figure 4.15 is an AP8[13] model of the proton environment in a circular orbit at 5093 km altitude and 60^o inclination (generated using SPENVIS), as used by Messenger *et. al.* in the example that was used to compare the JPL and NRL methods (Messenger *et. al.*, 2001). The solar cell used is a single junction GaAs/Ge cell, and the predicted degradation is shown in Figure 1.6. This figure shows very high total fluences for sub-10 MeV protons over a 1-year space mission.

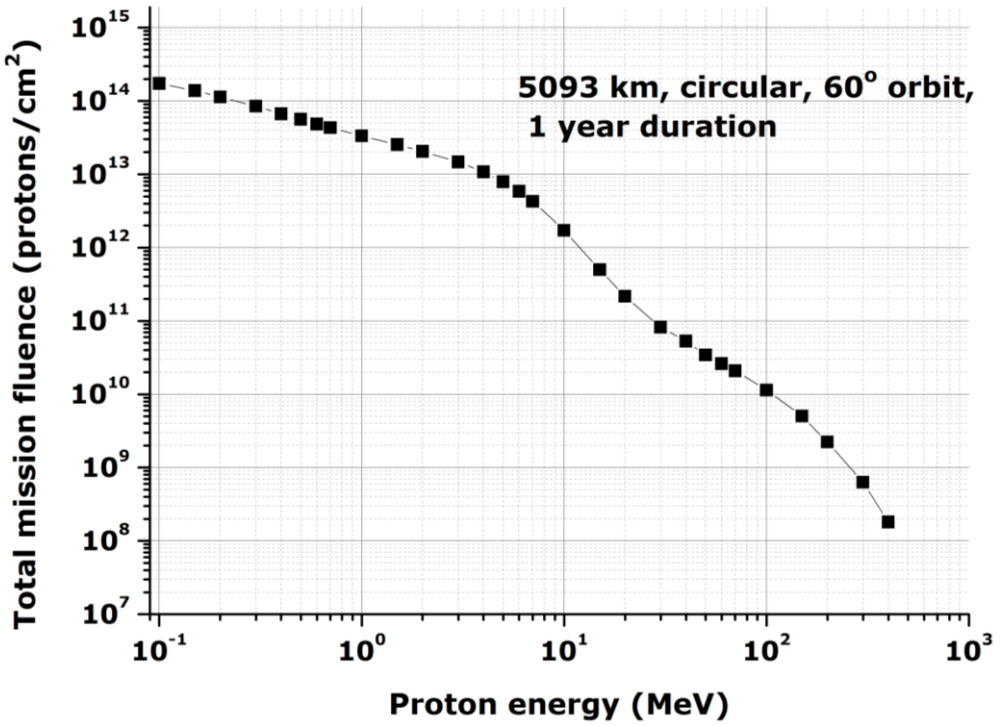

Figure 4.15: SPENVIS generated proton environment for a 1 year mission at 5093 km altitude.

[13] http://ccmc.gsfc.nasa.gov/modelweb/models/trap.php

Figure 4.16 shows the range of protons in SiO_2 and $WC_{0.9}B_{0.1}$ as a function of proton energy as simulated in SRIM. It should be noted that the densities computed by SRIM are not accurate, and this adds further uncertainty to the simulations. SRIM only takes Coulombic interactions into account, and based on that, it is evident from Figure 4.16 that $WC_{0.9}B_{0.1}$ is a better shield against protons than SiO_2 coverglass. To stop a 1 MeV proton, for instance, requires about 14 µm of SiO_2 but only about 8 µm of $WC_{0.9}B_{0.1}$. One can argue that there is an added protection due to the lateral diffusion of energy (and dispersion of matter) of $WC_{0.9}B_{0.1}$ which is not accounted for, since it is not included in SRIM calculations. This added protection should further reduce the range[14] of protons in $WC_{0.9}B_{0.1}$. This simulation was done for proton energies between 0.01 MeV to 10 MeV (sub-10 MeV) as this is the interval of interest in this work, and, in fact, the relevant interval for the current discussion.

Figure 4.17 shows the proton range ratio between $WC_{0.9}B_{0.1}$ and SiO_2. This is plot as a function of proton energy because the range is energy-dependent. It quantifies the equivalent thickness of $WC_{0.9}B_{0.1}$ required to stop protons of a certain energy based on known thicknesses of SiO_2. To stop 2 MeV protons, for instance, would require a thickness of $WC_{0.9}B_{0.1}$ equivalent to half the required SiO_2 thickness.

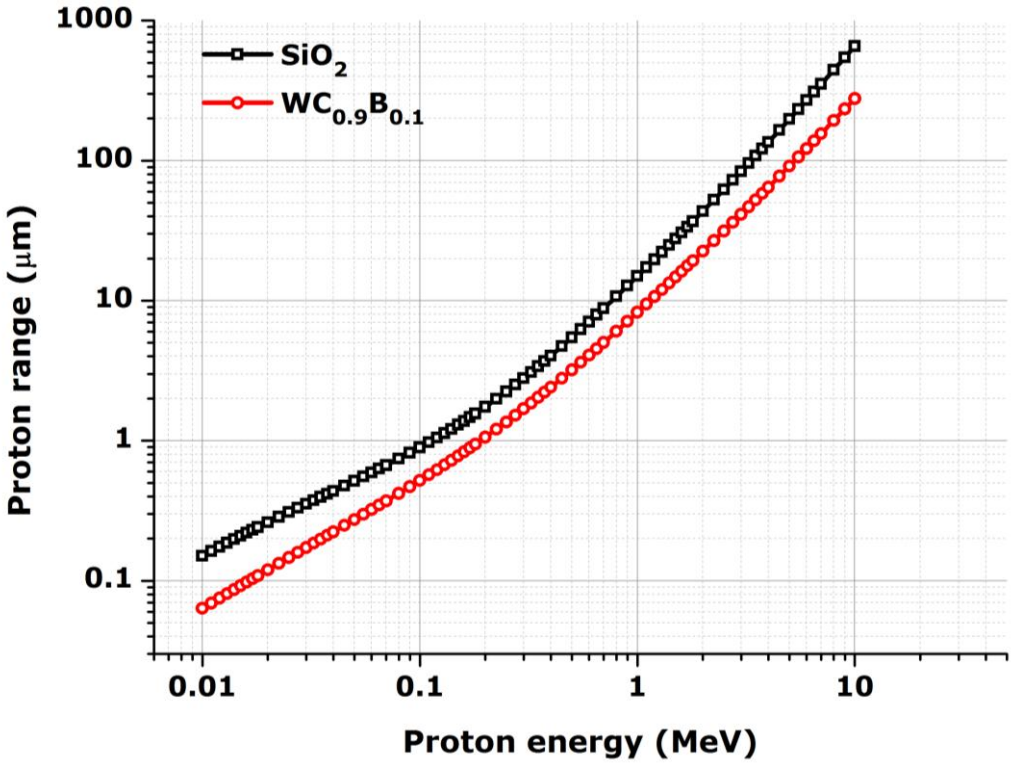

Figure 4.16: SRIM generated proton range in SiO_2 and $WC_{0.9}B_{0.1}$ as function of proton energy

[14] Proton range: The distance required for a proton to lose all its energy in a material and stop.

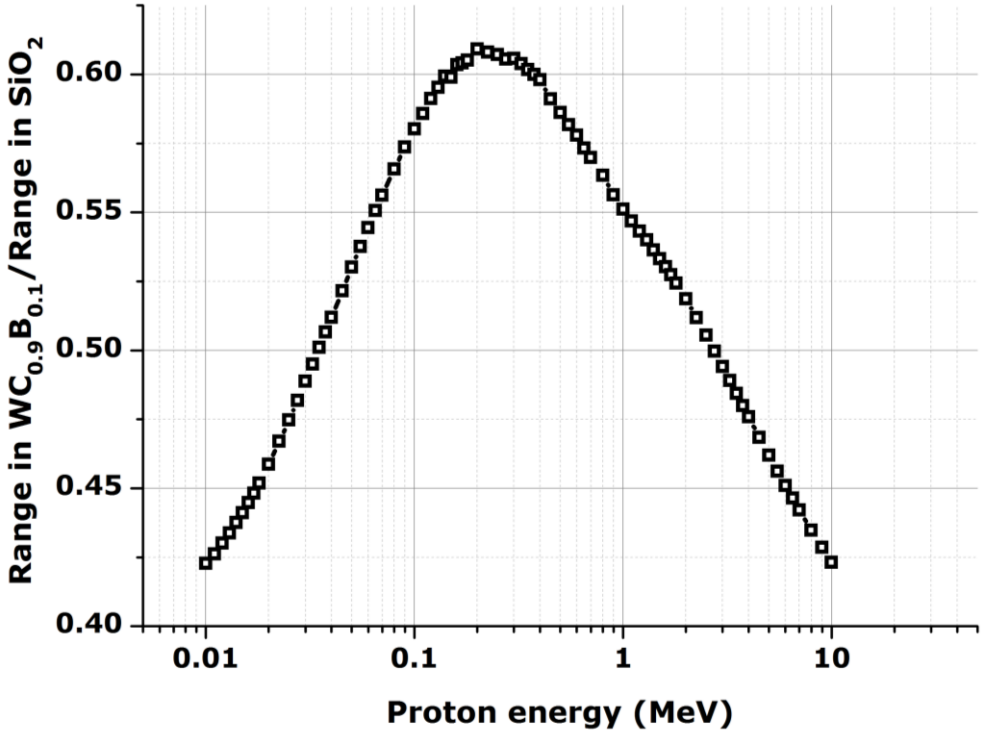

Figure 4.17: $WC_{0.9}B_{0.1}$ / SiO_2 range ratio as a function of proton energy

A typical coverglass thickness is 100 µm. One can read from Figure 4.16 that it would stop protons of about 3.5 MeV, and that it would take only about 52 µm of $WC_{0.9}B_{0.1}$ to achieve the same level of shielding.

The coatings investigated in this work were about 0.4 µm to 0.5 µm thick and were irradiated with 0.9 MeV and 1 MeV protons. From SRIM simulations, transmitted particles had lost about 0.1 MeV of their energy. This is consistent with the readings from Figure 4.16 as it shows that to stop a proton of energy 0.1 MeV requires approximately 0.5 µm of $WC_{0.9}B_{0.1}$, but nearly twice as much of SiO_2.

The significance of this equivalent thickness is that the reduction in degradation that a given thickness of $WC_{0.9}B_{0.1}$ is likely to provide, can be quantified. Figure 1.6 shows the effect of coverglass thickness on End of Life (EOL) normalised maximum power. One can select the equivalent thickness of $WC_{0.9}B_{0.1}$ that would yield the same result and design a required coating thickness. As an example, considering a GaAS/Ge single junction solar cell with a coverglass thickness of 150 µm, one can read from Figure 1.6 that it would correspond to a EOL normalised maximum power of about 0.43. If we assume that, for the purposes of the mission, it were important that the EOL normalised maximum power be at least 0.5 (for instance), then this would require about 200 µm of coverglass (an additional 50 µm). Assume also that this solar cell is commercially available off the shelf, such that it is not possible to

have a special thickness of coverglass made (which is generally the case). One can easily read from Figure 4.17 that the corresponding 10 MeV equivalent thickness of $WC_{0.9}B_{0.1}$ is 0.42 times the extra 50 µm. It then suffices to coat the solar cell with about 21 µm of $WC_{0.9}B_{0.1}$ to achieve the desired shielding.

The equivalent thickness can be further visualised by reading equivalent $WC_{0.9}B_{0.1}$ thicknesses for various proton energies and plotting them on the same graph as in Figure 1.6. Figure 4.18 shows the predicted degradation in normalised power as a function of SiO_2 and $WC_{0.9}B_{0.1}$ thicknesses for the solar cell measured by Messenger *et al.* (Messenger *et. al.*, 2001). One can use it to estimate the thicknesses of $WC_{0.9}B_{0.1}$ (from Figure 4.17) that would achieve the same level of shielding as SiO_2 (from Figure 1.6) for various proton energies. This estimate, however, does not include degradation due to electrons, which is included in the JPL and NRL methods for predicting the degradation of the nomralised maximum power as a function of SiO_2 thickness alone.

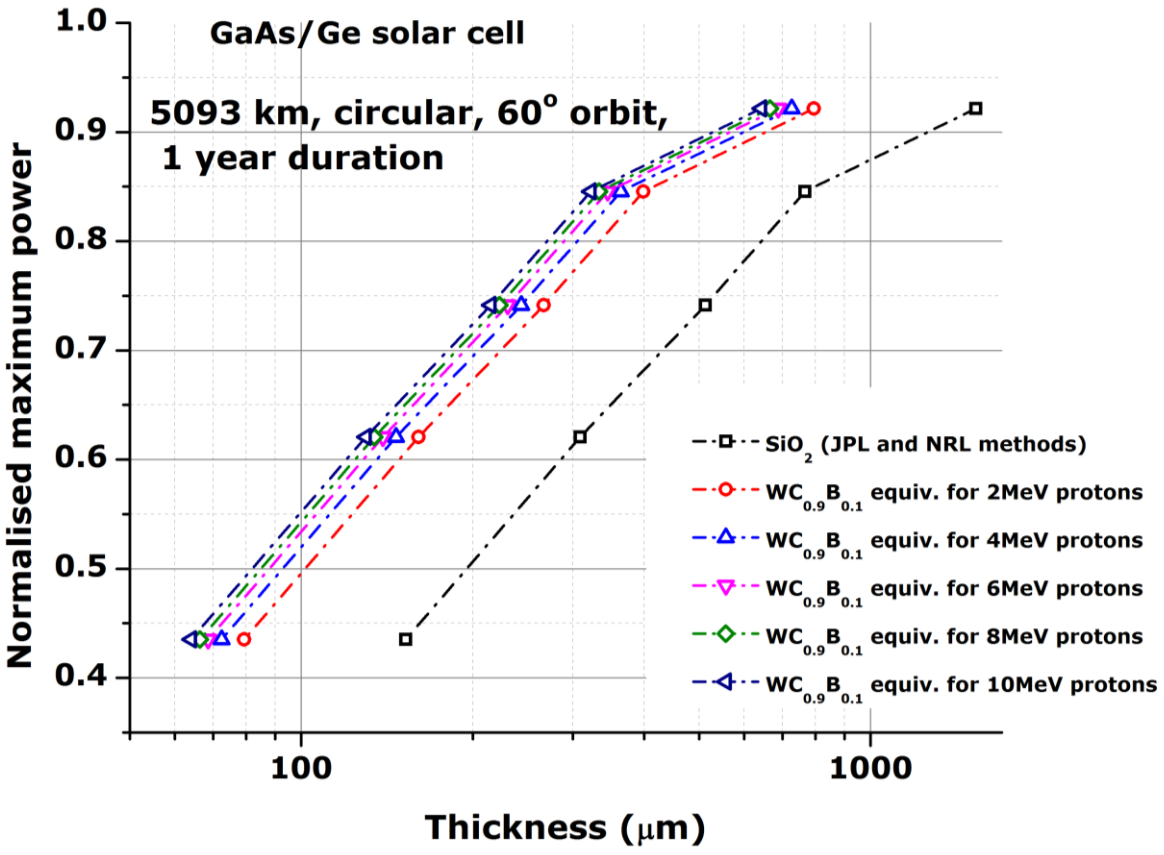

Figure 4.18: Degradation prediction for a GaAs/Ge solar cell as a function of protective SiO_2 and $WC_{0.9}B_{0.1}$ thicknesses.

It is worth mentioning, however, that a $WC_{0.9}B_{0.1}$ coating of thickness about 0.5 µm has a transmittance of only about 73% in the UV-Visible spectrum, as shown in Figure 4.14. This means the coating needs to be optimised further for this application.

4.7 Conclusion

This chapter described the pulsed laser ablation of W_2B_5/B_4C to yield $WC_{1-x}B_x$ coatings. It covered the characterisation and the effects of 900 keV and 1 MeV protons on the latter (synthesised at different laser fluences). The most important aspect of this chapter is the demonstration of the ability of this coating to laterally deflect energy transferred to it by incident protons, and to laterally diffuse matter as a result. The coating deposited at a high laser fluence does this through nanorod melting and regrowth. The coating deposited at a low laser fluence does this through a three-stage nanorod melting. This makes the coating particularly suitable for space application in protection against low energy protons. Of interest are the mitigation of solar panel degradation, and the mitigation of SEUs due to low energy protons in high density semiconductor devices, although the simulation results presented only quantified the shielding capabilities of $WC_{0.9}B_{0.1}$ for solar cell applications.

Chapter 5 General conclusions and recommendations

This work describes a pioneering investigation into the shielding capabilities of a coating obtained from the pulsed laser ablation of W_2B_5/B_4C ceramic composite to low energy protons. Chapters 2 and 3 offer a theoretical overview of the space radiation environment and pulsed laser deposition as a thin film synthesis technique. This background aids in the understanding of the synthesis and characterisation of $WC_{1-x}B_x$ by pulsed laser ablation of W_2B_5/B_4C, its irradiation with 900 keV and 1MeV protons, and the analysis of the effects of irradiation on the coating as described in Chapter 4. This forms the core of the work presented, including:

- The synthesis of a $WC_{1-x}B_x$ solid solution containing both crystalline and amorphous forms by PLD at room temperature (Tadadjeu Sokeng *et al.*, 2015b);
- The demonstration of lateral diffusion of energy and matter exhibited by the deposited coating (Tadadjeu Sokeng *et al*., 2015a);
- The report of nanorod melting and subsequent growth induced by 900 keV protons (Tadadjeu Sokeng *et al*., 2015a);
- The report of a "reversed Stranski-Krastanov film growth mode" occurring naturally and at room temperature;
- The report of a three-stage rod melting mechanism induced by 1 MeV protons;
- The report of a rod structure made up of a material enclosure containing nanospheres;
- The proposition of the applicability of the coating to the mitigation of SEUs and solar cell degradation caused by low energy protons in low Earth orbit;
- The key finding of the quantification of the shielding capability of the coating as compared to SiO_2 (it takes up to 50% less $WC_{1-x}B_x$ thickness to achieve the same level of shielding as SiO_2).

These contributions, to the best of the author's knowledge, are all original additions to literature, and therefore to the general body of knowledge. In fact, this document contributes to the fields of Electrical Engineering, Structural Engineering, Satellite Systems Engineering, Radiation Physics, Experimental Physics, and Material Science.

5.1 Responses to research questions

- How can coatings be synthesised from a B_4C/W_2B_5 pellet?
    - Pulsed Laser Deposition can be used to synthesize coatings from such a pellet. The stoichiometry, however, is not transferred, and the resulting coating is a solid solution of the form $WC_{1-x}B_x$ which contains both crystalline and amorphous forms.

- How can such coatings offer any level of protection against various types of radiation, specifically low energy protons?
    - This coating renders a low energy proton ‘harmless’ rather than stopping it. It does so by laterally transferring the proton energy across the surface of the coating. A consequence of this is the resulting lateral displacement of matter as demonstrated in this work (Tadadjeu Sokeng *et al*., 2015a). It is worth noting that this is not only due to Linear Energy Transfer, as can be expected from any material, but also due to the melting of surface nanostructures.
    - This coating contains B, which has a high Neutron Mass Absorption, as well as W which has a high atomic mass. This means that it can be used to stop neutrons as well as certain levels of X-rays.
    - Simulations show that the coating can provide the same level of shielding that coverglass provides to solar cells with only about half the thickness of coverglass.
- What are the physical mechanisms providing protection against radiation of this coating?
    - The first mechanism identified in this work is the melting of surface nanorods and their subsequent regrowth as described in section 4.3.
    - The second mechanism is the three-stage nanorod melting as described in section 4.4.
- How can these coatings be effectively used for space applications?
    - These coatings are deposited by PLD at room temperature. Commercial components susceptible to SEUs caused by low energy protons can therefore be coated immediately after being purchased. Because this coating is 73% transmitting (for a 0.5 μm thick coating) in the UV, Visible and near IR ranges, it can be considered as protection against solar panel degradation caused by low energy protons in low Earth orbit. Solar panels of small enough dimensions can also be coated as-purchased. Furthermore, the B and W content of these coatings make them promising for protection against neutrons and X-rays due to their high neutron and X-ray absorption cross-sections (Bacon, 1965).
    - These applications, however, require extensive simulation, testing and optimization prior to their implementation. This is because this coating was synthesized for the first time in this work. There is therefore no literature or previous tests or simulations to refer to, or rely on.

- What improvement in longevity do these coatings provide for critical components of a spacecraft, such as solar panels?
    - As described in section 4.6, simulations show that coating a commercial solar panel with this material can offer extra protection against low energy protons and, hence increase the longevity of the solar panel. The longevity that this coating can provide is equivalent to the longevity that commercial coverglass provides, except that this coating provides the same level of protection with only half the thickness (or even less).

5.2 Future work

Chapter 4 shows the radiation shielding capability of $WC_{1-x}B_x$ from experimental studies of proton irradiation at a material level. These studies indicate that using this material to coat high density semiconductor devices could reduce the way they are affected by low energy protons in space. Furthermore, simulations in Section 4.6 show a promising quantification of this shielding for solar cell applications in space.

There is, however, more work to do in order to measure and establish the shielding capabilities of the coating for specific applications. It is invisaged to measure the shielding capabilities of the coating on high density semiconductor devices and on solar panels, both for space applications. These measurements will take about 18 months to complete, and will typically involve one or two Master's theses. The duration of the measurements is estimated based on the bookings of the available radiation beams, the procurement processes, and the design considerations based on the vacuum chambers for live measurements.

5.2.1 Towards high density semiconductor device applications

First, memory cells will need to be designed and manufactured for the purposes of this test. This can be done in collaboration with the University of Pretoria. It will be abosutely necessary in order to quantify the amount of protection this coating provides. Because this coating has never been used for these purposes (and in fact has never been used before), very little is known about it and its properties. In fact, all that is known about it so far is presented in this work. It is advisable to use memory cells that are well understood. These memory cells will be irradiated with and without the coating and the level of protection will then be quantified. SRAM memory cells with feature size ranging between 45 nm and 90 nm will be used because, as seen in Chapter 1, they are the most affected by low energy protons. It will be necessary to delid these components for proton irradiation tests to ensure that their protective packaging does not stop protons before they get to the Silicon dye housing the memory cells. Components will be delided and coated with different thicknesses. Note that these can be coated by PLD because they are about 1.5 cm x 1.5 cm (typically,

PLD can uniformly coat up to about 2 cm x 2 cm, except for few set-ups capable of coating up to 10cm x 10 cm). Live tests will be conducted on the uncoated components according to the guidelines proposed by Schwank *et al.* (Schwank *et al.*, 2013) and those in the JEDEC[15] standards for proton energies ranging from 0.1 MeV to 5 MeV. The coated components will then be tested under the same conditions. The results will be compared to determine the shielding capabilities of different thicknesses of the coating.

5.2.2 Towards solar panel applications

It will be necessary to have a solar panel made specifically for the purposes of the experiments so that its size can be effectively coated (commercial off the shelf solar panels are too large to be fully coated in the available PLD set up, which can coat up to 2 cm x 2 cm uniformly). This can also be done in collaboration with the University of Pretoria. Alternatively, arrangements will have to be made to have access to one of the few PLD set-ups capable of coating larger surface areas.

Only 3 MeV Protons (Flux between $1x10^{10}$ and $1x10^{13}$ protons/cm^2), 1 MeV and 5 MeV electrons (Flux between $1x10^{13}$ and $1x10^{16}$ electrons/cm^2) are necessary to test solar panels using the NRL method mentioned in Chapter 1 (Summers *et. al.*, 1994; Summers *et. al.*, 1995; Summers *et. al.*, 1997; Messenger *et. al.*, 1997; Messenger *et. al.*, 1999; Morton *et. al.*, 1999). Pannels will be tested, some of which will be coated with different thicknesses. The uncoated panels will be used for a typical NRL test. The same test will be performed for each set of coated panels and the result will be compared to evaluate the shielding capability of each thinckess.

As seen in Figure 4.14 of Chapter 4, this coating is not 100% transparent in the Visible, Ultraviolet and Near Infrared spectra. In addition, it may become less transparent as its thickness increases. For the purposes of this test, a trade off between thickness and transparency will have to be used to determine a useful thickness threshold. Alternatively, an optimisation of the coating to enhance transparency will be investigated.

5.3 Recommendations

Pulsed laser deposition is regarded as a laboratory deposition technique, mainly because of the size of the samples. This work shows that it is possible to have direct application using PLD as long as the desired application substrate is of the right size. A large variety of metals, oxides, ceramics and composites can be deposited on Integrated Circuits, Printed Circuit Boards, Solar Panels, enclosures, etc. for various applications. There need not be an industrial applicability for it to be useful on an industrial scale. It is recommended that PLD be

[15] https://www.jedec.org/news/pressreleases/jedec-publishes-new-test-standard-measure-effects-proton-radiation-electronic-dev

considered more as an application technique, rather than just a laboratory technique. This will require additions to certain PLD vacuum chamber set ups, such as mechanisms to move substrates during deposition (rotation and translation), and the ability to alter the temperature of the entire chamber as opposed to the temperature of only the substrate.

The coating synthesised in this work is very promising for space applications in the mitigation of radiation effects by low energy protons. It is recommended that this coating be further tested not only by simulations and in laboratory set ups, but also in space within an active mission. Two CubeSat missions have shown interest in testing this coating on board. These are ZACUBE-3 (3U) designed by CPUT/F'SATI in South Africa, and AOBA-VELOX (2U) designed by Kyushu Institute of Technology in Japan.

The coating needs to be further investigated and characterised to experimentally determine its shielding capabilities. Spectroscopic methods are necessary to investigate lateral versus transverse diffusion of temperature across the coating during irradiation. Thorough electrical and optical characterization and optimisation is required. It is recommended to collaborate with a solar cell manufacturer and with a manufacturer of high density semiconductor devices (SRAM memory cells for instance). This will ensure that the devices to be tested are suitable for the intended irradiation chambers and deposition chambers. It will also ensure that the devices to be tested are known well enough to accurately determine how much of the post coating observations can be in fact attributed to the coating.

References

Allen, P. B. 1987. Theory of thermal relaxation of electrons in metals. *Physical Review Letters*, 59: 1469.

Allison, J., Amako, K., Apostolakis, J., Araujo, H., Dubois, P.A., Asai, M., Barrand, G., Capra, R., Chauvie, S., Chytracek, R., Cirrone, G.A.P., Cooperman, G., Cosmo, G., Cuttone, G., Daquino, G.G., Donszelmann, M., Dressel, M., Folger, G., Foppiano, F., Generowicz, J., Grichine, V., Guatelli, S., Gumplinger, P., Heikkinen, A., Hrivnacova, I., Howard, A., Incerti, S., Ivanchenko, V., Johnson, T., Jones, F., Koi, T., Kokoulin, R., Kossov, M., Kurashige, H., Lara, V., Larsson, S., Lei, F., Link, O., Longo, F., Maire, M., Mantero, A., Mascialino, B., McLaren, I., Lorenzo, P.M., Minamimoto, K., Murakami, K., Nieminen, P., Pandola, L., Parlati, S., Peralta, L., Perl, J., Pfeiffer, A., Pia, M.G., Ribon, A., Rodrigues, P., Russo, G., Sadilov, S., Santin, G., Sasaki, T., Smith, D., Starkov, N., Tanaka, S., Tcherniaev, E., Tome, B., Trindade, A., Truscott, P., Urban, L., Verderi, M., Walkden, A., Wellisch, J.P., Williams, D.C., Wright, D., Yoshida, H. 2006. Geant4 developments and applications. *IEEE Transaction on Nuclear Science*, 53(1): 270-278.

Amoruso, S., Sambri, A. & Wang, X. 2006. Propagation dynamics of a LaMnO laser ablation plume in an oxygen atmosphere. *Journal of Applied Physics*, 100(1): 013302.

Amoruso, S., Toftmann, B. & Schou, J. 2004. Thermalization of a UV laser ablation plume in a background gas: From a directed to a diffusionlike flow. *Physical Review E*, 69: 056403. May.

Anisimov, S. I., Kapeliovich, B. L. & Perel'man, T. L. 1974. Electron emission from metal surface exposed to ultrashort laser pulses. *Soviet Physics- Journal of Experimental and Theoretical Physics*, 39: 375-377.

Anisimov, S. I & Luk'yanchuk, B. S. 2002. Selected problems of laser ablation theory. *Physics-Upsekhi*, 45(3): 293-324.

Anisimov, S. I., Luk'yanchuk, B. S & Luches, A. 1996. An analytical model for three-dimensional laser plume expansion into vacuum in hydrodynamic regime. *Applies Surface Science*, 96-98: 24-32. April.

Anspaugh, B.E. & Downing, R.G. 1984. *Radiation effects in Silicon and Gallium Arsenide Solar Cells Using Isotropic and Normal Incident Radiation*, 61-84. JPL Publication.

Anspaugh, B.E. 1989. *The Solar Cell Radiation Handbook-Addendum 1: 1982-1988*, 69-92. JPL Publication.

Anspaugh, B.E. 1996. *GaAs Solar Cell Radiation Handbook,* 96-99. JPL Publication.

Arnold, N., Gruber, J & Heitz, J. 1999. Spherical expansion of the vapor plume into ambient gas: An analytical model. *Applied Physics A Materials Science & Processing*, 69(7): 87-93.

Aukerman, L. W. 1962. Proton and electron damage to solar cells.
REIC Report No. 23, Battelle Memorial Institute.

Bacon, G.E. 1956. Neutron diffraction. 2nd ed. In Jackson, W., Fröhlich, H., Mott, N.F. & Bullard, E.C. (eds). *Monographs on the Physics and Chemistry of Materials*. London: Oxford University Press: 60-63..

Badhwar, G. D. 1997. The radiation environment in low earth orbit. *Radiation Research, Supplement: Space Radiation Damage and Biodosimetr*, 148(5): S3-S10, November.

Barak, J. 2006. Simple calculations of proton SEU cross-sections from heavy ion cross-sections. *IEEE Transactions on Nuclear Science*, 53(6): 3336-3342, December.

Bardeen, J. & Brattain, W. H. 1948. The transistor – A semiconductor triode. *Physical Review*, 74: 230-231.

Barnard, A. & Nwosa, C. 2011. COTS based on-board-computer on South Africa's Sumbandilasat: A radiation and in-orbit performance analysis. *IEEE Radiation Effects Data Workshop*: 1-4, July 25-29.

Barnard, A. & Steyn, W.H. 2007. Low cost TID testing of COTS components. 9th *European Conference on Radiation and its Effects on Components*: 1-4, September 10-14.

Bäuerle, D. 2000. *Laser Processing and Chemistry*. 3rd ed. Berlin: Springer.

Bekhti, M. 2013. Radiation analysis of InGaP/GaAs/Ge and GaAs/Ge solar cell: A comparative study. *Internatioal Journal of Renewable Energy Research*, 3(4). Available

online. http://www.ijrer.org/index.php/ijrer/article/download/893/pdf. [10 December 2014].

Bilinski, J. R., Brooks, E. H., Cocca, U., Maier, R. J., & Siegworth, D. W. 1962. Proton-neutron damage correlation in semiconductors. *Final Report Contract No. NAS 1-1595, General Electric Company*, Syracuse, New York.

Billington, D. S. & Crawford, J. H. Jr. 1961. *Radiation Damage in Solids*. New Jersey: Princeton University Press.

Binder, D., Smith, E. & Holman, A. Satellite anomalies from galactic cosmic ray. *IEEE Transactions on Nuclear Science*, NS-30: 2675-1975.

Boardman A.D., Cresswell, B & Anderson, J. 1996. An analytical model for the laser ablation of materials. *Applied Surface Science*, 96-95: 55-60. April.

Böhlen, T.T., Cerutti, F., Chin, M.P.W., Fassò, A., Ferrari, A., Ortega, P.G., Mairani, A., Sala, P.R., Smirnov, G. & Vlachoudis, V. The FLUKA code: Development and challenges for high energy and medical applications. *Nuclear Data Sheets*, 120: 211-214.

Cai, K.-f. & Nan, C.-W. 2000. The influence of W_2B_5 addition on microstructure and thermoelectric properties of B_4C ceramic. *Ceramics International*, 26(5):523-527, June.

California Polytechnic State University. *s.a*. *CubeSat design specification, revision 12*. http://cubesat.atl.calpoly.edu/images/developers/cds_rev12.pdf. [10 October 2012].

Cannon, E. H., Cabanas-Holmen, M., Wert, J., Amort, T., Brees, R., Koehn, J., Meaker, B. & Normand, E. 2010. Heavy ion, high-energy, and low-energy proton SEE sensitivity of 90 nm RHBD SRAMS. *IEEE Transactions on Nuclear Science*, 57(6): 3493-3499, December.

Chadderton, L. T. 1965. *Radiation Damage in Crystals*. New York: John Wiley.

Chapin, D. M., Fuller, C. S. & Pearson, G. L. 1954. A new silicon p-n junction photocell for converting solar radiaition into electrical power. *Journal of Applied Physics*, 25: 676.

Chen, N. C., Shih, C. F., Chang, C. A., Chiu, A. P., Teng, S. D. & Liu, K. S. 2004. High quality GaN films grown on Si(111) by reversed Stranski-Krastanov growth mode. *Physica Status Solidi (b)*, 241(12): 2698-2702, October.

Chichkov, B. N., Momma, C., Nolte, S., von Alvensleben, F & Tünnermann, A. 1996.

Femtosecond, picosecond and nanosecond laser ablation of solids. *Applied Physics A*, 63(2): 109-115. August.

Clyde Space. 2012. http://www.clyde-space.com/cubesat/som_useful_info_about_cubesats. [10 October 2012].

Corkum, P. B., Brunel, F., Sherman, N. K & Srinivasan-Rao, T. 1988. Thermal response of metals to untrashot-pulse laser excitation. *Physical Review Letters*, 61(25): 2886.

Cucinotta, F. A., Hongu, W., Shavers, M. R. & George, K. 2003. Radiation dosimetry and biophysical models of space radiation effects. *Gravitational and Space Biology Bulletin*, 16(2): 11-18, June.

Dang, H. J., Zhou, M. F & Qin, Q. Z. 1999. Optical emission spectrometric characterization of plumes generated from laser-ablated $Pr_{0.67}Sr_{0.33}MnO_3$. *Applied Surface Science*, 140(1-2): 118-125. February.

Dijkkamp, D., Vankatesan, T., Wu, X. D., Shaheen, S. A., Jisrawi, N., Minlee, Y. H., McLean, W. L & Croft, M. 1987. Preparation of Y-Ba-Cu oxide superconductor thin films using pulsed laser evaporation from high T_c bulk material. *Applied Physics Letters*, 52(8): 619-622. August.

Dreyfus, R. W. 1993. Interpreting laser ablation using cross-sections. *Surface Science*, 283(1-3): 177-181. March.

Dyer, P. E., Issa, A & Key, P. H. 1990. Dynamics of excimer laser ablation of superconductors in an oxygen environment. *Applied Physics Letters*, 57(2): 186-189. July.

Einstein, A. 1917. Zur quantentheorie der strahlung. *Physikalische Zeitschrift*, 18:121-128.

Evans, R. D. 1955. *The Atomic Nucleus*. New York: McGraw-Hill.

Ferrari, A., Sala, P.R., Fassò, A. & Ranft, J. 2005. FLUKA: A multi-particle transport code. *CERN-2005-10, INFN/TC_05/11, SLAC-R-773*, October.

Frank, F. C. & Van der Merwe, J. H. 1949. One-dimensional dislocations. 1. Static theory. *Proceedings of the Royal Society of London. Series A, Mathematical and Physical Sciences*, 198(1053): 205-216. August.

Gaillard, R. 2011. Single event effects: Mechanisms and classification. In Nicolaidis, M. (ed). *Soft Errors in Modern Electronic Systems*. New York Heidelberg: Springer: 27-54.

Geant4 Collaboration, 2003. GEANT4-A simulation toolkit. *Nuclear Instruments and Methods in Physics Research A*, 506: 250-303.

Geohegan, D. B. 1994. Diagnostics and characteristics of laser-produced plasmas. In Chrisey, D. B. & Hubler, G. K. (eds). *Pulsed Laser Deposition of Thin Films*. New York: Wiley.

Gibert, T., Dubrueil, B., Barthe, M. F & Dubrun, J. L. 1993. Investigation of laser sputtering of iron at low fluence using resonance ionisation mass spectrometry. *Journal of Applied Physics*, 74(5): 3506-3514. September.

Glasstone, S. & Sesonske, A. 1963. *Nuclear Reactor Engineering*. New Jersey: D. Van Nostrand Company Inc.

Glenn, F.K. 2010. *Radiation Detection and Measurement*. 4th ed. *s.l.* John Wiley.

Gonzalo, J., Afonso, C. N. & Madariaga, I. 1997. Expansion dynamics of the plasma produced by laser ablation of $BaTiO_3$ in a gas environment. *Journal of Applied Physics*, 81: 951-955.

Green, M. L. & Hamman, D. J. 1971. *Radiation Effects Design Handbook Section 5. The Radiation in Space and Their Interactions With Matter*. Columbus: NASA.
Guenzer, C. S., Wolicki, E. A. & Allas, R. G. 1979. Single event upset of dynamic RAM by neutrons and protons. *IEEE Transactions on Nuclear Science*, 26(6): 5048-5052.

Haduverdi, M. & Baylakoglu, I. 2011. Space environment and evaluation for RASAT. *5th International Conference on Recent Advances in Space Technologies*:926-931, June 9-11.

Harilal, S. S., Bindhu, C. V., Tillack, M. S., Najmabadi, F & Gaeris, A. C. 2003. Internal structure and expansion dynamics of laser ablation plumes into ambient gases. *Journal of Applied Physics*, 93(5): 2380-2389. March.

Hubert, G., Duzellier, S., Bezerra, F. & Ecoffet, R. 2009. MUSCA SEP^3 contribution to investigate the direct ionisatioin proton upset in 65 nm technology for space atmospheric and

ground applications. *European Conference on Radiation and Its Effects on Components and Systems*: 179-186, September.

Huijben, M. 2006. Interface engineering for oxide electronics : Tuning electronic properties by automatically controlled growth. PhD Thesis, University of Twente.

Inam, A., Hedge, M. S., Wu, X. D., Venkatesan, T., England, P., Miceli, P. F., Chase, E. W., Chang, C. C., Tarascon, J. M & Wachtman, J. B. 1988. As- deposited high T_c and J_c superconducting thin films made at lowtemperatures. *Applied Physics Letters*, 53(10): 908-911. September.

Itina, T. E., Katassonov, A. A., Marine, W. & Auric, M. 1998. Numerical study of the role of a background gas and system geometry in pulsed laser deposition. *Journal of Applied Physics*, 83(11): 6050-6055. June.

Kaganov, M. I., Lifshitz, I. M & Tanatarov, L. V. 1957. *Soviet Physics-JETP*, 4: 173-178.

Kilby, J. S. 1964. Miniaturized electronic circuit. US Patent 3,138,743, June.

Kilby, J.S. 1964. Integrated semiconductor circuit device. US Patent 3,138,747, June.

Koshiishi, H. & Matsumoto, H. 2012. Space radiation environment in low earth orbit during solar-activity minimum period from 2006 through 2011. *Journal of Atmospheric and Solar-Terrestrial Physics*, Accepted manuscript, available online [17 September 2012].

Kumuduni, W. K. A., Nakayama, Y., Nakata, Y., Okada T & Maeda, M. 1993. Transport of YO molecules produced by ArF laser ablation of $YBa_2Cu_3O_{7-\delta}$in ambient oxygen gas. *Journal of Applied Physics*, 74(12): 7510-7517. December.

Landau, L. D. & Lifshitz, E. M. 1987, *Fluid Mechanic*. 2nd ed. Oxford: Pergamon Press.

Lawrence, R.K., Ross, J.F., Haddad, N.F., Reed, R.A. & Albrecht, D.R. 2009. Soft error sensitivity in 90 nm bulk CMOS SRAMs. *IEEE Radiation Effects Data Workshop*: 123-126.

Lilienfeld, E. J. 1933. Device for controlling electric current. US Patent 1,900,018, July.

Maiman, T.H. 1960. Stimulated optical radiation in Ruby. *Nature*, 187: 493-494, August.

Maini, A.K. & Agrawal, V. 2011. *Satellite Technology: Principles and Applications*. Chichester: John Wiley.

Maurer, R.H., Fraeman, M.E., Martin, M.N. & Roth, D.R. 2008. Harsh environments : Space radiation environment, effects, and mitigation. *John Hopkins APL Technical Digest*, 28(1) : 17-29.

May, T. C. & Woods, M. H. 1979. Alpha-particle-induced soft errors in dynamic memories. *IEEE Transaction on Electron Devices*, 26(1): 2-9.

Mayanbari, M. & Kasesaz, Y. 2011. Design and analyse space radiation shielding for a nanosatellite in low earth orbit (LEO). *5th International Conference on Recent Advances in Space Technologies,* 487-493, June 9-11.

Messenger, S.R., Xapsos, M.A., Burke, E.A., Walters, R.J. & Summers, G.P. 1997. Proton displacement damage and ionising dose for shielded devices in space. *IEEE Transactions on Nuclesr Science*, 44(6): 2169-2173.

Messenger, S.R., Burke, E.A., Summers, G.P., Xapsos, M.A., Walters, R.J., Jackson, E.M. & Weaver, B.D. 1999. Nonionising energy loss (NIEL) for heavy ions. *IEEE Transaction on Nuclear Science,*46(6): 1595-1602.

Messenger, S.R., Summers, G.P., Buerke, E.A., Walters, R.J. & Xapsos, M.A. 2001. Modeling solar cell degradation in space: A comparison of the NRL displacement damage dose and the JPL equivalent fluence approaches. *Progress in Photovoltaics: Research and Applications,* 9:103-121.

Messenger, S.R., Burke, E.A., Walters, R.J., Warner, J.H. & Summers, G.P. 2005. Using SRIM to calculate the relative damage coefficients for solar cells. *Progress in Photovoltaics: Research and Applications*, 13(2): 115-123. March.

Moore, G. E. 1965. Cramming more circuits on chips. *Electronics*, 38(8), April.

Morton, T.L., Chock, R., Long, K., Bailey, S., Messenger, S.R., Walters, R.J. & Summers, G.P 1999. Use of displacement damage dose in an engineering model of GaAs solar cell radiation damage. *11th international Photovoltaic Science and Engineering Conference, Hokkaido, Japan,* 815-816.

Ngom, B.D. 2010. Structural and physical properties of ReNiO3 (Re=Sm, Nd) nanostructured films prepared by Pulsed Laser Deposition. Unpublished PhD thesis, University of the Western Cape.

Nolte, S., Momma, C., Jacobs, H., Tünnermann, A., Chichkov, B. N., Wellegehausen, B & Welling H. 1997. Ablation of metals by ultrashort laser pulses. *Journal lf the Optical Society of America B*, 14(10): 2716-2722.

Okhoshi, M., Yoshitake, T & Tsushima, K. 1994. Dynamics of laser-ablated iron in nitrogen atmosphere. *Applied Physics Letter*, 64(24): 3340-3343. June.

Peterlongo, A., Miotello, A & Kelly, R. 1994. Laser-pulse sputtering of aluminium: vaporization, boiling, superheating, and gas-dynamic effects. *Physical Review E*, 50: 4716. December.

Phipps, C. R., Turner, T. P., Harrison, R. F., York, G. W., Osborne, W. Z., Anderson, G. K., Corlis, X. F., Haynes, L. C., Steele, H. S., Spicochi, K. C & King, T. R. 1988. Impulse coupling to targets in vacuum by KrF, HF, and CO_2 single-pulse lasers. *Journal of Applied Physics*, 64(3): 1083-1096. August.

Pickel, J. & Blandford, J. 1978. Cosmic ray induced errors in MOS memory cell. *IEEE Transactionson Nuclear Science*, NS-30: 1166-1978.

Pippin, G. 2003. Space environments and induced damage mechanisms in materials. *Progress in Organic Coatings*, 47:424-431.

Predteceensky, M. R & Mayorov, A. P. 1993. Expansion of laser plasma in oxygen at laser deposition of HTSC filsm: theoretical model. *Applied Superconductivity*, 1(10-12): 2011-2017. October-December.

Qiu, T.Q. & Tien, C.L. 1993. Heat transfer mechanism during short-pulsed laser heating of metals. *Journal of Heat Transfer*, 115: 835-841.

Radev, D.D., Milhailova, B. & Konstantinov, L. 2002. Raman spectroscopy study of metal-containing boron carbide-based ceramics. *Solid State Sciences,* 4:37-41.

Ready, J. F. 1971. *Effects of High-Power Laser Radiation*. New York: Academy Press.

Reitz, G. 2008. Characteristic of the radiation field in low earth orbit and in deep space. *Zeitschrift für Medizinische Physik*, 18(4):233-243.

Reitz, G., Beaujean, R., Benton, E., Burmeister, S., Dachev, Ts., Deme, S., Luszik-Bhadra & Olko, P. 2005. Space radiation measurements on-board ISS- The DOSMAP experiment. *Radiation Protection Dosimetry*, 116(1-4): 374-379.

Rijnders, G. 2001. The initial growth of complex oxides: study and manipulation. PhD thesis, University of Twente.

Santin, G., Ivanchenko, V., Evans, H., Nieminen, P. & Daly, E. 2005. GRAS: A general-purpose 3-D modular simulation tool for space environment effects analysis. *IEEE Transactions on Nuclear Science*. 52(6): 2294-2299.

Schwank, J. R., Shaneyfelt, M. R. & Dodd, P. E. 2013.Radiation hardness assurance testing for microelectronic devices and integrated circuits: Test guideline for proton and heavy ion single-event effects. *IEEE Transactions On Nuclear Science,* 60(3):2101-2118.

Seitz, F. & Koehler, J. S. 1952. Displacement of atoms during irradiation. In Seitz, F & Turnbull, D. *Solid State Physics*, Vol 2. New York: Academic Press Inc.

Shockley, W. 1951. Circuit element utilising semiconductive material. US Patent 2,569,347.

Shockley, W. 1961. Problems related to p-n junctions in silicon. *Czechoslovak Journal of Physics*, B 11: 81-121.

Singh, R. K & Narayan, J. 1990. Pulsed-laser evaporation technique for deposition of thin films : Physics and theoretical model. *Physical Review B*, 41 : 8843-8858. May.

Singh, R. K., Holland, O. W & Narayan, J. 1990. Theoretical model for deposition of semiconducting thin films using pulsed laser evaporation technique. *Journal of Applied Physics*, 68 : 233-247.

Smith, H. M & Turner, A. F. 1965. Vacuum deposited thin films using a ruby laser. *Applied Optics*, 4(1): 147-148.

Stranski, N. I. & Krastanov, L. 1938. Theory of orientation separation of ionic crystals. *Sitzungsberichte / Akademie der Wissenschaften in Wien, Mathematisch-*

Naturwissenschaftliche Klasse Abteilung IIB, 146: 797–810.

Strauch, K. 1962. Measuremsnts of secondary spectra from high-energy nuclear reactions. *Symposium on Protection Against Radiation Hazards in* Space, 2:409.

Summers, G.P., Walters, R.J., Xapsos, M.A., Burke, E.A., Messenger, S.R., Shapiro, P. & Statler, R.L. 1994. A new approach to damage prediction for solar cells exposed to different radiation. *IEEE Proceedings on the First Worls Conference on Photovoltaic Energy Convention*, 2068-2073. Hawaii.

Summers, G.P., Burke, E.A. & Xapsos, M.A. 1995. Displacement damage analgogs to ionising radiation effects. *Radiation Measurements,* 24(1): 1-8.

Summers, G.P., Messenger, S.R., Burke, E.A., Xapsos, M.A. & Walters, R.J. 1997. Contribution of low energy protons to the degradation of shielded GaAs solar cells in space. *Progress in Photovoltaics: Research and Application,* 5: 407-413.

Summers, G.P., Messenger, S.R., Burke, E.A., Xapsos, M.A. & Walters, R.J. 1997. Low energy proton-induced displacement damage in shielded GaAs solar cells in space. *Applied Physics Letters*, 71(6): 832-834.

Tada, H.Y., Carter, J.R., Anspaugh, B.E. & Downing, R.G. 1982. *The Solar Cell Radiation Handbook*, 3rd Edition, 69-82. JPL Publication.

Tadadjeu Sokeng, I., Ngom, B. D., Cummings, F., Kotsedi, L., Msimanga, M., Maaza, M. & Van Zyl, R. R. 2015a. Proton-induced nanorod melting in a coating obtained from the pulsed laser ablation of W_2B_5/B_4C. *Nuclear Instruments and Methods in Physics Research B*, 344: 70-75, February.

Tadadjeu Sokeng, I., Ngom, B.D., Coetzee-Hugo, L., Msimanga, M., Nuru, Z. Y., Kotsedi, L., Maaza, M., Van Zyl, R. R. 2015b. Coatings synthesized by the pulsed laser ablation of W_2B_5/B_4C ceramic composite. *Thin Solid Films,* Available online [21 September 2015]: http://www.sciencedirect.com/science/article/pii/S0040609015009086

Ulmer, W. & Matsinos, E. 2010. Theoretical methods for the calculation of Brag curves and 3D distributions for proton beams. *European Physical Journal Special Topics*, 190:1-81.

Van Lint, V. A. J. & Wikner, E. G. 1963. Correlation of radiation types with radiation effects.

IEEE Transactions on Nuclear Sciences, 1:80-87, January.

Venkatesan, T., Wu, X. D., Inam, A & Wachtman, J. B. 1988. Observation of two distinct components during pulsed laser deposition of hich T_c superconducting films. *Applied Physics Letters*, 52(14): 1193.

Volmer, M. & Weber, A. 1926. Keimbildung in übersättigten gebilden. *Zeitschrift für Physikalische Chemie*, 119: 277-301.

Wallace, R. & Sondhaus, C. 1962. Techniques used in shielding calculations for high-energy acelerators: applications to space shielding. *Symposium on Protection Against Radiation Hazards in Space*, 2:829.

Wallmark, J. & Marcus, S. 1962. Minimum size and maximum packing density of nonredundant semiconductor devices. *Institute of Radio Engineering Proceedings*, 50: 286-298.

Wang, Z. 2008. Fabrication and applications progress on Boron Carbon for bulletproof ceramics. *China Powder Science and Technology*, 14(3):56-59.

Wang, Z. 2008. Research progress of Boron Carbon for bulletproof ceramic. *Bulletin of Chinese Ceramic Society*, 27(1):132-135, February.

Wanlass, F. 1967. Low stand-by power complementary field effect circuitry. US Patent 3,356,858, December.

Wen, G., li, S.B., Zhang, B.S. & Guo, Z.X. 2000. Processing of in situ toughened B-W-C composites by reaction hot pressing of B_4C and WC. *Scripta Materialia,* 43(9):853-857.

Wood, R. F., Chen, K. R., Leboeuf, J. N., Puretzky, A. A & Geohegan, D. B. 1997. Dynamics of plume propagation and splitting during pulsed-laser ablation. *Physials Review Letters*, 79: 1571-1574.

Wrobel, F. & Saigne, F. 2011. MC-Oracle – A tool for predicting soft error rate. *Computer, Physics, Communications*, 182: 317-321.

Yin, J., Huang, Z., Liu, X., Zhang, Z. & Jiang, D. 2013. Microstructure, mechanical and thermal properties of *in situ* toughened boron carbide-based ceramic composites co-doped

with tungsten carbide and pyrolytic carbon. *Journal of the European Ceramic Society*, 33(10):1647-1654, September.

Zel'dovic, Y. B & Raizer, Y. P. 1966. *Physics of Shock Waves and High-Temperature Hydrodynamic Phenomena*. New York: Academic Press.

Ziegler, J.F., Ziegler, M.D. & Biersack, J.P. 2010. SRIM - The stopping and range of ions in matter. *Nuclear Instruments and Methods in Physics Research B*, 268(11-12): 1818-1823.